EOM-3901

MASTER'S THESIS IN ENERGY, CLIMATE AND ENVIRONMENT

A gas-hydrate related BSR on the W-Svalbard margin: distribution, geological control and formation mechanisms

Kristine Vevik

June, 2011

Faculty of Science and Technology

Department of Geology

University of Tromsø

EOM-3901

MASTER'S THESIS IN ENERGY, CLIMATE AND ENVIRONMENT

A gas-hydrate related BSR on the W-Svalbard margin: distribution, geological control and formation mechanisms

Kristine Vevik

June, 2011

Abstract

A widespread bottom-simulating reflection (BSR) defining the base of the gas hydrate stability zone (BGHSZ) exists on seismic data from the western Svalbard margin, including the Vestnesa Ridge, which is a mounded and elongated sediment drift NW of Svalbard to the north of the Molloy Transform. The BSR stretches from the continental slope to within few km of the mid-oceanic ridge system thereby shoaling due to an increase in heat flow over the juvenile oceanic crust, which cools off in eastward direction. The interpretation of a BSR leads to the subdivision into three regions based on distribution and geological setting, namely the Vestnesa Ridge, the continental slope and the Molloy Transform Fault (MTF), where potential gas hydrate occurrences comprise an area of ~2700 km^2. The BSR occurrence and inferred hydrate accumulation zone is bound by impermeable glacial debris-flow (GDF) deposits on the upper continental slope, the Knipovich Ridge and MTF to the south and the Molloy Ridge to the west. Enhanced reflections beneath the BSR indicate the presence of significant amounts of free gas.

The crest of the Vestnesa Ridge at water depth between 1200-1500 m is pierced with fluid-flow features, but they are absent on the flanks of the ridge, where hydrate-bearing sediments effectively reduce the permeability of the sediments. Thus, fluids are forced to migrate laterally upwards along the GHSZ towards the crest in this topographically controlled system. The vigorous flow of fluids at the crest disrupts the BSR, causing it to shoal locally in vicinity of fluid-flow features. The fluid-flow features are often connected to deep-seated faults indicating a deep hydrocarbon gas supply, which is corroborated by hydrate-stability modeling suggesting a larger fraction of thermogenic hydrocarbons involved in hydrate formation. In addition to that, the combination of high heat flow, tectonic activity, a thick sedimentary cover and a shallow maturation window suggests that the free-gas/gas-hydrate system at the Vestnesa Ridge is more active and dynamic than elsewhere in the study area. Free-gas/gas-hydrate systems on the lower continental slope and at the MTF seem mostly in a steady state with gas predominantly originating from biogenic methanogenesis.

Acknowledgements

Table of Contents

1. Introduction

1.1 Objectives

The primary objectives of the thesis are to identify and map the distribution of a bottom-simulating reflector (BSR) related to the occurrence of gas hydrates on the western Svalbard margin (figure 1-1), which is supposedly stretching from the shelf edge and all the way to the sedimented mid-ocean ridge, thereby covering a highly variable geological setting. The thesis is based on analysis of 2D and 3D seismic data. The BSR provides indirect evidence for the presence of gas hydrates in sub-seafloor sediments, and its location is controlled mainly by pressure, temperature and gas composition. The geological processes that control the occurrence of gas hydrates and the formation mechanisms for the BSR will be assessed. Another aim in addition to that is a better understanding of fluid migration and accumulation mechanism supported by modeling of gas hydrate stability that allows an assessment of the origins of the gas and the state of the free-gas/gas-hydrate system. The relatively young and peculiar geological setting on the western Svalbard margin makes this a compelling area to study gas-hydrate formation, free-gas migration and fluid expulsion in marine sediments, their governing parameters and their relationship with each other.
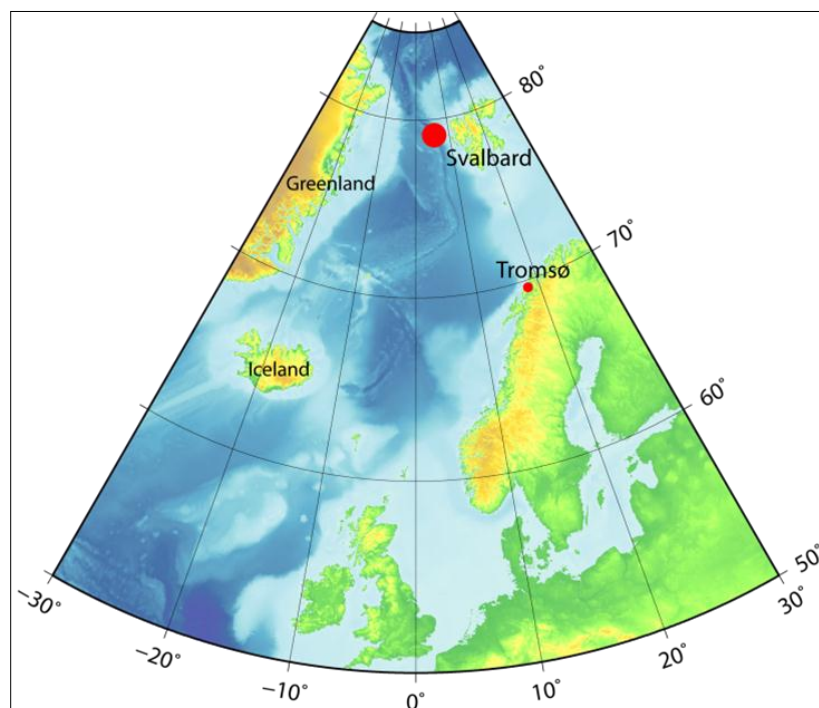
Figure 1-1: Map showing the location of the western Svalbard margin (From Petersen et al. 2008).

1.2 Structure and outline

In order to meet the objectives previously described, the thesis is structured into the following 6 chapters:

1. Introduction: Gives an overview of the fundamentals of gas hydrates, such as formation, occurrence, structure and stability. Methods to identify gas hydrate are also described here, as well as the importance of gas hydrates in terms of energy and environmental perspectives.

2. Study area: Introduces the study area in terms of bathymetry, oceanography, geologic development, gas hydrate occurrence and temperature development.

3. Data and methods: This chapter gives an overview and a description of the data used in the thesis as well as the applied methods.

4. Results: The seismic observations are presented and described here.

5. Discussion: The observations presented in the result chapter are discussed here. A sub-chapter including gas hydrate stability modeling is also included here.

6. Conclusion: The main conclusions and the accomplishment of the thesis are given here.

1.3 Fundamental science of gas hydrates

1.3.1 Definition and occurrence

Gas hydrates, also called gas clathrates, are naturally occurring ice-like crystalline solids (figure 1-2). They are composed of hydrogen bonded water molecules forming a rigid lattice of cages each containing a molecule of natural gas, mainly methane (Sloan, 1998[b]; Kvenvolden, 1993[a], 1995, 1998). Hydrates are typically formed when small "guest" molecules (< 0.9 nm) are in contact with water at ambient temperatures (typically less than 300 K) and moderate pressures (typically more than 0.6 MPa) (Sloan, 2003). The natural gas component of gas hydrates is typically dominated by methane, but other natural gas components (e.g. ethane, propane, CO_2) can also be incorporated into a hydrate. The origin of the methane in a hydrate can be either thermogenic or biogenic gas (Kvenvolden, 1998).

Joseph Priestly was the first who obtained gas hydrates in a laboratory in 1778, while naturally ocurring gas hydrates were proven in the 1960s in polar continental settings in Russia (Kvenvolden, 1995; Makogon, 2010). The occurrence of gas hydrates in nature is controlled by the factors of temperature, pressure, gas composition and sufficient amount of gas and water present. Gas hydrates occur world-wide, but because of the pressure-temperature and gas-volume requirements, they are restricted to two regions, polar and deep oceanic (Kvenvolden, 1998).

Figure 1-2: Chunks of gas hydrate recovered from the Gulf of Mexico in 2002 (from Winters and Lorenson, 2002).

Gas hydrates are typically found in the pore spaces of the uppermost hundreds of meters of continental margin sediments in ocean and inland seas, and in arctic permafrost areas (Vanneste et

al. 2005[a]). This thesis focus on gas hydrates in oceanic sediments, which occur where the bottom-water temperatures approach 0°C, and water depths exceed about 300 meters (Kvenvolden, 1998). The lower limit of methane-hydrate occurrence is determined by the geothermal gradient; the maximum lower limit is about 2000 meters below the solid surface, but is typically much less depending on local conditions (Kvenvolden, 1998). This implies that the ocurrence of gas hydrates is restricted to the shallow lithosphere (Kvenvolden, 1995).

1.3.2 Hydrate crystal structure

The appearance of gas hydrates is similar to that of ice and commonly resembles snow, as hydrates contain 85 % water on molecular basis (Sloan, 1998[b]). The crystalline structure, however, is different. While ice is showing a non-planar array of hexagonal rings, hydrate forms three dimensional water cages in which guest molecules reside, linked to the framework by van der Waals forces (Koh and Sloan, 2007).

The three most common hydrate structures are I, II and H, where I and II are cubic structures and H is hexagonal (figure 1-3). For natural gases, hydrate will form one of these crystallographic lattice types. The type of lattice that is formed depends on the size of the guest molecules (Sloan, 1998; Koh, 2002).
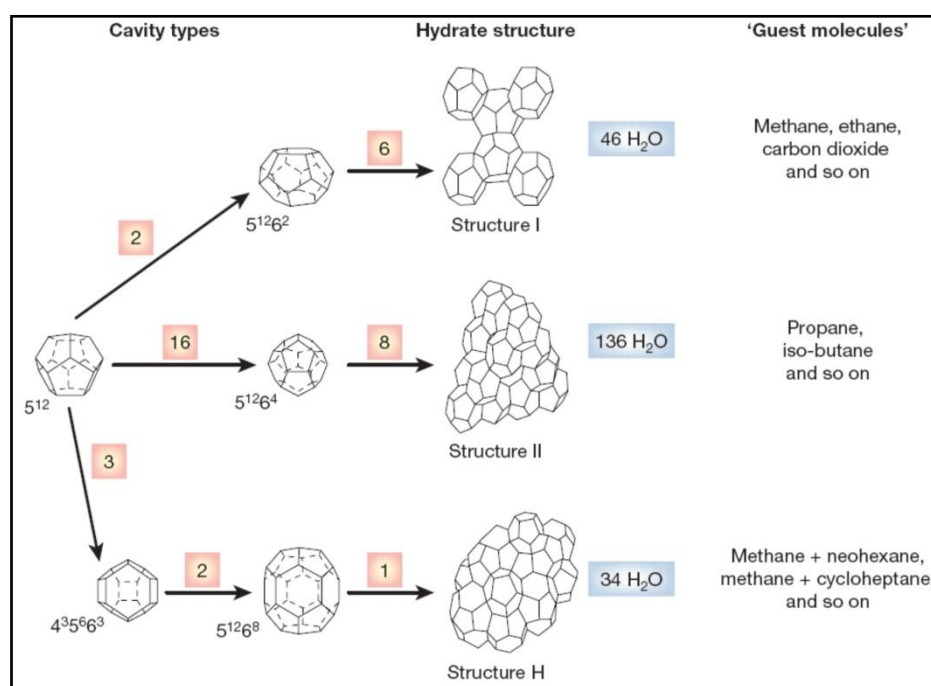
Figure 1-3: The three most common hydrate crystal structures. The descriptors (e.g. $5^{12}6^{4}$) indicates the number of pentagonal and hexagonal faces. The numbers indicated in the square fields refer to the number of cage types (From Sloan, 2003).

 Gases with the smallest molecule diameter will form structure I, and therefore contain biogenic gases such as methane, carbon dioxide, ethane and hydrogen sulfide. This makes structure I the

most common in Earth's natural environment (Sloan, 2003; Maslin et al., 2010). Gases with molecules larger than ethane, but smaller than n-butane will form structure II, which is more common in man-made environments such as hydrocarbon production and in the processing industry. The hexagonal structure H may occur in either environment, combining elements of structure I and II; encaging both small and large molecules (Beauchamp, 2004). Table 1 gives a summary of the structure and cage types of I, II and H.

Structure	I		II		H		
Crystal system	Cubic		Cubic		Hexagonal		
Cavity	Small	Large	Small	Large	Small	Medium	Large
Description	5^{12}	$5^{12}6^2$	5^{12}	$5^{12}6^4$	5^{12}	$4^35^66^3$	$5^{12}6^8$
No cavities/unit cell	2	6	16	8	3	2	1
Average cavity radius [Å]	3.95	4.33	3.91	4.73	3.91	4.06	5.71
Ideal unit cell formula	6x2y46H$_2$O		8x16y136H$_2$O		1x3y2z34H$_2$O		

Table 1: Summary of the main properties of the three main hydrate crystal structures (Modified from Sloan, 2003).

1.3.3 Formation of hydrates in marine sediments and source of gas

In order for natural gas hydrates to form, the requirements of high pressure – low temperature, sufficient and regular supply of gas, sufficient amount of water and a host rock for the hydrates to grow in must be fulfilled (Sloan, 1998[b]; Xu and Ruppel, 1999).

As mentioned, the hydrate forming methane can be of biogenic or thermogenic origin, where biogenic methane constitute most of it (Kvenvolden, 1995). The gas is generated from organic material that undergoes microbial and/or thermal alteration and degradation (Norville and Dawe, 2007). As much as 20 % of the world's natural gas resources (Rice and Claypool, 1981), and 99% of all naturally occurring hydrate is believed to be of biogenic origin (Kvenvolden and Lorenson, 2001). This is consistent with most deep-sea gas-hydrate samples (Riedel, Willoughby and Chopra, 2010). Biogenic methane formation occurs from a conversion of organic matter to methane by microorganisms through either fermentation or reduction of carbon dioxide at low temperatures and shallow depths (Riedel, Willoughby and Chopra, 2010). The microbial generation of methane is limited by the amount of pore-water sulfate and by the corresponding methane oxidation (Chand and Minshull, 2003).

Different models have been proposed for the formation of marine gas hydrates in marine sediments (Bouriak et al., 2000). Claypool and Kaplan (1974) assumed that methane is generated microbially in situ from organic matter and that the formation of gas hydrates takes place concurrent with sedimentation. In the second model, suggested by Hyndman and Davis (1992), gas hydrates are

formed by the removal of dissolved biogenic or thermogenic methane that originates from upwelling pore fluids entering the gas hydrate stability zone. A third model (Minshull et al., 1994) suggests free gas to migrate upwards through zones of higher permeability due to buoyancy, capillary forces and overpressuring mechanisms. Hydrate forms at suitable sites and are able to form a seal, trapping free gas beneath the accumulations.

There are reports from some locations where gas hydrates have components of typical thermal origin, for example in the Gulf of Mexico (Sassen et al., 2004), the Caspian Sea (Ginsburg et al., 1992) and the Black Sea (Woodside et al., 2003). Thermogenic methane is only relevant under temperature conditions of 80-90°C (Kvenvolden, 1995), where thermal conversion of organic matter to methane occurs. This implicates that gas hydrate formation from thermogenic methane only can happen if there is a rapid upward fluid flow of methane into the gas hydrate stability zone (Hyndman and Davis, 1992). Faults and fracture zones on active margins could typically act as such migration pathways for the gas (Hyndman and Davis, 1992). Gas leakage on passive margins from large hydrocarbon reservoirs has also been observed (Løseth et al., 2011).

The determination of whether a natural gas is of biogenic or thermogenic origin is frequently assessed by using carbon isotope ratios of methane as the carbon isotopic composition of biogenic methane is usually lighter than of thermogenic methane where more ethane and propane are produced (Tilley and Muehlenbachs, 2008). The ratio between ^{12}C and ^{13}C and the ratio of methane to the sum of ethane and propane are both methods that can be used (Sloan and Koh, 2008). Such geochemical analyses of gas from natural environment do not always give unambiguous results and may complicate the source identification (Floodgate and Judd, 1992).

Despite the abundance of gas hydrates in marine environments, relatively little is known about the actual hydrate formation process when it comes to hydrate nucleation and growth (Buffet and Zatsepina, 2000). Sloan and Koh (2008) presents a thorough review of these processes, only briefly presented in this thesis.

The nucleation process is the first step in gas hydrate formation, where gas and water in a supersaturated solution re-organize to form a hydrate nucleus. Before hydrate growth can happen, there is an induction time before the nucleus reach a critical cluster size which is stable. During the induction time, hydrates cannot form due to metastability (Sloan and Koh, 2008). When critical cluster size is reached the growth period of hydrate crystals can proceed in a rapid manner (Koh, 2002). The growth of hydrates will be reduced as water is being consumed (Sloan and Koh, 2008).

1.3.4 Stability and dissociation of gas hydrates

Gas hydrates are metastable compounds, meaning certain conditions must be fulfilled in order to achieve stability. At pressure and temperatures outside the hydrate stability range, dissociation of gas hydrates will occur. The dissociation of hydrates results in a change of phase from a solid to a gas and liquid (Maslin et al., 2010). Other factors, such as time dependency, soil permeability and diffusion are also affecting the dissociation process (Nixon and Grozic, 2006). On a micro-scale, the process of dissociation is fundamentally different from that of hydrate formation (nucleation and growth). As hydrates require long time to initiate, dissociation can happen quite fast when the hydrates are brought out of the stability zone. This is explained by the effect of entropy which favors disorder in a system rather than order. It will therefore take longer time for gas and liquid, which are disorderly arranged, to arrange into an orderly hydrate structure than it will take for the structure to decompose (Sloan and Koh, 2008).

The zone where gas hydrates are stable is called the gas hydrate stability zone (GHSZ) and is typically observed in the upper few hundred meters of sediments. The GHSZ is defined as a part of a geologic section, limited from above the seafloor, where gas hydrate can exist under in-situ conditions (Ginsburg and Soloviev, 1997). It is common practice to locate the base of this zone using depth (pressure) – temperature diagrams (figure 1-4). The sub-bottom depth of the GHSZ depends on the geothermal gradient, bottom-water temperature, pressure (water depth), gas composition, pore-water salinity, and the physical and chemical properties of the host rock (Bünz et al., 2003). To be able to predict the thickness of the GHSZ, knowledge about these parameters are necessary as a change in any of these could result in lowering/lift of the base of the gas hydrate stability zone (BGHSZ). The thickness of the GHSZ will for example increase with increasing water depth (pressure) if the geothermal gradient is constant, while an increase in geothermal gradient will lead to a lift of the BGHSZ thus decreasing the thickness of the GHSZ (Kvenvolden and Barnard, 1983). Concerning the gas-composition, the presence of gases with high molecular weight such as ethane, butane and propane will increase the thickness of the GHSZ (Sloan, 1998[a]).

The GHSZ extends oceanward, with increasing water depth, but thins in areas of high geothermal gradient such as mid-ocean ridges or hot spots. As a result, the potential area of hydrate formation is a narrow subset of the sedimentary zone of hydrate stability that excludes both seawater and sub-abyssal sediments and lies mostly beneath continental slopes in water depths exceeding 500 meters (Beauchamp, 2004).

The phase equilibrium envelope is calculated on the basis of the guest composition, the presence of inhibitors such as salts, the presence of water and the P-T conditions. Specific software packages have been developed for routinely calculations of this purpose such as CSMHYD (Sloan, 1998[b]).
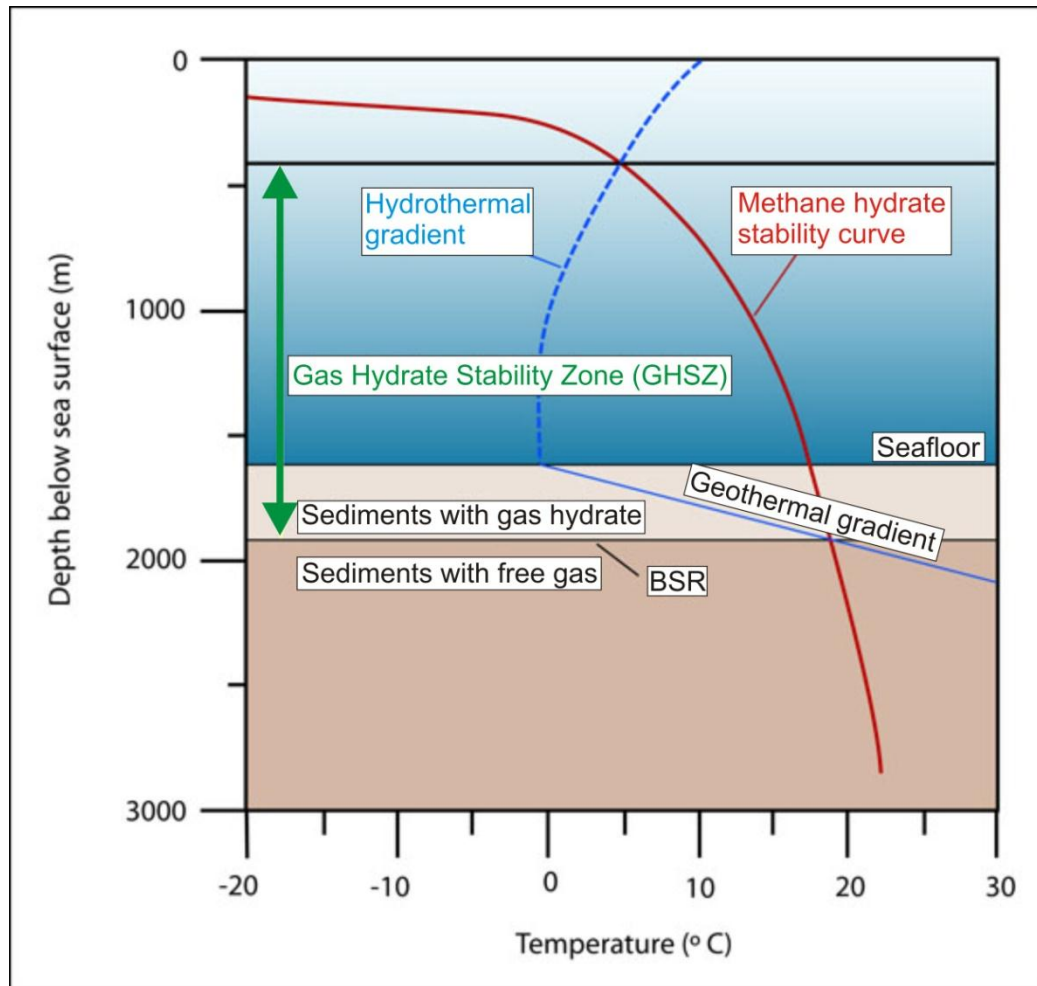
Figure 1-4: Phasediagram for the transition of gas hydrates in solid phase and free gas. When the temperature and pressure is beneath the phase boundary (blue dotted line), the gas hydrates are stable. When P-T conditions lies above the phase boundary, the gas hydrates will be unstable and fluids will occur as free gas or water. The transition is marked with a red line. At the transition between the GHSZ and free gas phase, the bottom simulating reflector (BSR) can be observed (Modified from Chand and Minshull, 2003).

1.4 Identification of gas hydrates

Geophysical exploration is an important approach to determine the presence of gas hydrates, where the seismic reflection technique is the most widely used method for remotely detecting and quantifying gas hydrate beneath continental margins (Westbrook et al., 2008). Together with the seismic method, associated processing and imaging techniques follows. The presence of gas hydrates within sediments increases the bulk and shear modulus, and thus the P- and S-wave velocities. The S-wave velocity (V_s), however, is only expected to change if hydrate cements the sediment, thereby altering the shear moduli of the sediment. The P-wave velocity (V_p) will change when hydrates are present, whether they occur in pore space or as a cementing material (Chand and Minshull, 2003). 1700-2400 m/s are typical V_p values for gas hydrate bearing sediments (Andreassen et al., 1990). The presence of free gas will also have a significant impact on the physical properties of sediments. Even small amounts of free gas will reduce V_p drastically, typically below 1500 m/s. The changes in the physical properties of sediments caused by gas hydrates and/or free gas result in geophysical anomalies in seismic imaging such as for example bright spots (Riedel, Willoughby and Chopra, 2010).

When gas hydrates forms, they occupy pore space in the sediments above the base of the gas hydrate stability zone (BGHZ), which causes reduced porosity and permeability within the sediment. High gas hydrate saturation in the sediments can form a nearly impermeable sequence acting as a barrier, leading free gas to accumulate below the GHSZ (Sain et al., 2000). The base of the gas hydrate stability zone (BGHSZ) represents the phase boundary between stable gas hydrates and free gas below. As a consequence, a sharp contrast in acoustic impedance[1] exist due to higher velocities in the hydrate-bearing sediments overlying lower velocities resulting from gas-filled pore spaces (Hornbach et al., 2003; Bünz et al., 2003). This boundary can easily be identified on reflection seismic data where it is known as bottom-simulating reflection (BSR) (figure 1-5), and provides indirect evidence for the existence of gas hydrates in sediments (Shipley et al., 1979; Kvenvolden, 1993[b]; Bünz and Mienert, 2004; Hustoft et al., 2007).

BSRs therefore approximate an isotherm, and as a result of its pressure – temperature dependence the BSR regularly mimics the seafloor (hence the name), crosscutting dipping strata showing that it is not a bedding plane reflection (Hornbach et al., 2003).

---

[1] Acoustic impedance (Z): For a given material it is defined as the product of its density (ρ) and seismic velocity (v). It varies among different rock layers, and the difference in acoustic impedance between the different rock layers affects the reflection coefficient which describes how much energy being reflected (Schlumberger, 2011).
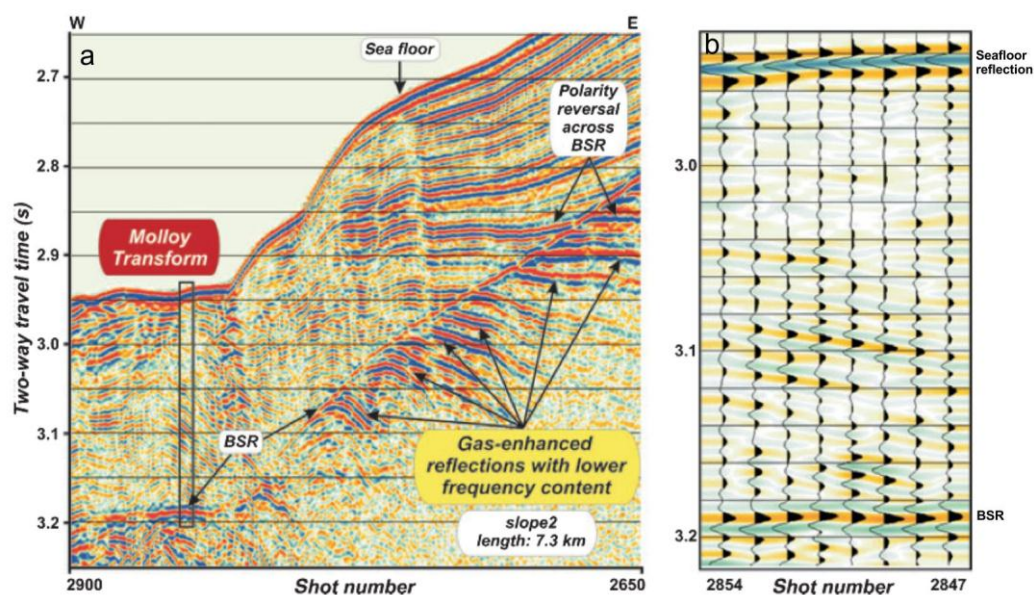
Figure 1-5: a) Illustration of a BSR showing the characteristics of crosscutting of sedimentary strata and a simulating trend to the seafloor reflection. b) Wiggle trace display illustrating the high reflection amplitude of the BSR and its reversed polarity relative to the seafloor reflection, taken from the area marked with a black box in a) (modified from Vanneste et al., 2005[b]).

The BSR shows reversed polarity relative to the seafloor reflection, which indicates the decrease in acoustic impedance (Andreassen et al., 1997). Due to the negative acoustic impedance contrast, the BSR often shows enhanced seismic amplitudes (Bünz et al., 2003; Vanneste et al., 2005[b]). Gas hydrate accumulations are geophysically inferred from the presence of a BSR, even though hydrates might exist without a BSR if no gas is trapped underneath it (Ecker et al., 2000; Mienert et al., 2005; Bünz et al., 2003; Haacke et al., 2007).

Recent studies suggest that most of the BSR amplitude is due to the velocity reduction of the underlying free gas (e.g. MacKay et al., 1994; Holbrook, 2001; Hyndman et al., 2001; Pecher et al., 2001) (figure 1-6). The presence of a free-gas zone (FGZ) is an important part of the gas-hydrate system. It is in particular important if the presence of gas hydrate is to be inferred from BSR observations (Haacke et al., 2007).
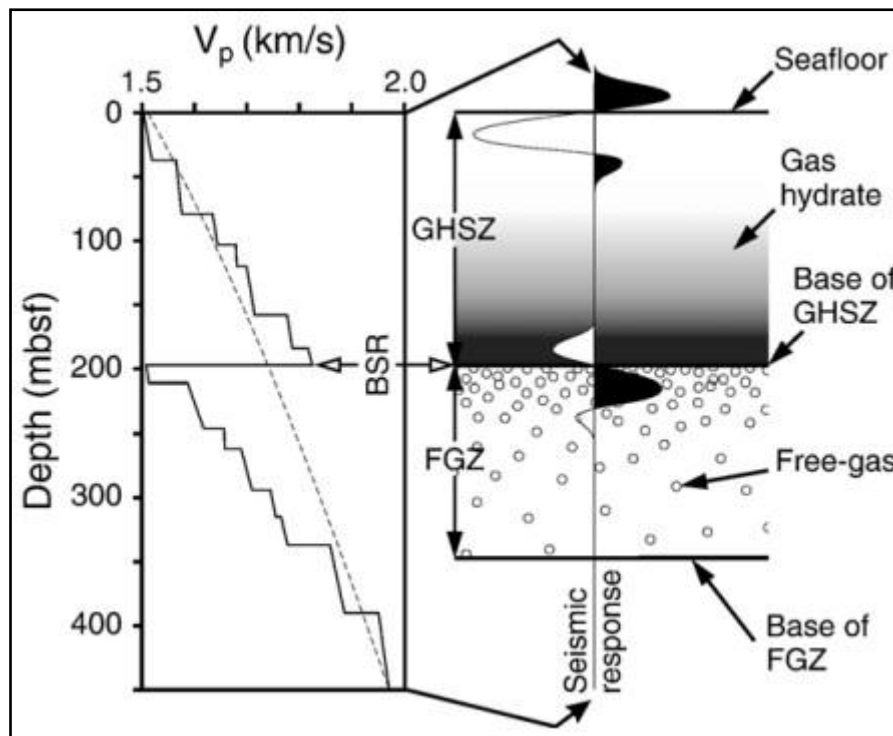
Figure 1-6: Illustration of a submarine sedimentary section containing gas hydrate above the BSR and free gas below the BSR. The BSR marks the base of the GHSZ. The P-wave velocity profile (V_p) is from a site west of Svalbard (Westbrook et al., 2005) and indicates a thick sub-BSR free-gas zone (FGZ) with downward-decreasing concentration of free gas. The dashed line is an empirical velocity curve for soft terrigenous muds (Hamilton , 1980), shown for comparison (From Haacke et al., 2007).

BSRs can also be observed as the result of diagenesis in silica rich sediments, from the transformation of Opal A to Opal CT, and Opal CT to quartz. This process however, gives a positive acoustic impedance contrast, resulting in a bottom simulating reflection with the same polarity as the seafloor, thus it can be distinguished from hydrate related BSRs (Hein and Scholl, 1978).

The identification of BSRs provides an easily recognizable indicator of the presence of gas hydrate, but it does not provide information directly on the concentration of hydrate or its distribution in the region between the BSR and the seafloor (Westbrook et al. 2008). Furthermore, BSRs provide no information about the reservoir quality, and is therefore not a fully reliable stand-alone tool when it comes to exploration of gas hydrates (Riedel, Willoughby and Chopra, 2010).

As the BSR only identifies the potential presence of gas hydrates, additional methods can be used for a more comprehensive study giving more detailed seismic analysis. Deploying seismic receivers on the seafloor, such as ocean bottom cable (OBC), -seismometers (OBS) and –hydrophones (OBH), can provide additional information as the structure of the subsurface can be inferred in more detail. Compared to surface-towed streamers these methods have a major advantage as they record shear waves which gives an additional control on the estimation of gas hydrate concentration in the sediments as well as noise reduction (Chand and Minshull, 2003; Riedel, Willoughby and Chopra,

2010). The use of vertical seismic profiling (VSP) allows measurements to be taken inside the wellbore using geophones. This gives the opportunity to measure in situ velocities of hydrate bearing sediments using seismic frequencies (Holbrook et al., 1996). The BSR depth can also easily be determined (Chand and Minshull, 2003). Sonic logging makes it possible to identify the presence of gas hydrates in situ by measuring the elastic wave properties of the formation. The sonic velocities are affected by the presence of free gas and hydrate, increasing and decreasing respectively. Sonic logs can therefore be used to support seismic interpretation and even quantify hydrate and gas concentrations (Guerin and Goldberg, 2002). As for understanding the free gas effect on the BSR, amplitude versus offset (AVO) analysis is a useful method (Andreassen et al., 1997).

1.5 Heat flow

On a global scale heat flow reach highest values along tectonic plate boundaries (e.g. the Mid-Atlantic Ridge), where local variations in fluid flow will affect the regional geothermal gradient (Mottl and Wheat, 1994). Gas hydrate related BSRs can be used to derive heat flow estimations, thereby give information about the thermal structure below the seafloor (Yamano et al., 1982). Such information can be used to enlighten issues related to fluid expulsion processes, heat transport mechanisms, sediment overburden and its influence on the lithosphere, and evaluation of continental margins (Shankar et al., 2004).

The stability of gas hydrates has been proven to be more sensitive to changes in temperature than in pressure (Ruppel, 2000; Mienert et al., 2005). It is therefore vital to investigate the thermal regime in a gas hydrate reservoir in order to predict the stability of the hydrates in a given depositional environment. Heat flow values through the seafloor are commonly calculated by the product of the geothermal gradient and the thermal conductivity of the upper part of the sediments (Mottl and Wheat, 1994). The thermal conductivity describes a materials ability to conduct heat, and for hydrates and hydrate bearing sediments it is often determined by laboratory measurements (Ruppel, 2000). The thermal conductivity is usually related to the age of the oceanic crust and thus a given spreading rate. Assuming a constant thermal conductivity in the sediments, a connection between the age of the oceanic crust and the geothermal gradient can be derived (Miles, 1995).

The geothermal gradient within the sediments is the most influential parameter in determining the thickness of gas hydrate formation (Miles, 1995). A conventional method of measuring the thermal gradient is by measuring the temperature in the upper few meters of the sediments using a probe. The geothermal gradient can be extrapolated downwards using these measurements. This technique's sensitivity to ocean bottom water temperature variations is however a weakness (Lucazeau et al., 2004). In areas comprising gas hydrates, these types of measurements will not

include direct measurements from the gas hydrate reservoir, often localized several hundreds of meters below the seafloor.

Direct measurements of the geothermal gradients can also be accomplished. Such measurements can be obtained from temperature logs, Bottom Hole Temperature (BHT) and temperatures of fluid during Drill Stem Test (DST). Such methods are often accomplished for industrial purposes, e.g. oil exploration boreholes (Lucazeau et al., 2004). There are, however, sources of errors that must be considered deploying these methods. Large temperature perturbations are related to drilling, thus making temperature logs less reliable. BHT is less perturbed by drilling and corrections can be made. DST is considered even more reliable as the fluid temperatures are measured in situ (Lucazeau et al., 2004).

As heat flow measurements in marine environments are cost-prohibitive, heat flow and geothermal gradients could be derived from the location of the BSR on reflection seismic sections. A method to estimate heat flow derived from gas hydrates was suggested by Yamano et al. (1982). When a gas hydrate related BSR is identified, the basic data on pressure, temperature and composition as a function of the phase boundary are relatively well known. Based on the assumption that BSRs mark the base of the gas hydrate stability field, it is possible to use seismically determined depth information to estimate in situ BSR temperatures and thereby to calculate heat flow through the uppermost sedimentary column. Heat flow estimates using BSRs require estimates of the temperature and pressure of the BSR, seafloor temperature, and the in situ thermal conductivity profile between the seabed and the BSR. The pressure at a BSR can be calculated based on its depth below the seabed and the corresponding temperature can be obtained using the gas hydrate P-T diagram (Townend, 1997).

The accuracy of such heat flow estimates depends upon velocity information above the BSR, pore-water salinity, gas molecular composition, choice of hydrate system considered and the type of conductive regime assumed (Shankar et al., 2004). The cumulative effects of uncertainties associated with the determination of the thermal gradient and thermal conductivity structure between the seafloor and the BSR are reported to be 10-30 % (Yamano et al., 1982; Minshull and White, 1989; Ashi and Taira, 1993; Townend, 1997; Grevemeyer and Villinger, 2001). If additional measurements of the temperature at the BSR can be constrained by heat probe measurements, the resulting uncertainty of the assessment can be within 5-10 % (Grevemeyer and Villinger, 1997).

1.6 Importance of gas hydrates

The importance of gas hydrates has only been realized in the last two decades even though the British scientist Sir Humphrey Davy defined the substance for about 200 years ago. In the following century gas hydrates did not attract much attention and was considered as a chemical oddity. In the 1930s, the oil and gas industry discovered that gas hydrates caused clogging of pipelines during low temperature conditions (Maslin et al., 2010). In the 1950s, the first two structures of gas hydrates were described, and in the 1970s it was suggested that there must be vast quantities of gas hydrates on earth. This postulation was made by Russian scientists based on theoretical models (Tucholke et al., 1977).

It has been estimated that more carbon is contained in gas hydrates than in any other carbon reservoirs on Earth. Gas hydrates exist on continental margins worldwide and there has been an increasing interest in the substance for the last decades. The academic and industrial interest in gas hydrates is primarily for three reasons:

1. Gas hydrates as a potential energy resource

The world energy system of today is dependent on hydrocarbons, oil in particular, but increasingly also natural gas. As much as 80 % of the global energy supply is of fossil origin (Krey et al., 2009). Considering the whole planet, the quantity of natural gas hydrate deposits greatly exceeds the conventional natural gas resources. Enormous amounts of methane is apparently sequestered within clathrate structures at shallow sediment depths within 2000 meters of Earth's surface and is widely geographically distributed (Kvenvolden, 1993[b]). As a result from national programs for research and production of natural gas from gas-hydrate deposits, over 220 deposits have been discovered worldwide (Makogon et al., 2007). Figure 1-7 shows a map of discovered gas hydrate deposits.
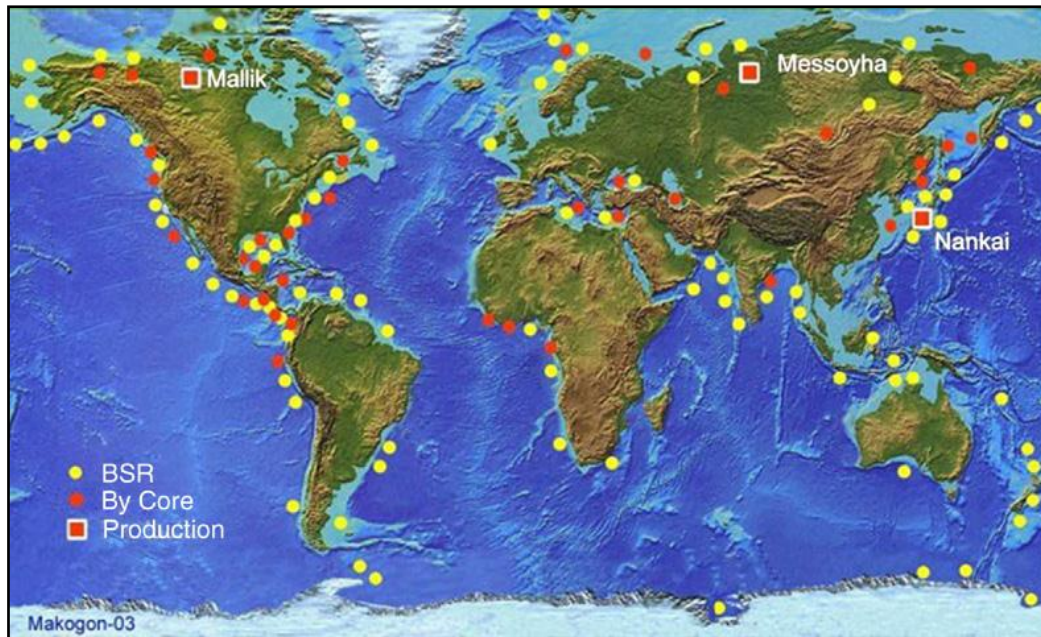
Figure 1-7: Map showing the distribution of discovered gas hydrate deposits (From Makogon, 2010).

Gas hydrate is considered as an unconventional source of gas together with coal bed methane and gas in shale (Boswell, 2009). One of the aspects that make gas hydrates interesting as an energy source is the energy density (volume of methane at standard conditions per volume of rock) which is 10 times higher than the energy density of other unconventional sources of gas, and 2-5 times higher than the energy density of conventional natural gas (Kvenvolden, 1993[b]). Where methane is the hydrate forming gas, 1 m^3 of solid crystalline hydrate can give about 164 m^3 of methane at STP (Max, Johnson and Dillon, 2006). Because of this large gas-storage capacity, gas hydrates are thought to represent an important source of natural gas (Pierce and Collett, 2004).

Several estimates of the global amount of gas hydrates have been suggested in recent years, covering a wide range and are considered highly uncertain (Lerche, 2000; Collett, 2002; Milkov, 2004; Sloan and Koh, 2008). Despite the wide range of estimates and the fact that the numbers have dropped due to the addition of new data past the years, even the lowest and most conservative estimates suggest very large volumes of hydrate accumulations (Collett, 2002; Milkov, 2004; Boswell, 2007). As much as 10^{19} g of carbon is believed to be trapped mostly as methane within solid gas hydrates. This is equal to approximately a 40 meter thick blanket of methane covering the entire surface of Earth (Kvenvolden, 1988). MacDonald (1990) and Kvenvolden (1998) suggest an estimate for the total amount of gas hydrate stored on Earth to be about 2 x 10^{16} m^3, which gives

approximately 15 x 10^{12} toe[2] of hydrated gas on Earth. A production of 17-20 % of this resource can be a sufficient supply of energy for 200 years (Makogon, 2010).

Mostly, countries with limited hydrocarbon resources have been the main investors in gas hydrate research, where the potential of gas hydrate to become a major energy resource has been the primary motive power (Boswell, 2009). However, the development of methods to recover methane from hydrates leading to commercialization has been slow. Both economic and technological issues are inhibiting factors concerning the development. Gas hydrates will only become a potential energy resource when it can be shown that the cost of the energy required to release methane from the hydrate is significantly less than the economic value of the methane that can be recovered from the dissociated gas hydrate deposits (Kvenvolden, 2006). Solving the substantial economic and technological obstacles, gas hydrates could be able to meet future energy demands as well as functioning as an important "bridging" fuel in the transition to sustainable energy supplies of the future (Boswell, 2009).

2. Gas hydrates as a critical factor for global climate change

Methane is an atmospheric trace gas, which influences chemical processes and species in the troposphere and stratosphere (Badr et al., 1991). Because methane is radiatively active, it is a greenhouse gas, and it has a global warming potential (GWP)[3] 20 times larger than an equivalent weight of carbon dioxide when integrated over a 100 year span of time (Kvenvolden, 1993[a]). In the atmosphere, it takes about a decade for methane to be oxidized to CO_2, which also is a greenhouse gas which can continue to impact the climate for many millennia (Archer et al., 2009).

Nisbet (1990) has suggested that the release of methane from hydrates to the atmosphere may have contributed to the warming at the end of the last major glacial period. The release of methane from destabilized gas hydrate may contribute to global warming also in the future and may represent a factor in future human-induced climate change (Kvenvolden, 2006; Krey et al., 2009).

A hypothesis concerning the global climatic effect of large methane release from hydrate dissociation was published by Kennett et al. (2003). The "Clathrate Gun Hypothesis" suggests that the dissociation of methane hydrates likely induced rapid global warming at various times in the geologic past resulting from changes in sea level and sea-water temperature. Such large methane

---

[2] Toe = tonne of oil equivalent. Defines a unit of energy from which is released by burning one tonne of crude oil. 1 toe corresponds to 42 GJ (OECD, 2011).
[3] GWP was developed to compare the ability of each greenhouse gas to trap heat in the atmosphere relative to another gas. The definition of GWP for a particular greenhouse gas is the ratio of heat trapped by one unit mass of the greenhouse gas to that of one unit mass of CO_2 over a specified time period (U.S. Energy Information Administration, 2011).

releases could result in further global warming leading to even more dissociation of methane hydrates enhancing global warming by a positive feedback loop.

In contradiction, Kvenvolden (2000) emphasize that the role of hydrates concerning global climate change is uncertain, because in order for methane to be an effective greenhouse gas, it must reach the atmosphere. Further he points out that there are several obstacles to the transfer of methane from hydrate to the atmosphere. The suggested limiting factors are the rates of hydrate dissociation, gas migration and trapping in sediments, and gas venting into the water column. Methane that dissolves in the deep ocean oxidizes to CO_2 and remains in solution until the water mass equilibrates with the atmosphere, releasing some 15-20% of the carbon to the air (Valentine et al., 2001; Archer et al., 2009). Another important factor is anaerobic methane oxidation, where a significant amount of globally produced methane is converted to CO_2 in marine sediments. Methane is being consumed in anoxic sediments where archaea is suggested to reverse the methanogenesis by interaction with sulfate-reducing bacteria (Boetius et al., 2000). Sulfate is the terminal electron acceptor in the zone of anaerobic oxidation of methane according to:

$$CH_4 + SO_2^{2-} \rightarrow HCO_3^- + HS^- + H_2O$$
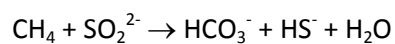
This means that a possible climate impact of dissociated hydrates in the ocean depends on whether the carbon reaches the atmosphere in the form of methane or if it remains in place below the seafloor (Archer et al., 2009).

Even though there is some disagreement among scientists concerning gas hydrates related to climate change, it seem to be a broad agreement that large amounts of gas hydrates are stored within Earth's crust, and that it is important that the distribution of gas hydrates and their sensitivity to environmental changes are studied and better understood. Gas hydrate systems in polar latitudes may be of particular importance due to the fact that environmental changes will be felt here first and most likely are more extreme than elsewhere (Bünz et al., 2008).

3. Gas hydrates as a submarine geohazard

As mentioned, submarine gas hydrates are stable in ocean sediments under appropriate pressure- and temperature conditions and dissociation will occur if the hydrates become unstable. A destabilization can be caused for example by an increase in ocean temperature or a reduction in pressure due to sea-level fall. Such dissociation of submarine gas hydrates has been suggested as a contributing factor when it comes to sediment failure (Mienert et al., 2005).

McIver (1982) was the first who suggested the link between gas hydrate dissociation and submarine slope failures (figure 1-8). Lowering of sea level or continuing sedimentation are factors that can induce dissociation of hydrates at the base of the hydrate layer. This can result in a loss of cementation, gas production and overpressurization, leading to a glide plane where massive wedges of hydrate-cemented sediment can slide (Grozic, 2009).

Dillon and Max (2000) suggest three criteria that must be met in order for decomposing gas hydrates to be a widespread cause of slope failure; (1) Gas hydrates must be widespread. (2) Slides must have originated in areas that are within the gas hydrate phase boundaries. (3) Soils of low permeability must be common at the base of the hydrate zones in order to permit the build-up of excess pore pressure that could lead to unstable slopes during sea-level falls.

Slope failure is considered as a hazard to underwater installations, pipelines and cables and in extreme scenarios, to coastal populations through the generation of tsunamis (Maslin et al., 2010).
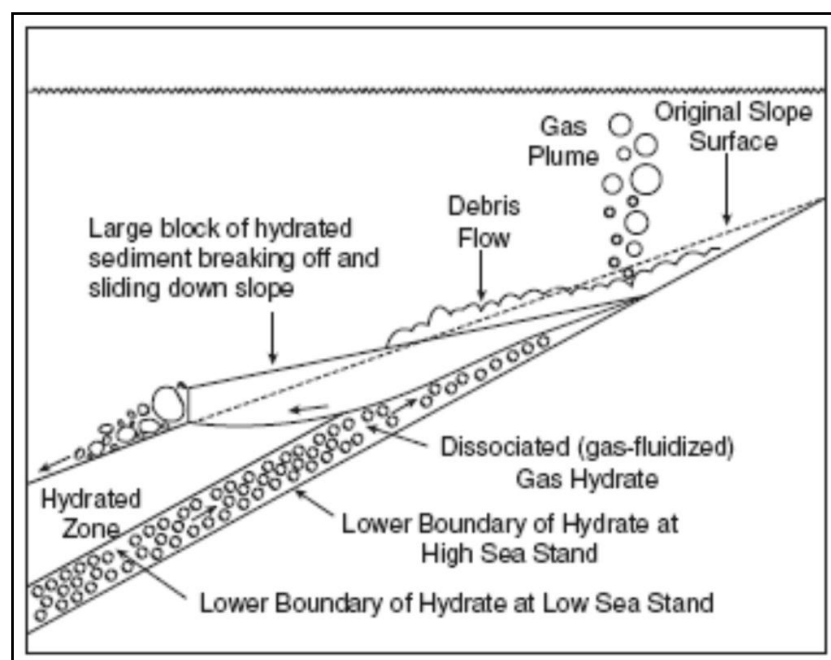
Figure 1-8: Diagram showing the effects of changes in sea level on submarine gas hydrate and the resulting failures and gas release (McIver, 1978).

Gas hydrates may also constitute a hazard for drilling and production operations (Collett and Dallimore, 2002). The problems that may arise under such operations can be different between onshore and offshore operations, but they stem from the same characteristic of gas hydrate which includes dissociation in the case of pressure decrease and/or increases in temperature. The dissociation of the hydrates can lead to a rapid release of large amounts of gas into the well bore during the drilling operation, threatening the safety of personnel and the surface equipment (Folger, 2010).

18

2. Study area

The study area is located at the western Svalbard margin on the continental slope, north of the Knipovich Ridge and east of Molloy Transform Fault (MTF), including the Vestnesa Ridge (figure 2-1). The area is stretching out up to 140 km from the shelf edge, down the continental slope, from the middle part of the Svalbard margin to the MTF. The shelf edge lies at depths from 250-400 m and the continental slope is gently dipping in the south and steepens towards the north (Myhre and Eldholm, 1988). The Norwegian – Barents – Svalbard continental margin is a dynamic area showing abundant evidence of fluid migration processes, submarine mass wasting, fan development, cold water reefs, faulting, hydrocarbon accumulation, and the inferred presence of gas hydrates (Vanneste et al., 2005[a]).
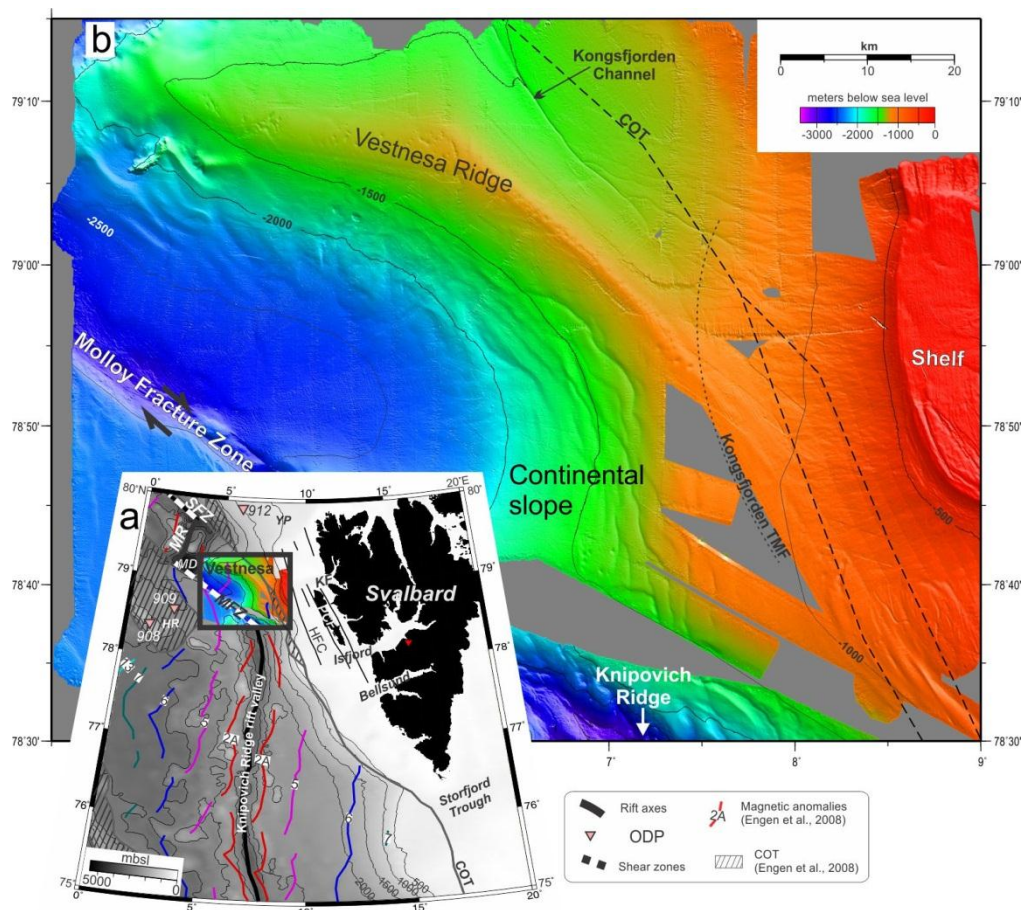
Figure 2-1: a) Bathymetric map of the study area including the eastern Fram Strait and the western Svalbard margin with the location of the Vestnesa Ridge in the black frame. Abbreviations; SFZ, Spitsbergen Fracture Zone; MD, Molloy Deep; HFC, Hornsund Fracture Complex; YP, Yermak Plateau; HR, Hovgård Ridge; KF, Kongsfjorden; PCF, Prins Carls Foreland (modified from Jakobsson et al., 2000). b) Swath bathymetry shows the morphology of the Vestnesa Ridge in detail. Continent ocean transition (COT) is marked with a dashed line (modified from Hustoft et al., 2009).

2.1 Localization and bathymetry

The Knipovich Ridge represents the northernmost extension of the active mid-Atlantic Ridge system (figure 2-1). It is extending in N-S direction at a water depth of 2300 m and is localized asymmetrically in the Norwegian-Greenland Sea, abutting the lower slope of the western Svalbard margin at 78.5°N in the Fram Strait (Thiede et al., 1998; Bünz et al., 2008). It is an ultra-slow spreading, approximately 550 km long, transform-free segment which links the MTF at its northern end and the Mohns Ridge at its southern end. The spreading rate is calculated to ~15-17 mm/year. (Crane et al., 1988; Okino et al., 2002). The Knipovich Ridge offsets westward and intersects with the MTF, where it continues within the Molloy Ridge and connects with the Gakkel Ridge in the Arctic Ocean through a complex system of transform faults and short spreading centres (Crane et al., 2001). The presence of extensional faults, suggest that the Knipovich Ridge is propagating northwards as a buried feature (Crane et al., 2001). The topographically rough areas at the Knipovich-, Molloy- and Hovgård Ridges divide the deep-water area in the Fram Strait into four separate sedimentary basins; the western Svalbard (Spitsbergen) slope and rise east of the Knipovich Ridge, the Vestnesa depocenter east of the Molloy Ridge together with the Yermak Plateau, the Greenland-Spitsbergen Sill located between the Hovgård Ridge and the MTF, and the Boreas Basin (Eiken and Hinz, 1993).

The present-day topography of the western Svalbard margin is partly influenced by the underlying bedrock topography and partly by the moulding by late Cenozoic glacial erosion (Faleide et al., 1996). Relatively shallow banks at 100-200 m depth characterize the bathymetry in the shelf area. Troughs reaching depths of approximately 400 m separate the banks. The troughs are acting as the westerly continuation of fjords in Svalbard that extends across the shelf (Faleide et al., 1996). The most prominent troughs are the Bellsund-, Isfjorden- and Kongsfjorden Troughs. At the mouth of each trough, sedimentary deposits described as "Trough Mouth Fans" are found (Vorren et al., 1989, 1997, 1998). The size of the fans reflects the size of the troughs and their corresponding drainage area (Vorren et al., 1998).

2.2 Oceanography

The Norwegian-Greenland Sea is influenced both by the North-Atlantic Current (NAC) and the Norwegian Coastal Current (NCC), which are both important agents concerning the northern hemisphere climate. The area is climatically very sensitive, and the effect of global warming is assumed to be pronounced here (Overpeck et al., 1997). The water of the Atlantic is relatively warm and saline (>5 °C and >35 ‰) and enters the Nordic seas through the northward-flowing NAC (Hansen and Østerhus, 2000; Klitgaard Kristensen et al., 2003). The Atlantic water is carried along the Norwegian continental margin in northeastward direction and forms the Norwegian Current (NC). The water is entering the Polar Sea through the Fram Strait, which plays an important role for the circulation of water masses between the Arctic Ocean, the Norwegian-Greenland Sea and the rest of the world oceans (Thiede et al., 1990; Eiken and Hinz, 1993; Hebbeln et al., 1998). Two surface currents dominate the Fram Strait; the warm and northward flowing West-Spitsbergen Current (WSC) and the cold and southward flowing East-Greenland Current (EGC). The EGC carries polar water south, into the North Atlantic, along the Greenland margin, while Atlantic waters flow along the western Svalbard margin as part of the WSC, entering the Fram Strait (Howe et al., 2008). The Atlantic water is relatively warm and saline which keeps the area free of ice (Aagaard et al., 1987). Figure 2-2 shows the present-day circulation pattern in the northern North Atlantic.
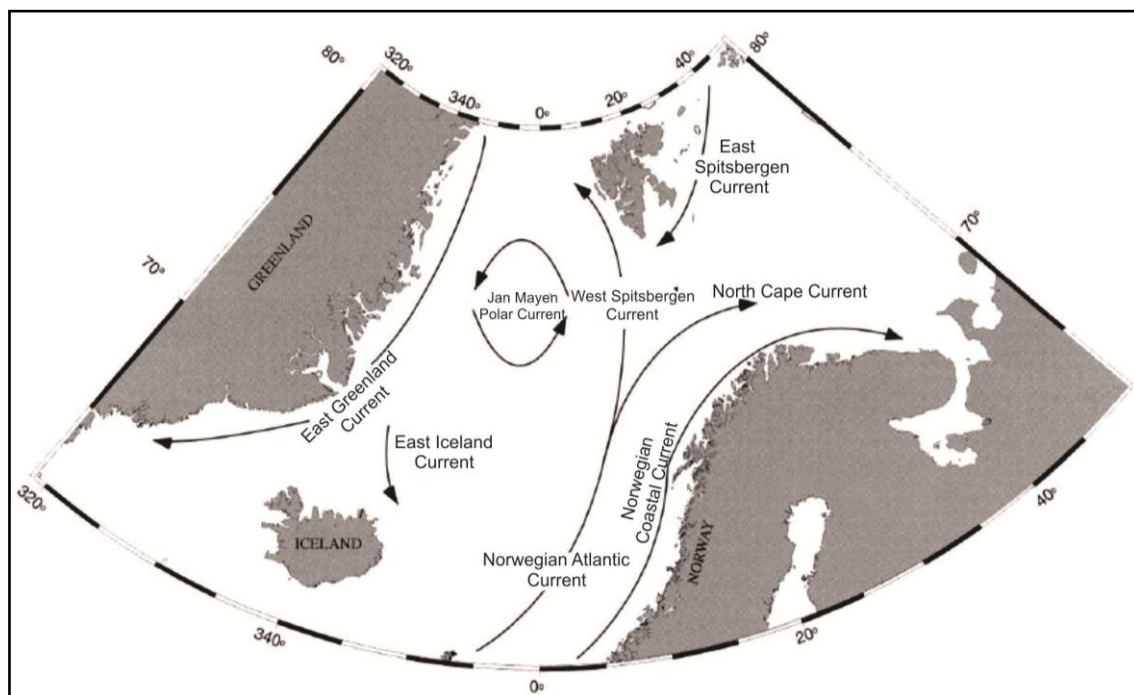

Figure 2-2: Present-day circulation pattern in the northern North Atlantic (modified from Butt et al., 2000).

2.3 Geologic development

Paleozoikum to mesozoikum: In early Devonian time young rocks of Caledonian age, dominating the northern and western part of the Spitsbergen archipelago, were eroded and deposited on Svalbard and East Greenland. The establishment of north – northwestern structural lineaments probably reactivated by subsequent tectonic events happened during these times (Birkenmajer, 1981). A change in the compressional system to a sinistral strike-slip motion took place along the older lineaments in the Late Devonian times (Birkenmajer, 1975). This was an unstable period that lasted throughout Carboniferous and Early Permian time. A stable platform was established in the Late Permian times (Birkenmajer, 1981).

Tectonic stability characterized the Mesozic and relative change in sea level is indicated by a succession of marine and continental sediments (Myhre and Eldholm, 1988). In late Cretaceous times, Svalbard underwent regional uplift that may have been the initial stage of the opening of the adjacent ocean basins (Talwani and Eldholm, 1977).

Cenozoikum: Svalbard is bordered by passive continental margins on the north and west, which evolved during the Tertiary. The margins are in particular related to the history of rifting and seafloor spreading in the Norwegian – Greenland Sea and the Eurasia Basin (Myhre and Eldholm, 1988). The seafloor spreading started at the Paleocene – Eocene transition (Talwani and Eldholm, 1977), and Faleide et al. (1996) date the event to approximately 57 Ma. It continued into the northern Greenland Sea at around 35 Ma, through a change in orientation of the opening direction (Faleide et al., 1996).

Both tectonic and sedimentary processes have influenced the passive rifted and sheared Norwegian-Svalbard margin during the Cenozoic (Myhre and Eldholm, 1988; Vorren et al., 1998). In the early Eocene, breakup followed by seafloor spreading took place in the south of the Norwegian-Greenland Sea. In the Oligocene a change in plate movements led to rifting along the continental transform between the Barents Sea and Greenland. This in turn, led to the northwards, stepwise propagation of and spreading along the Knipovich Ridge, in which culminated in the continental separation of Greenland and Svalbard (Lundin and Doré, 2002). Since Oligocene time oceanic crust has been formed along the whole Barents Sea margin followed by subsidence and the accumulation of a thick Late Cenozoic sedimentary wedge fed by erosional products from the Barents Shelf and Svalbard (Faleide et al., 1996).

After the plate movement between Svalbard and Greenland changed from strike-slip to oblique divergence at approximately 35 Ma, the Fram Strait developed, which is the only deep-water passage between the Arctic Ocean and the Atlantic Ocean (Eiken and Hinz, 1993).

After the opening of the Fram Strait, the margin has been further shaped by movement of the Fennoscandian and Barents Sea ice sheets. During the Late Pliocene and Pleistocene, glaciers reached the shelf break frequently (Vorren et al., 1998).

2.4 Vestnesa Ridge

At 80° N, north of the Knipovich Ridge and east of the MTF, the Vestnesa Ridge is located. It is a SE-NW to E-W bending elongated sediment drift of post late-Miocene. The drift is 120 m high and 5 km in lateral extent (Howe et al., 2008). The topographic shape of the Vestnesa Ridge, the sediment thickness, varying from 1 km in the west to >2 km in the east, and the internal seismic-reflection structure indicates that it is a sediment drift formed by bottom currents (Eiken and Hinz, 1993; Vogt et al., 1994; Ritzmann et al., 2004). The sediments are covering several hundreds of meters and are lying in close distance (40 km) to the 20 Ma young western Svalbard margin, where the relatively warm and northward directed western Spitsbergen current is shaping the morphology of the Vestnesa Ridge (Bünz et al., 2008). Vogt et al. (1994) described the origin of the Vestnesa Ridge as the result of a gas-hydrate cemented "carapace" allowing sediments to accumulate in a mounded form. Vogt (1986) suggested that the ridge is underlain by a basement high of oceanic crust of age estimated to range from ~3 Ma in the west to ~14 Ma in the east.

2.5 Sedimentation and seismic stratigraphy

Solheim et al. (1998) identified four main depositional facies based on the interpretation of seismic data acquired from the Svalbard – Barents Sea margin. These are represented by hemipelagic, glaciomarine sediments, sandy, silty debris flows, diamictic debris flows and tills deposited directly beneath grounded ice. The regions of net downslope sedimentation are dominated by debris flows and turbidites (Howe et al., 2008). Between the TMFs, the sedimentation on the margin is controlled by alongslope currents and hemipelagic deposition producing sediment drifts and thick draped sediments (Vogt et al., 1999; Howe et al., 2008).

Eiken and Hinz (1993) suggested that the West-Spitsbergen Current has affected the sedimentation in large parts of the Fram Strait since Late Miocene, and that contourites of Late Miocene to Quaternary age has been deposited.

Faleide et al. (1996) identified seven regional seismic reflectors (R7-R1) between the seafloor and the oceanic basement along the outer Svalbard-Barents margin. The R7 reflector is the oldest (2,3

Ma) and marks the onset of extensive continental shelf glaciations (Faleide et al., 1996). The seismic units show variation along the margin when it comes to thickness and internal seismic reflection patterns. The stratigraphic subdivision of the western Svalbard margin by Schlüter and Hinz (1978) (SP-III to SP-I sequences) show that the base of SP-II corresponds to reflection R6 of Faleide et al. (1996).

Eiken and Hinz (1993) divided the seismic section of the Vestnesa Ridge and the Yermak Plateou into three seismic sequences; YP-1, YP-2 and YP-3 (figure 2-3), which shows continuous strata with only minor unconformities. YP-1 is the lowermost sequence, showing a sub-parallel refection pattern and consists of syn- and post rift deposits. YP-2 sequence, consisting mainly of contourites, shows characteristic westward thickening wedges showing westward migration of the depocentre, and the sequence downlaps to the west. Characteristic patterns within the sequence with layers truncated at the seafloor are suggested as a result of contour currents systematically migrating upslope in response to changing bottom configuration caused by their own deposition. The uppermost YP-3 sequence has a depocentre with prograding pattern at the outer shelf and a second depocentre of elongated shape at the Vestnesa Ridge (figure 2-3). The sequence is on the upper slope dominated by glacial sediments in the Kongsfjorden TMF, the middle slope consists of contouritic, glaciomarine and hemipelagic sediments, while turbidites and hemipelagities probably dominate YP3 on the lower slope and abyssal plain.
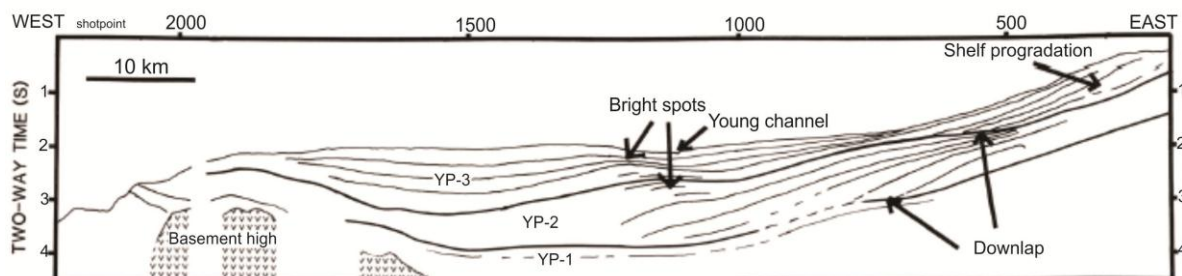
Figure 2-3: Interpretation of seismic line UB 18-81 across Vestnesa Ridge (modified from Eiken and Hinz, 1993).

Howe et al. (2008) carried out sediment core analysis from the Vestnesa Ridge. The analysis revealed that Holocene sedimentation is dominated by muddy-silty contourites with abundant IRD (ice-rafted debris). This was deposited under the persistent flow of the West-Spitsbergen Current. The LGM (last glacial maximum) was dominated by silty turbidites, resulting from increased sediment supply. The mid-Weichselian section displayed both turbidites and contourites with abundant IRD. Further, Howe et al. (2008) calculated sedimentation rates at the Vestnesa Ridge to be 105 cm/kyr during the Mid to Late Weichselian and a decrease to <10 cm/kyr during the interval between the LGM to the Early Holocene.

2.6 Gas hydrates, fluid flow and geothermal conditions

The gas hydrate province on the western continental slope of Svalbard is different than that from the Barents Sea and Mid Norwegian. The heat flow values are on average two to three times higher, suggesting a geothermal driven gas hydrate system (Bünz et al., 2008).

Gas hydrates have not been sampled from the western Svalbard margin, but the presence of a prominent BSR was revealed on seismic profiles in several seismic studies (Eiken and Hinz, 1993; Posewang and Mienert, 1999; Vanneste et al., 2005[b]), which indicates that gas hydrates and gas accumulations are common in the area. The BSR supposedly covers the whole of the Vestnesa Ridge, which represent one of the northernmost gas hydrate provinces that exist along Arctic continental margins (Petersen et al., 2008). The inferred gas- hydrate occurrence zone is situated nearby the mid ocean ridge which, makes a connection to the hydrothermal circulation system likely. Faults are identified on seismic profiles, stretching from the seafloor and through the BSR (Vanneste et al., 2005[a]). Thiede et al. (1998) proved a high content of organic carbon in the northern areas of the Fram Strait, and Premuzik et al. (1982) suggested values of organic carbon to 0,51 and 1,0 % for these areas. The gas hydrates on the western Svalbard margin are suggested to be mainly of biogenic origin (Myhre et al., 1995; Kvenvolden et al., 1998; Vanneste et al., 2005[a]).

Vogt et al., (1994) mapped out a 1-3 km wide and 50 km long belt of pockmarks on the crest of the Vestnesa Ridge and suggested that a hydrate layer is present under it. Pockmarks are assumed to be caused by the eruption of gas and seepage of gas and pore-fluids in soft fine-grained sediments (Hovland and Judd, 1988). Further, Vogt et al., (1994) hypothesized that methane is generated at depths below the Vestnesa Ridge, rising vertically and then migrates along the BGHZ until the methane finally accumulates below the crest of the natural anticline formed by the ridge (figure 2-4).

Posewang and Mienert (1999) identified a 100 m thick layer west of Svalbard with P-wave velocities ranging from 1800-1840 m/s. The velocities are approximately constant and indicate a homogenous distribution of gas hydrates within the sediments. The identification of a layer varying in thickness from 12-25 m with P-wave velocities down to 1380 m/s is interpreted to represent a free gas zone below the BGHZ.

Vanneste et al., (2005[b]) suggest that gas hydrates have accumulated in an area of ~1600 km^2 on the western Svalbard margin, in water depths ranging from about 750 to 2500 m. The BSR in the area can be traced from the upper continental slope and down to the oceanic ridge at 250 ms (TWT) bsf (below seafloor). It has high reflection amplitude, but varies laterally (Vanneste et al., 2005[a]). The short distance to the Knipovich Ridge, which acts a heat source, results in a sub-seafloor

temperature increase downslope. The sub-bottom depth of the BSR is therefore decreasing with increasing water depth (Posewang and Mienert, 1999).

According to Vanneste et al., (2005[b]), the sub-bottom depth of the hydrate stability limit varies laterally and is mainly controlled by the bottom-water temperature and the geothermal trend connected with lithospheric cooling in distance from the Molloy spreading Ridge.
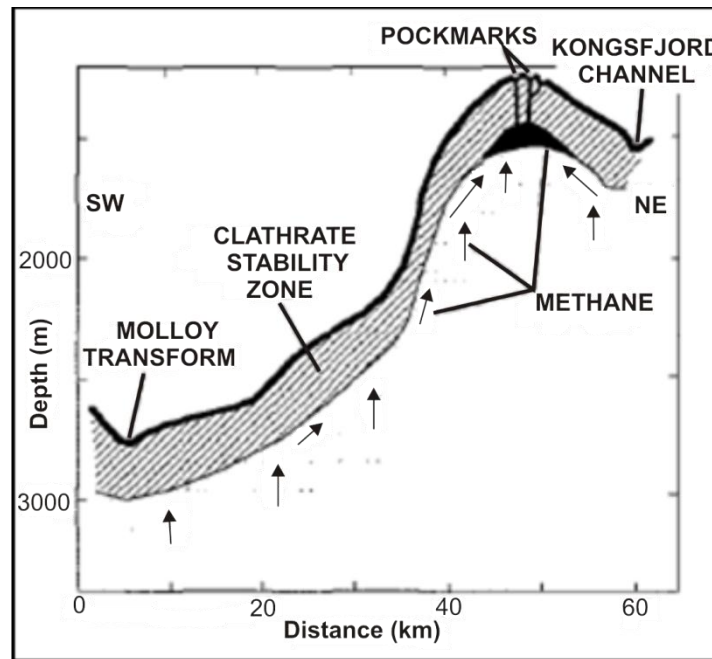
Figure 2-4: Profile through Vestnesa Ridge. Diagonal-ruled area indicates the hypothesized internal structure consisting of hydrate carapace. Methane is assumed to have been generated in the sediments below and migrated upwards. At the crest of the ridge the methane has been accumulated and intermittently venting along faults (modified from Vogt et al., 1994).

3. Data and methods

This thesis is based on the interpretation of 2D and 3D seismic data acquired on the western

Svalbard margin in the period 2001 – 2009 (figure 3-1).
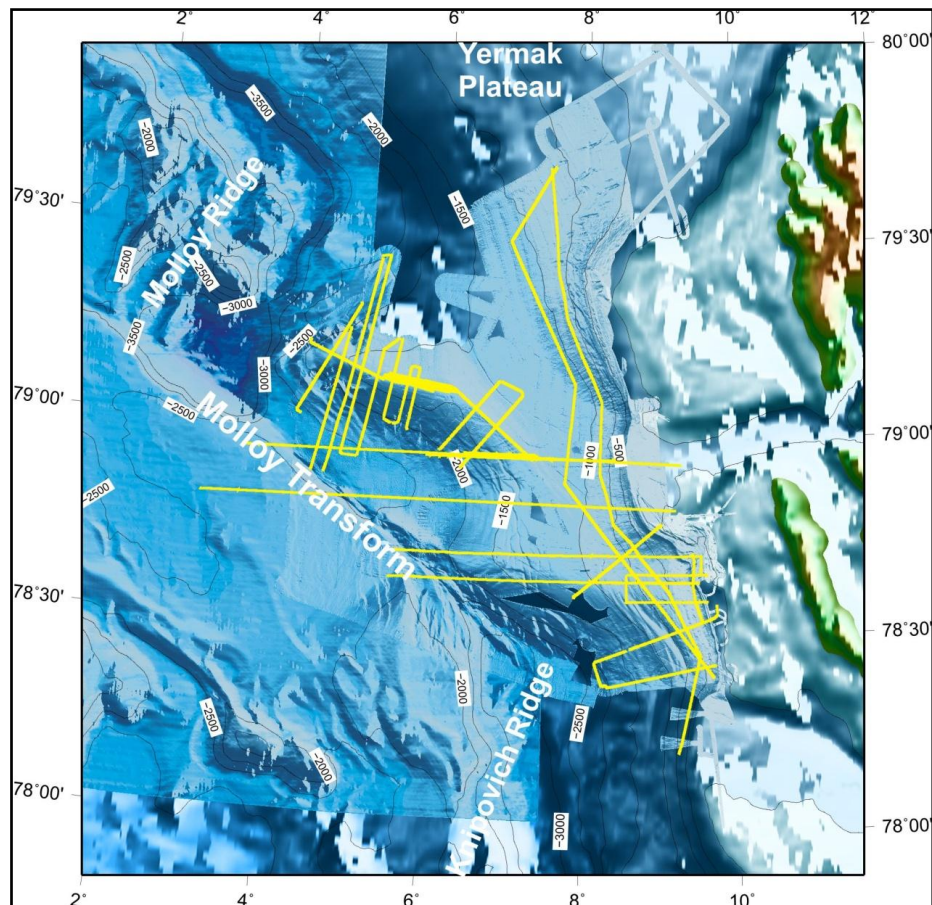
Figure 3-1: Bathymetric map of the study area with the Vestnesa Ridge located west of Svalbard and north of the North Atlantic mid-ocean ridge system. Seismic data are marked with yellow. (Modified from Bünz and Mienert, 2009)

3.1 Seismic resolution

Resolution is the ability to separate two features that are very close together; the minimum separation of two bodies before their identities are lost (Badley, 1985). Seismic resolution comprises two aspects – the vertical and horizontal resolution. Both are related to the minimum distance of two reflectors/layers that is needed in order to be realized on seismic data as two individual reflectors, or a measure of how large an object need to be in order to be seen on seismic data. The resolution of seismic data is measured in terms of the seismic wavelength, given by the quotient of velocity and frequency (figure 3-2). With increased depths, the rocks are older and more compacted, and thus the seismic velocity increases. Higher frequencies in the seismic signal are more quickly attenuated with depth leading to a decrease of the dominant frequency with increasing depth. This in turn results in an increase in wavelength with depth, making the resolution poorer (Brown, 1999).
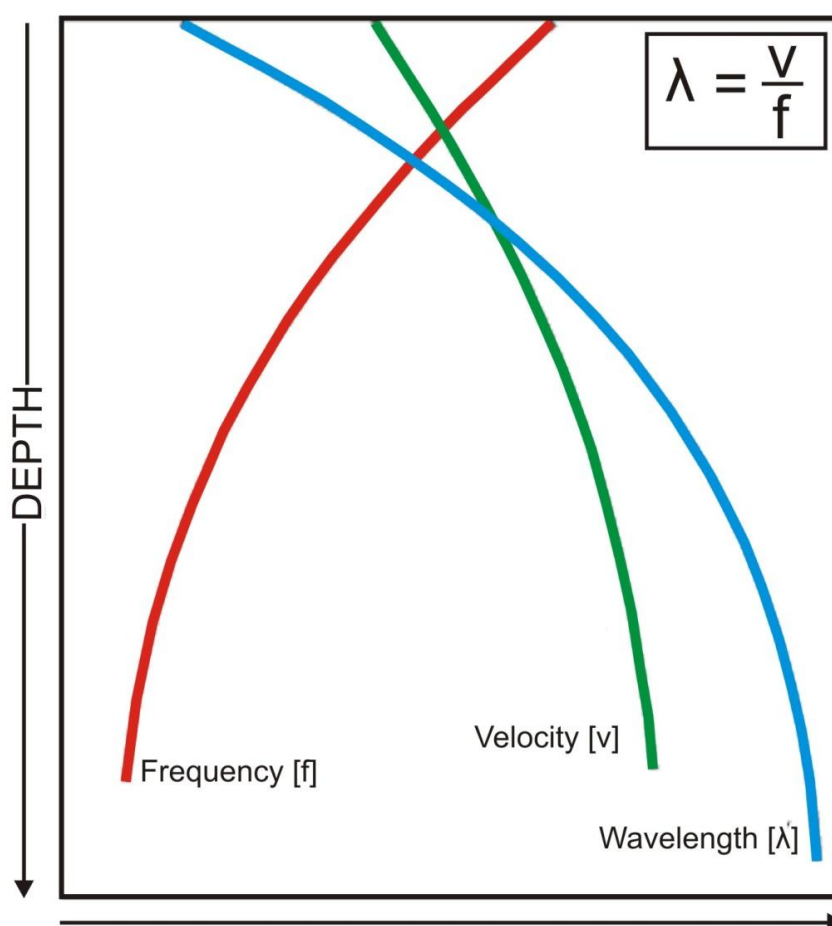
Figure 3-2: Relationship and variation of wavelength, frequency and velocity with increasing depth. Wavelength increases significantly with depth, making the resolution poorer (modified from Brown, 1999).

3.1.1 Vertical resolution

The vertical resolution refers to the ability to distinguish two close seismic events corresponding to different depth levels (e.g. identify the top and the base of a thinning sedimentary bed). Vertical resolution is commonly given as $^1/_4$ of the wavelength . To obtain a good resolution, it is desirable to achieve a small wavelength. This means a reduction in the relationship between the seismic velocity and the frequency. Lithologies with low velocities would therefore get a better resolution than high velocity lithologies.

3.1.2 Horizontal resolution

The horizontal resolution is concerned with the ability to distinguish and recognize two laterally displaced features as two distinct events. Horizontal resolution of unmigrated seismic data is determined by the Fresnel zone (Badley, 1985; Brown, 1999) (figure 3-3). This implies that if two elements fall within the Fresnel zone, they will not be separable and will not be seen on the seismic data. The horizontal resolution is getting poorer with an increase in depth and velocity and a decrease in frequency (Badley, 1985). Migration of seismic data is the most important technique for improving the horizontal resolution. This process repositions misplaced reflections due to dip, focuses energy spread over a Fresnel zone, and collapses diffraction patterns from points and edges. When performing migration, the Fresnel zone is reduced to an ellipse perpendicular to the line using 2D migration, and a small circle for 3D migration (Brown, 1999). The theoretical result of 2D- and 3D migration is shown in figure 3-3.

Figure 3-3: Effect on Fresnel zone size and shape after 2D and 3D migration (modified from Brown, 1999).

3.2 2D seismic data

Both single- and multi-channel 2D seismic surveys have been used. This data has been acquired on several academic cruises with R/V Håkon Mosby an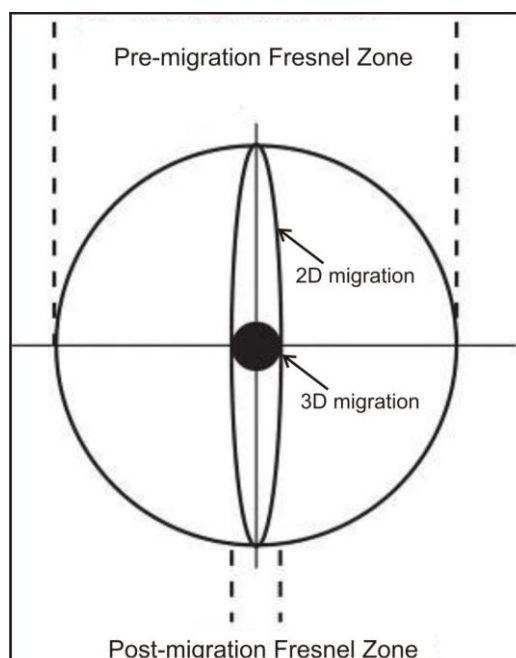d R/V Jan Mayen conducted by the University of Tromsø and the University of Bergen. Table 2 provides an overview of the individual surveys and their basic survey parameters.

Year	Vessel	Parameters
2001	R/V Jan Mayen, UiTø	single-channel seismic using a sleeve-gun array of 80 in^3 , towed at 4 m water depth and shot at 10 sec interval providing a trace spacing of ca. 22 m
2001	R/V Håkon Mosby, UiB	Multi-channel seismic using a 3000 m long, 240-channel streamer towed at 7 m water depth, and a bolt gun array of 776 in^3 with a shooting distance of 75 m providing a CMP spacing of 6.25 m
2006	R/V Jan Mayen, UiTø	single-channel seismic using a GI-gun array of 240 in^3 , towed at 4 m water depth and shot at 10 sec interval providing a trace spacing of ca. 22 m
2007	R/V Jan Mayen, UiTø	single-channel seismic using a GI-gun array of 240 in^3 , towed at 4 m water depth and shot at 10 sec interval providing a trace spacing of ca. 22 m
2009	R/V Jan Mayen, UiTø	single-channel seismic using one single GI-gun of 140 in^3 , towed at 4 m water depth and shot at 7 sec interval providing a trace spacing of ca. 15 m

Table 2: Overview of the individual 2D seismic surveys and their basic parameters.

The processing of the multichannel seismic data followed standard work flows including bandpass filtering, deconvolution, amplitude correction, stacking and Stolt F-K migration. The data has a dominant frequency of about 50 Hz providing a theoretical resolution of up to 8 m assuming a velocity of 1600 m/s. Though the data has been migrated, 2D seismic data generally suffer from out-of-plane reflection acrosstrack. Hence, the Fresnel zone at the seafloor in 1500 m water depth would be approximately 300 m.

The processing of the single-channel seismic data included spherical divergence correction, spiking, deconvolution, bandpass filtering (Ormsby, 30-300 Hz) and F-K Stolt migration. The data for both the sleeve gun and the GI-gun array has a dominant frequency of 80-100 Hz with usable frequency contents of up to 250 Hz. This results in a theoretical resolution of about 4 m and a Freznel zone radius of about 210 m assuming a water depth of 1500 m.

3.3 3D seismic data

The 3D seismic data were acquired in July 2007 using the P-cable 3D seismic system of the University of Tromsø. The system consists of up to 24 streamers towed parallel and separated by a lateral offset of about 10 meters. The array of single-channel streamers acquire 24 seismic lines simultaneously, thus covering an approximately 240 m wide swath with close inline spacing. Streamers with hydrophones are 25 m long and contain 8 channels each. They are attached to a cross cable towed perpendicular to the vessel's steaming direction using two large trawl doors (figure 3-4). In total, an area of 23 km^2 was surveyed with 32 profiles using 8 or 12 parallel streamers. Two GI guns with a total volume of 240 cubic inch provided seismic energy with frequencies from 20-200 Hz. Streamer position calculations assumed a modified triangular cross cable geometry, and for relocations direct wave arrivals were used (Petersen et al., 2008).
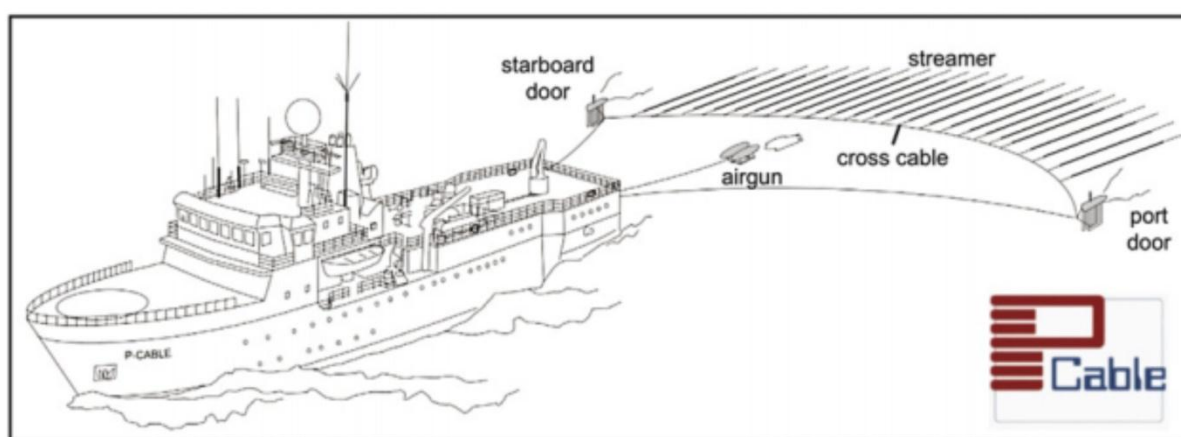
Figure 3-4: Schematic diagram of P-cable 3D seismic system (from Petersen et al., 2010).

3.4 Bathymetry data

Bathymetry data from the western Svalbard margin has been used to correlate 2D seismic data with seafloor features. Swath bathymetric data acquired during cruises in 2006 and 2007 with R/V Jan Mayen have a bin-size of 50 m. The raw data originated from the Simrad EM300 acquisition system that operates with 135 beams and sonar frequencies of 30 kHz (Hustoft et al., 2009).

3.5 Petrel as interpretation tool

The seismic interpretations and visualizations carried out in this thesis were performed using Petrel 2010 software from Schlumberger. Petrel provides different tools for generating horizon maps from which geological information can be determined. Petrel uses negative sign in front of depths (e.g. -500 ms TWT), but are referred to as positive in the text. Green arrow is used on figures indicating orientation towards north.

3.5.1 Interpretation of 2D- and 3D seismic data

There are three basic methods for horizon interpretation suitable for 2D lines in Petrel. 1) Manual interpretation, which perform a linear interpolation between the picked points along a horizon. 2) Guided autotracking where the best route along a reflection between two picked points along a horizon is chosen automatically. 3) Seeded 2D autotracking where points will be tracked along a reflection until it comes to a discontinuity and does not fulfill the constraints specified in the autotracking parameters. For 3D seismic data a fourth method can be used in addition; seeded 3D autotracking, where points will be tracked outwards from a picked point in all directions to get a 3D view of a distinct reflection. For the purpose of interpreting the seafloor horizon on the 2D seismic data, the seeded 2D autotracking and guided autotracking was appropriate. Seeded 3D autotracking was used on the seafloor on the 3D seismic data. For the interpretation of the BSR, guided autotracking and manual interpretation was used both on the 2D and 3D seismic data.

It must be decided on which type of reflection the interpretation will be done. This is done manually where it can be chosen from peak, trough, upper zero crossing or lower zero crossing (figure 3-5). Peak or trough with the best continuity was chosen for horizon interpretation in this thesis.
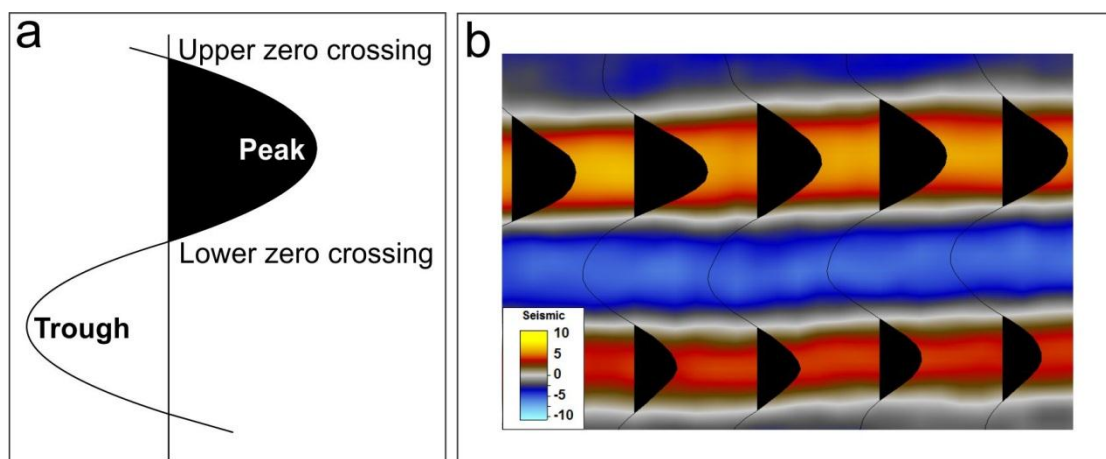

Figure 3-5: A: Definition of the seismic signal where peak, trough, upper- and lower zero crossings are indicated. B: Seismic traces overlaid on the seismic depiction. The seismic color table show how the amplitudes are viewed in the seismic data. The values are a measure of the excursion of the acoustic impedance contrast.

3.5.2 Functions, tools and seismic attributes in Petrel

Petrel offers different tools for visualization of seismic data. Surfaces can be generated and displayed in 2D or 3D view using different color-scales and appropriate light sources in order to highlight different features. Surface generation based on 2D lines can, however, prove to be difficult, especially in cases where the line spacing is large.

Seismic attributes can be applied on seismic sections, time-slices, random intersections, surfaces and as volume renders.

Thickness map calculates the thickness between a given surface and another using the dip and azimuth of the surfaces. The thickness map is displayed in TWT between two surfaces with depth in TWT that are interpreted from the seismic data.

Envelope is the total instantaneous energy of the analytic signal, independent of phase. Envelope is also known as 'Instantaneous Amplitude', 'Magnitude' or 'Reflection Strength'. The envelope attribute is useful in detecting bright spots caused by gas accumulations, detecting major lithological changes that are caused by strong energy reflections and sequence boundaries. The attribute clearly shows subtle lithological changes that may not be apparent on the seismic data.

Instantaneous frequency is the time derivative of phase. It is often used to estimate seismic attenuation, as hydrocarbon reservoirs usually cause drop-off of high frequency components.

RMS Amplitude is the square root of the sum of the squared amplitudes, divided by the number of samples. RMS can map directly to hydrocarbon indications in the data and other geologic features by amplitude response. It is an important attribute for characterizing different sedimentary environments.

Variance (Edge method) estimates the local variance in the signal. This analysis can discriminate between low and high continuity of seismic reflections and is a useful tool to investigate discontinuities in seismic reflectors related to terminations (stratigraphic) or structures (faults). The variance attribute can be used in fault detection from continuous variance response and for gas chimney mapping.

3.6 Gas hydrate stability modeling with CSMHYD

The CSMHYD software from Sloan (1998[b]) was used in the modeling of gas-hydrate stability in the study area (figure 3-6). The program calculates pressure/temperature conditions for the phase transition between free gas and gas hydrates. It is also possible to vary the hydrate composition in such the stability zone of different hydrate structures are differentiated. Different hydrate structures are expected to cause a change in the GHSZ thickness, where an increase in higher order hydrocarbons (e.g. ethane and propane) will increase the thickness (Sloan, 1990). In addition to calculations of the stability temperature at a given pressure (or vice-versa) in pure water, the program also includes a variable salt component to allow seawater and pore-water predictions.

Figure 3-6: Section from the CSMHYD software by Sloan (1998b). The program calculates the temperature or the pressure at the phase transition. Further, composition of free gas-phase and solid hydrate-phase is calculated (marked as phase composition). Hydrate composition describes the composition of gas molecules in small and large hydrate structures.

4. Results

The seismic observations and interpretations presented in this chapter is a result of the identification and mapping of a BSR on the 2D- and 3D seismic data. The BSR provides indirect evidence for the occurrence of gas hydrates in the study area. In the 3D seismic dataset, horizon mapping is also integrated with seismic attribute maps and cubes, suggesting areas with fluid migration. Focus is gained on how these structures affect the BSR. Figure 4-1 shows an outcrop of the area including the 2D seismic surveys and the 3D seismic cube used in this study. Figure 4-2 shows a 3D view of the 3D seismic cube. The outcrop in figure 4-1 is used as a location reference map for figures presented in this thesis.

The appearance and characteristics of the BSR shows great variation within different parts of the study area. In the following, a description of the different areas will be presented, including the area of the Vestnesa Ridge, the Molloy Transform and the continental slope (figure 2-1). The 3D seismic data is used for a detailed study on how fluid flow and related structures affect the BSR at the Vestnesa Ridge crest.
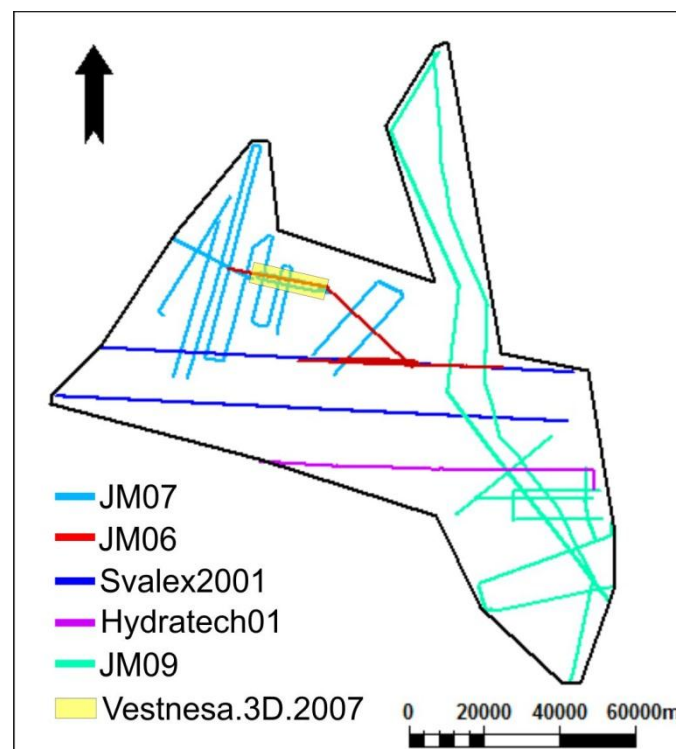
Figure 4-1: Overview of the orientation of the seismic data.
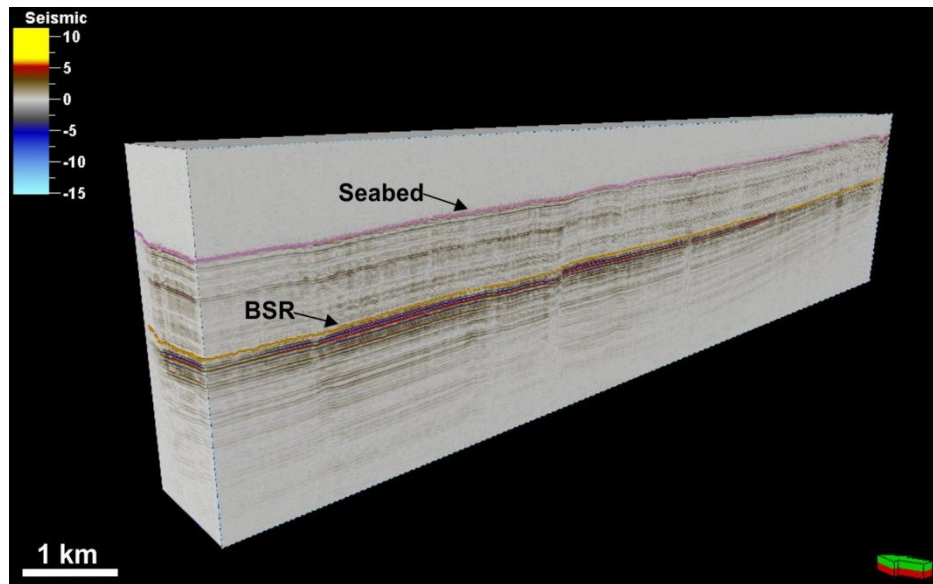
Figure 4-2: 3D image of the Vestnesa.3D.2007 survey with the interpreted seabed and BSR horizons.

4.1 BSR in the Vestnesa Ridge area

4.1.1 Vestnesa Ridge crest

The crest axis is stretching out for ~100 km in SE-NW to EW direction in water depths between ~1200-1500 m. The Vestnesa Ridge is gently dipping from SE to the point where it turns westward with an average slope angle of ~0,1°. From this point the slope angle gradually increases to ~1° until a rapid increase to ~6° at the most western part of the Vestnesa Ridge, towards the Molloy Deep. The average slope angle of the southern flank is increasing from the SE area (2,5°) to the western part of the ridge flank (3,5°). The northern flank slope is dipping more gently with a gradually increasing slope angel of ~0,9° in the SE part to ~1,5° in the western part.

The most striking features at the crest are several depressions at the seafloor interpreted as pockmarks (figure 4-3 a and b). These are observed both on 2D and 3D seismic data, but are however best visualized on the 3D data. The pockmarks have circular to oval shape, diameter of up to 500 m and depth of ~10 m. Pockmarks are typical seabed expressions of focused fluid flow (Judd and Hovland, 2007), and may indicate recent fluid flow activity at the crest. The pockmarks are distributed along the whole crest but the density is generally decreasing from east to west.
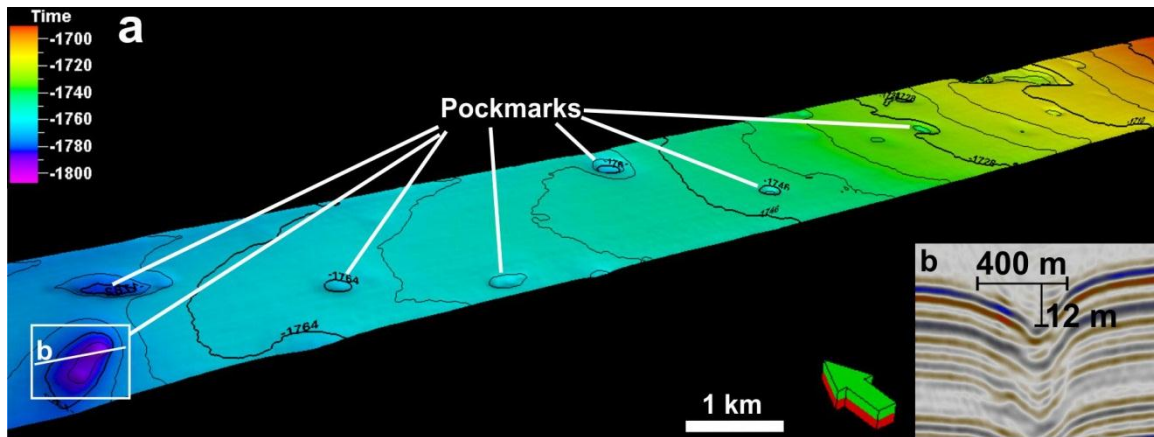
Figure 4-3: a) Visualization of the seafloor showing depressions interpreted as pockmarks. b) Seismic inline showing a pockmark with a diameter of ~400 m and a depth of ~12 m.

The seismic lines going parallel to the axis of the Vestnesa Ridge show a pronounced polarity reversed reflection running parallel to the seafloor reflection, and crosscuts stratigraphic boundaries at ~180-240 ms (TWT) bsf (figure 4-4). The reflection is interpreted to represent a gas-hydrate related BSR as these characteristics are typical for such seismic phenomenon (Vanneste et al., 2005[b]). The 3D seismic data is located at the crest in NW-SE direction. Here, the BSR is identified laterally throughout the dataset and can be illustrated as a time-structure map (figure 4-5), showing a depth increase towards NW. The BSR at the crest is showing high amplitude values, high reflection strength and reversed polarity relative to the seafloor reflection (figure 4-4). Enhanced reflections showing high amplitude values are observed beneath the BSR and are indicative of the presence of free gas. Below the enhanced reflections, large seismic turbidity zones or acoustic masking is observed (figure 4-4).
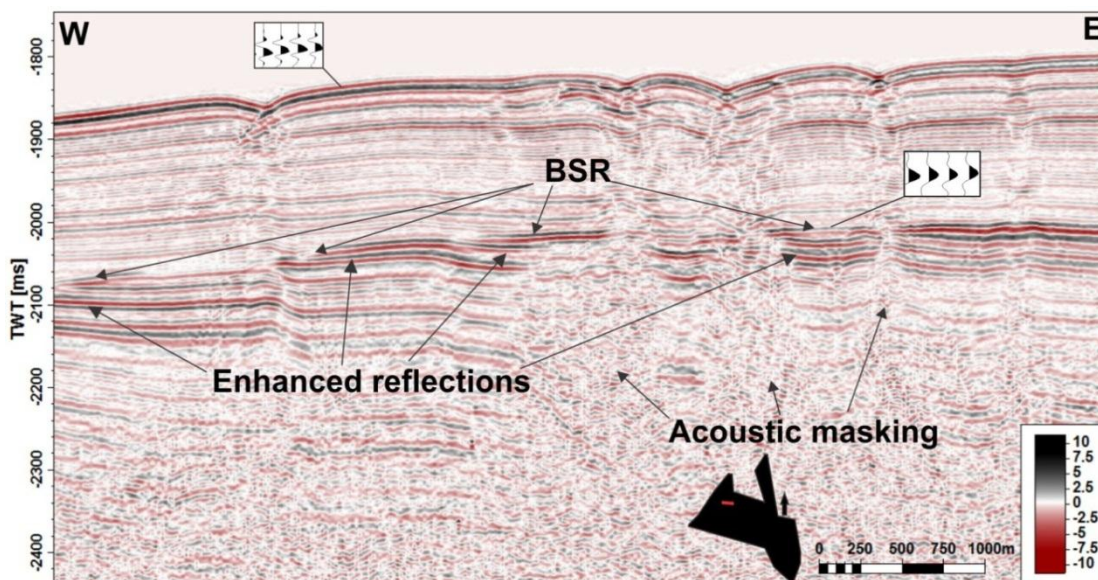
Figure 4-4: Seismic section along the crest of the western part of the Vestnesa Ridge showing a BSR with reversed polarity compared to the seafloor reflection. Beneath the BSR a zone of enhanced reflections and zones of acoustic masking is observed.
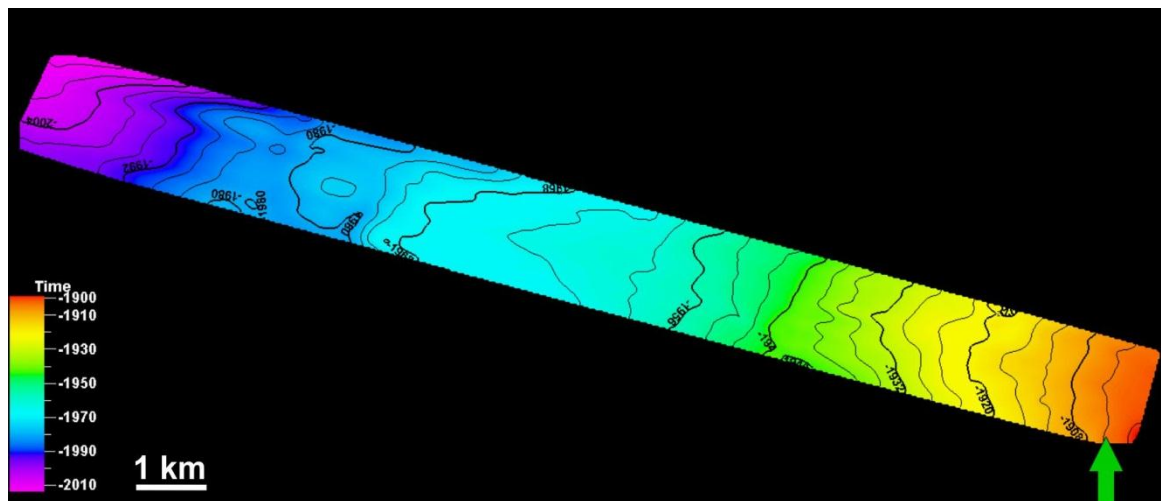
Figure 4-5: Time-structure map of the interpreted BSR showing a depth increase towards the northwest.

As well as the BSR observation, the investigation of changes in the instantaneous frequency content of the 3D seismic data allows the inferring of the presence of gas hydrates in the sediments (Satyavani et al., 2008). Within the GHSZ, above the BSR, elevated frequency contents are manifested from the instantaneous frequency attribute (figure 4-6 and 4-9c), where the dominant instantaneous frequency shifts from ~130 Hz above the BSR to ~50 Hz below the BSR. A 40-90 ms (TWT) thick layer above the BSR shows higher frequencies. Below the BSR, the frequency is lower, indicating higher attenuation. Low frequency shadows are commonly associated with the free gas that occurs below highly reflective layers indicating a strong velocity contrast (Taylor et al., 2000).
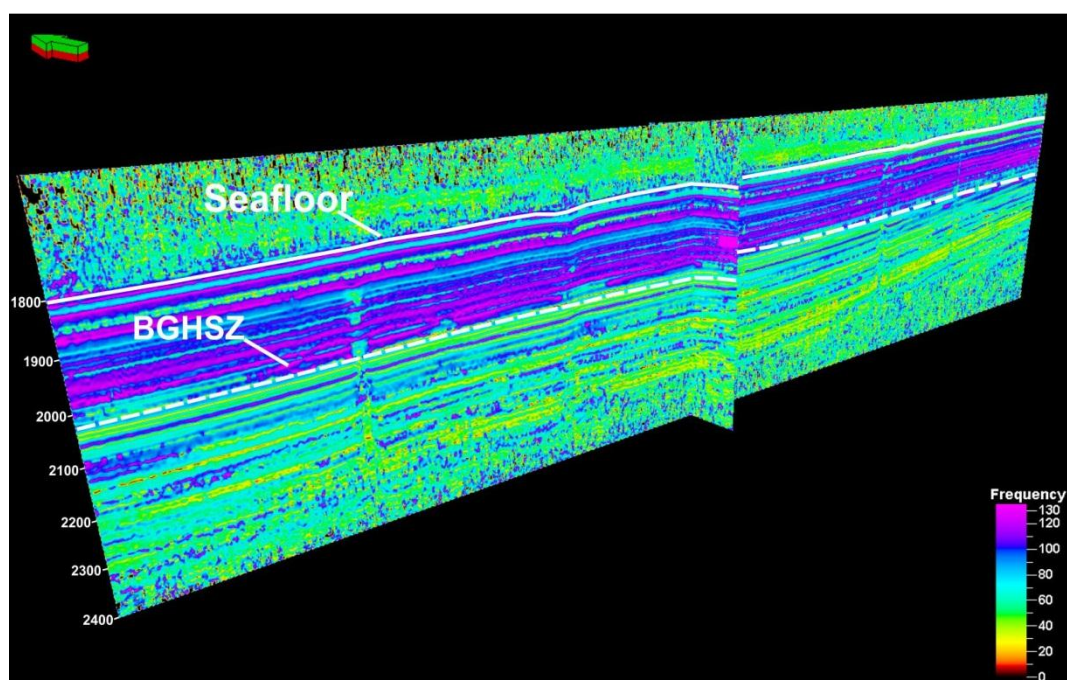
Figure 4-6: Inline and crossline from instantaneous frequency attribute cube. Higher frequencies above the BGHSZ indicate a lower attenuation than below, where the frequencies are lower.

The sub-bottom depth of the BSR at the crest generally decreases from SE to NW towards the mid-oceanic ridge system. A time-thickness map generated between the seafloor and the BSR surface illustrates this (figure 4-7).
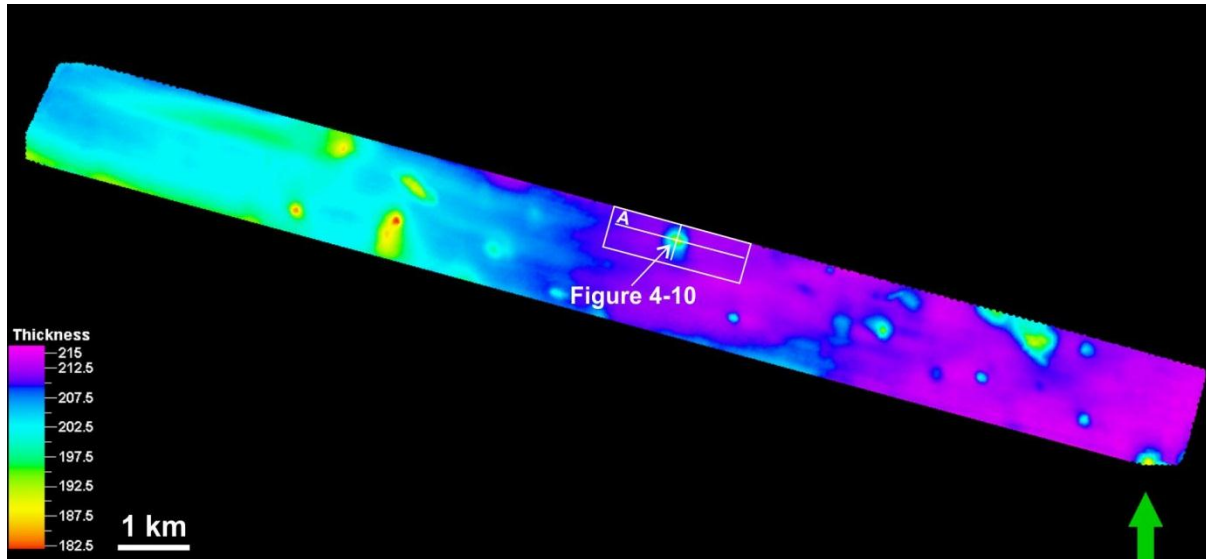
Figure 4-7: Time-thickness map generated between the seafloor and the BSR surface. Seismic section A is shown in figure 4-11.

The BSR can be observed along the whole of the ridge crest, but at several places it is significantly disrupted and cut of what appears to be fluid-flow related structures (figure 4-8 and 4-9). The structures are on seismic sections identified as near-vertical zones characterized by seismic wipe-outs, localized up-bending and amplitude decrease of reflections, and can be termed as acoustic pipes or chimneys (Løseth et al., 2011). The size and shape of the structures show a great range of variation along the crest. Also variation is observed within the unique chimney. In some of the pipes/chimneys, amplitude anomalies with irregular distribution are observed between the BSR and the seafloor (figure 4-10). Fluid-flow related structures seem to be confined to the ridge crest in particular.
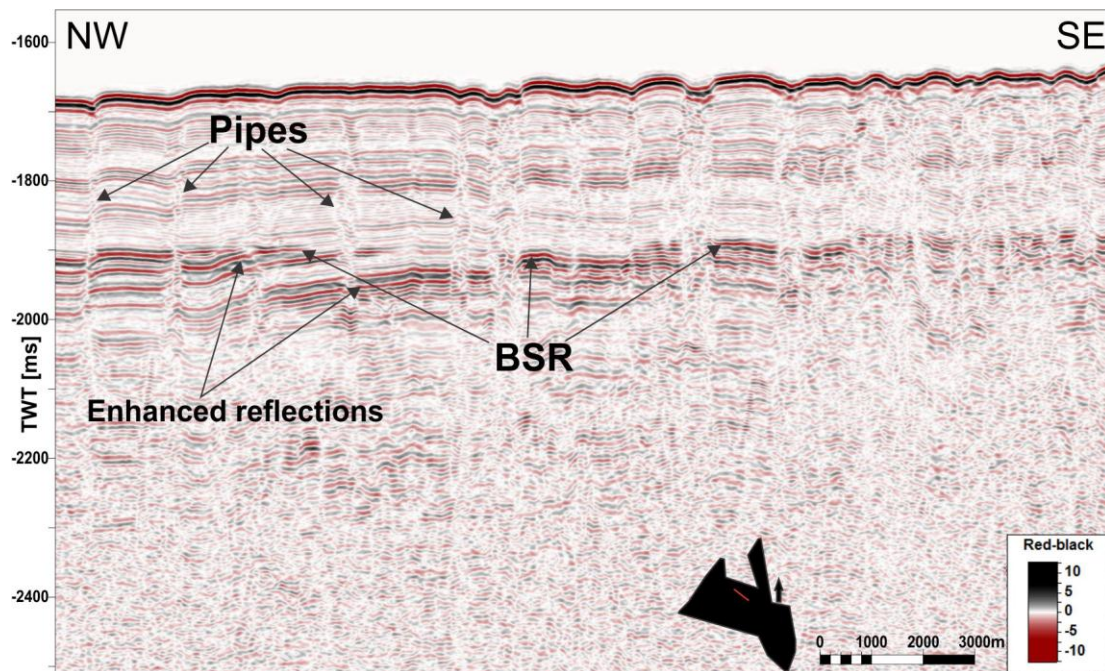
Figure 4-8: Seismic section along Vestnesa Ridge crest, showing the BSR with underlying enhanced reflections and the disruption of it by pipe structures.

The structures reach from the BSR or from even greater depths to shallower levels where they commonly terminate in seafloor pockmarks. In the western and northwestern part of the ridge crest, and down from the ridge towards the Molloy Deep, the seafloor is dipping; here the BSR can be identified as envelope of the termination of high-amplitude reflections that strongly crosscuts stratigraphic boundaries at ~190-200 ms (TWT) bsf (figure 4-9). In few places the BSR shows a proper reflection in its own right. Here it is characterized by reversed polarity relative to the seafloor reflection, thereby mimicking the seafloor. Figure 4-9 shows four displays of a seismic profile from this area where vertical zones of disrupted reflections pierce through sedimentary strata, perturbing the BSR and can be followed upwards where the connections to seafloor depressions are clearly seen. In the SE part of the profile, the structures are aligned so closely, that they are difficult to separate from each other. The reflection strength attribute (figure 4-9 b) enhances the strong reflections terminated by the BSR. A variance volume attribute (figure 4-9 d) shows that the vertical zones of disrupted reflections show a significant larger degree of variance than the surrounding reflections.
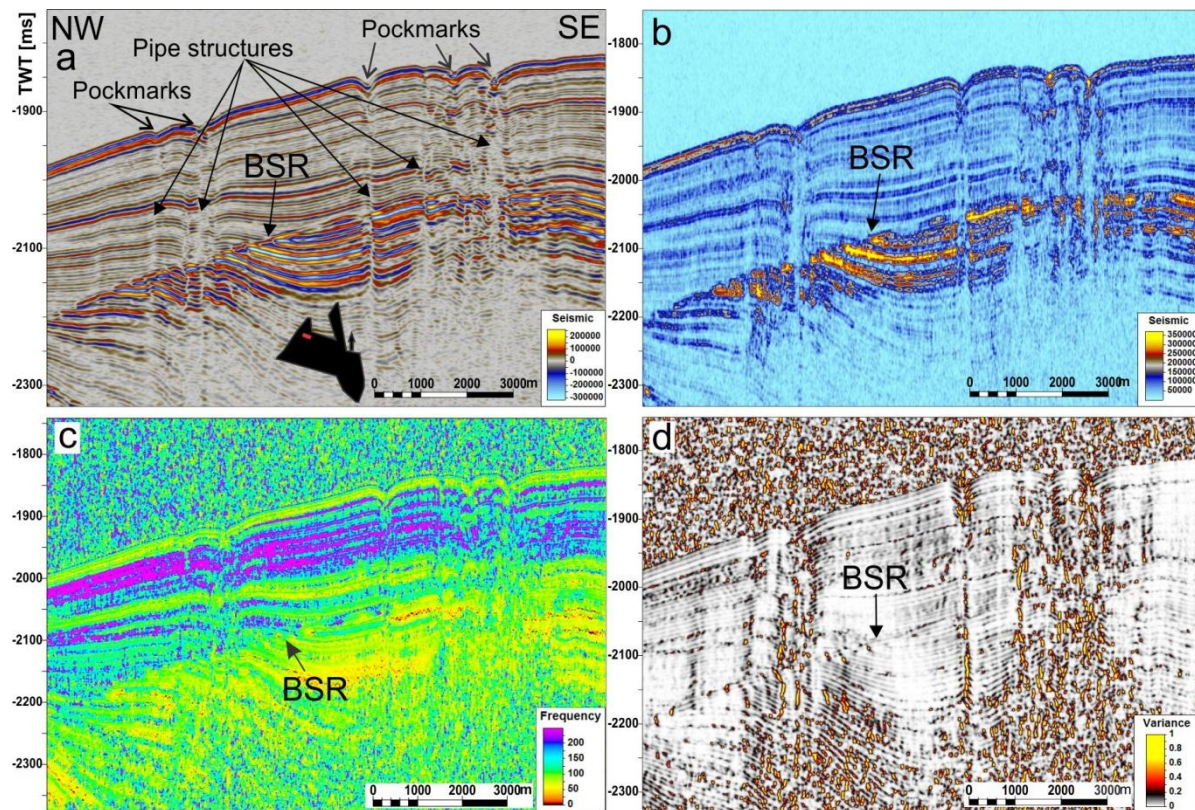
Figure 4-9:a) Seismic section from the western part of the Vestnesa Ridge crest showing pipe structures that pierce through the sedimentary strata and cuts the BSR. The pipe structures terminate seafloor depressions interpreted as pockmarks. b) Reflection strength attribute show the enhanced reflections terminated by the BSR. c) Instantaneous frequency attribute showing the low frequency content below the BSR indicating high attenuation and the presence of free gas in the pore space. d) Variance attribute showing areas of high variance below the BSR and concentrated in the pipe structures above the BSR.

The time-thickness map show circular to oval areas with a significant decrease in thickness compared to the surrounding area (figure 4-7). These areas coincide with the localization of the acoustic chimneys/pipes and the seafloor pockmarks. Figure 4-10 shows a perspective view of a selected inline and crossline that intersects in a seafloor pockmark (see figure 4-7 for location). A positive amplitude anomaly is observed within the chimney at ~100 ms (TWT) bsf (figure 4-10, and 4-11). Within the chimney it is observed that the BSR is shifted to earlier times in a circle area of 200 m in diameter, which could represent a velocity pull-up feature. Beneath the BSR, a moderate push-down effect is observed, which might be related to the presence of free gas.

Figure 4-11 shows an inline going through the chimney (A) and time-slices from an RMS amplitude cube taken at different stratigraphic levels showing lateral amplitude variations of the chimney. The seafloor show rather homogeneously distributed amplitudes with exception of the seafloor pockmark which show decreased amplitudes at its rim. Time-slice 1 images the amplitude anomaly observed within the chimney where the highest amplitudes are observed in the centre. Time-slice 2 encloses the BGHSZ. At this level, the BSR is starting to deflect upwards, observed as a pull-up feature on the seismic section (figure 4-10). The centre of the chimney shows low amplitudes. Time-

slice 3 image the area just below the BGHSZ where the supposedly free gas zone is located. Here, the chimney showing low amplitudes seem to deflect high-amplitude strata reflections. Time-slice 4 shows that the area of low amplitudes within the chimney is decreasing. This trend is continuing with depth as amplitude variations across the chimney cannot be traced longer than ~2100 ms (TWT).
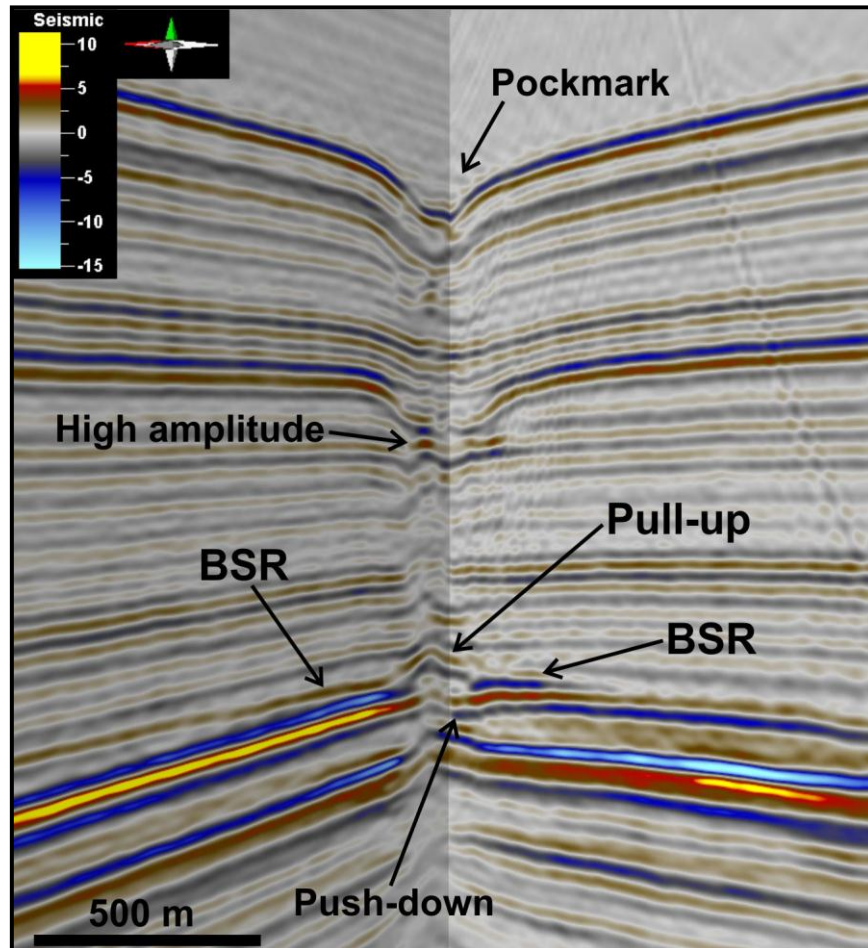
Figure 4-10: 3D view of chimney structure terminating a seafloor pockmark (see figure 4-7 for location). A high amplitude anomaly is identified within the chimney structure at ~100 ms (TWT). The BSR is observed as a pulled up feature within the chimney, whereas a moderate push-down feature is observed beneath the BSR.
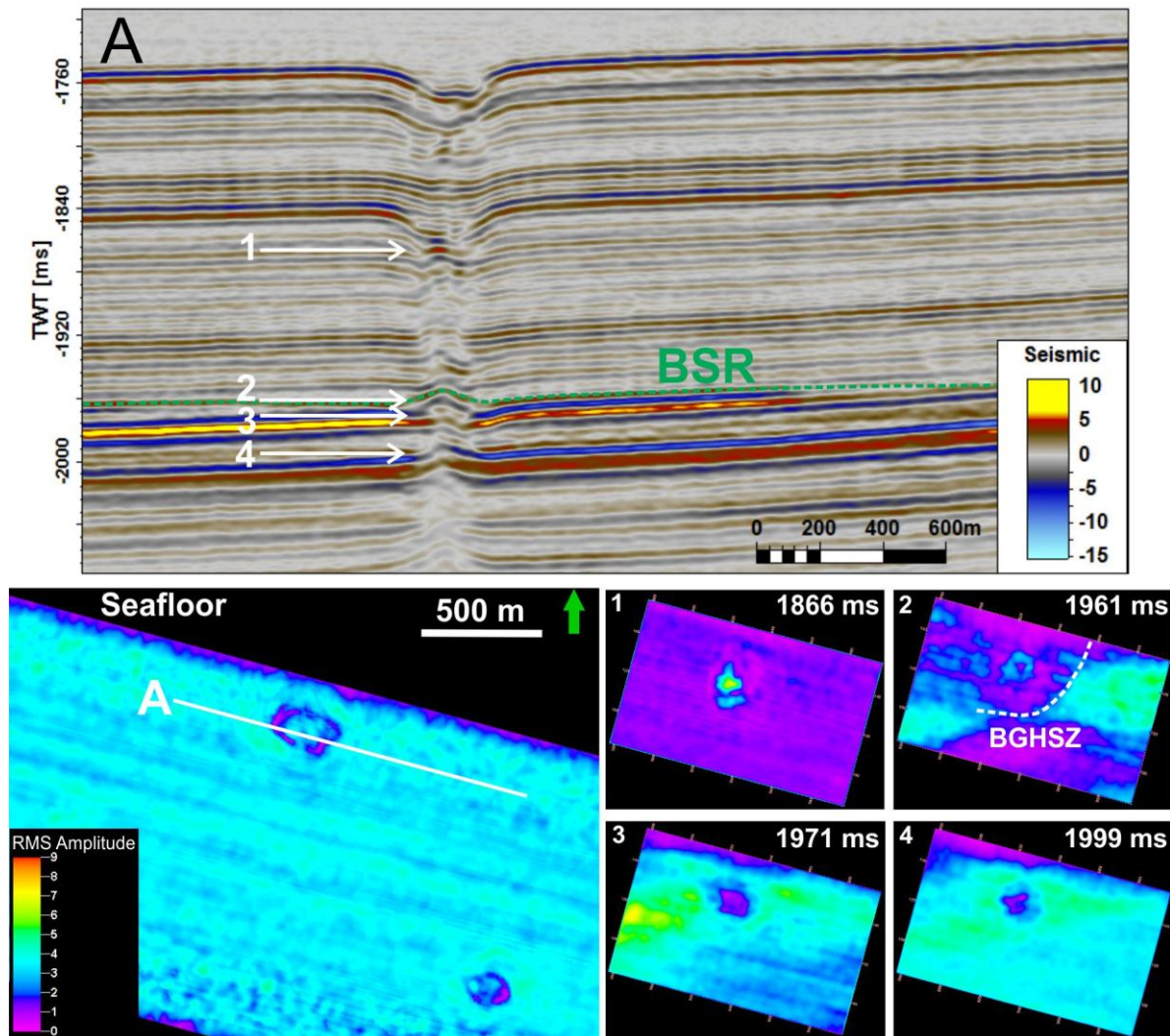
Figure 4-11: A: Seismic section showing an acoustic chimney structure (also shown in figure 4-10). The BSR is going through the chimney, but loses its seafloor mimicking characteristics as it bends upwards. RMS time-slices generated from five stratigraphic levels (marked with white arrows) including the seafloor are shown below the seismic section A. The seafloor show homogeneously distributes amplitudes with exception of the seafloor pockmark showing decreased amplitudes at its rim. 1) Images the amplitude anomaly observed within the chimney structure with the highest amplitude observed in the center. 2) This level encloses the BGHSZ (white dashed line). 3) Images the area just below the BSR where the supposedly free gas zone is located. The chimney is showing low amplitudes and seems to deflect high-amplitude strata reflections. 4) The area of low amplitudes within the chimney is decreasing at this level.

In the NW part of the 3D seismic data, four large seafloor pockmarks are observed (figure 4-12 a). A random seismic line was created across these, revealing acoustic chimneys, all terminating in the pockmarks (figure 4-12b). Within the chimneys, the seismic reflectors are disturbed and especially chimney 2, 3 and 4 show vertical displacement of reflectors relative to each other. These vertical displacements are interpreted to represent faults or fractures. A variance cube was generated from which seismic time-slices from ten different stratigraphic levels were investigated (figure 4-13). The time-slices visualize the lateral extent of the chimneys. The areas of high variance indicates disturbance of the sediments due to active or former gas movement. Near the seafloor, at 1800 ms (TWT), the shape of the chimney structures can be suggested according to the areas of high variance

(figure 4-13). The two westernmost chimneys (1 and 4) show a near-circular shape, while the two easternmost chimneys (2 and 3) show a more elongated oval shape. At 1900 ms (TWT), chimney 3 and 4 loses their characteristic rounded shape and adapt to narrow zones of high variance oriented in SE-NW and SW-NE direction respectively (figure 4-13). This transition may represent a connection between the chimneys and the fault/fractures. The fault/fracture connected to chimney 3 is approximately 650 m oriented in SE-NW direction, while the fault/fracture related to chimney 4 increase in length down to 2000 ms (TWT), assuming a crescent shape oriented in SW-NE direction with a length of approximately 1,5 km. At chimney 3, however, the seismic section reveals vertical displacement of the reflectors as shallow as 1825 ms (TWT) (figure 4-12b). Also, chimney 2 seems to be connected to fault/fractures that are clearly seen at 2000 ms (TWT). The fault connected to chimney 2 is approximately 700 m oriented in SW-NE direction. The time-slice at 2000 ms (TWT) is cutting through the high reflective strata just beneath the BSR (figure 4-12b). Here, the areas of high variance are confined to narrow zones interpreted as faults in connection to chimney 2, 3 and 4. Chimney 1 still maintains its circular shape at this level. Down to 2100 ms (TWT) the zones of high variance are confined to the faults/fractures, observed as narrow lines on the time-slices. From this level and down to 2250 ms (TWT) the area of high variance is increasing gradually, concentrated around the faults/fractures that are still recognizable at 2250 ms (TWT).
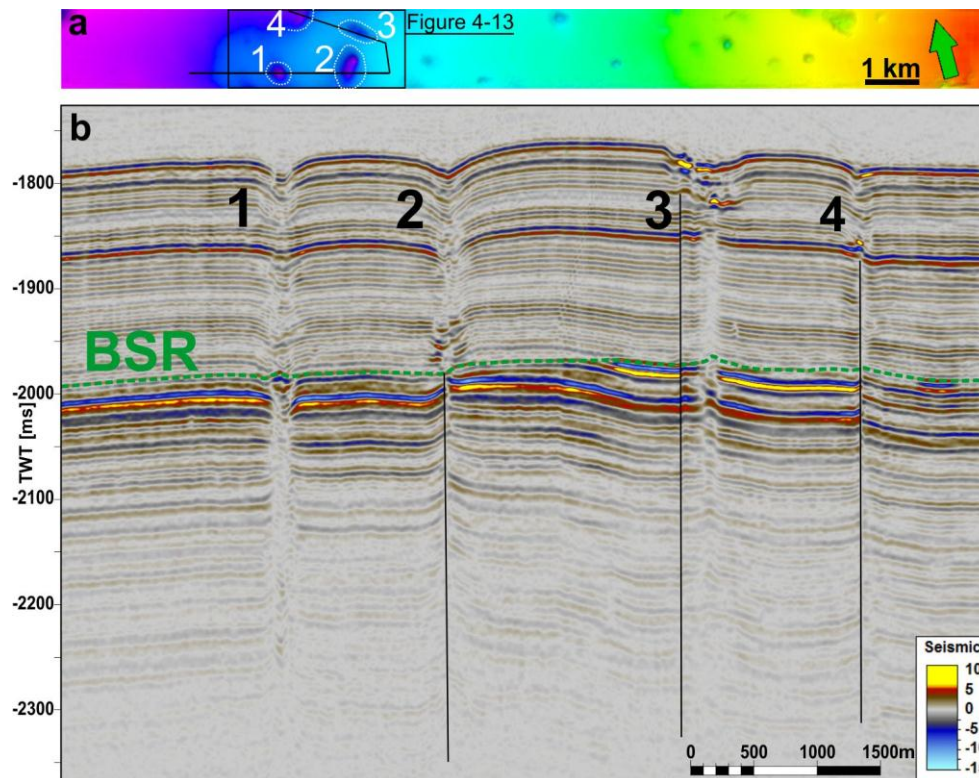
Figure 4-12: a) Seafloor pockmarks (numbered 1-4) observed in the NW part of the 3D seismic data. b) Random seismic line generated through the four pockmarks (indicated as a black line in a). The seismic section reveals chimneys that terminate the seafloor pockmarks (same numbering as for the pockmarks in a). The BSR is crossing all the chimney structures and faults are observed at or close to them.
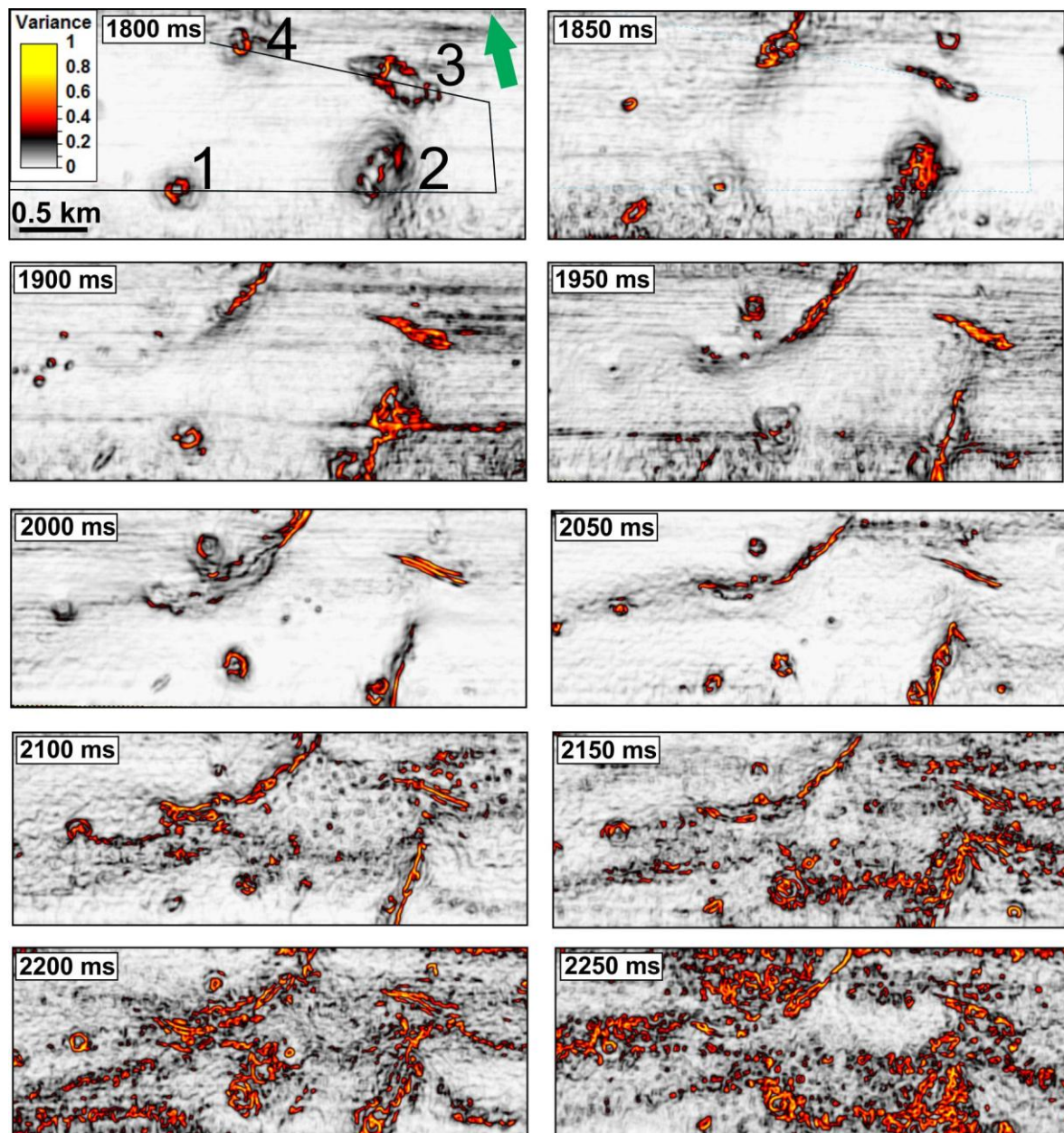
Figure 4-13: Time-slices from a variance attribute cube at different stratigraphic levels. The time is given in TWT. The pockmarks are numbered 1-4 and can be observed as near-circular to elongated areas of high variance. The development of the structures can be followed with depth where they seem to be connected to faults or fractures.

4.1.2 Vestnesa Ridge flanks

In contradiction to the BSR observations at the crest, where fluid flow structures dominate, the crest flanks show well stratified reflections with no signs of seafloor pockmarks (figure 4-14 and 4-15).

On the N-S oriented seismic lines running transverse to the Vestnesa Ridge, the BSR is observed in well-stratified sediments at ~200-250 ms (TWT) bsf in water depths varying between 1300-2500 m. On the western side of the southern ridge flank topographic elevated areas are observed (figure 4-14). These appear as local drifts on the flanks, probably related to the contouritic depositional environment. The reflections are showing a parallel trend until they are cut by the BSR which can be

traced for ~10 km. The BSR fades out towards south as the reflections show an increasingly degree of parallel layering with the seafloor reflection (figure 4-14). Beneath the drifts, the BSR terminates enhanced reflections. Between the drifts, however, the BSR can be identified as a continuous event on the westernmost lines across the ridge. The enhanced reflections beneath the BSR, showing high amplitude values, seem to be focused just beneath the drifts and appear as lens-shaped segments. Below the enhanced reflections, a zone of acoustic masking is observed (figure 4-14). A south-dipping fault is identified reaching from the seafloor and down to ~3800 ms (TWT). The fault is situated below a topographic elevated area (figure 4-14). A similar faulting trend is also observed on the other seismic lines oriented across the ridge (figure 4-15), the dip of the faults is however deviating.
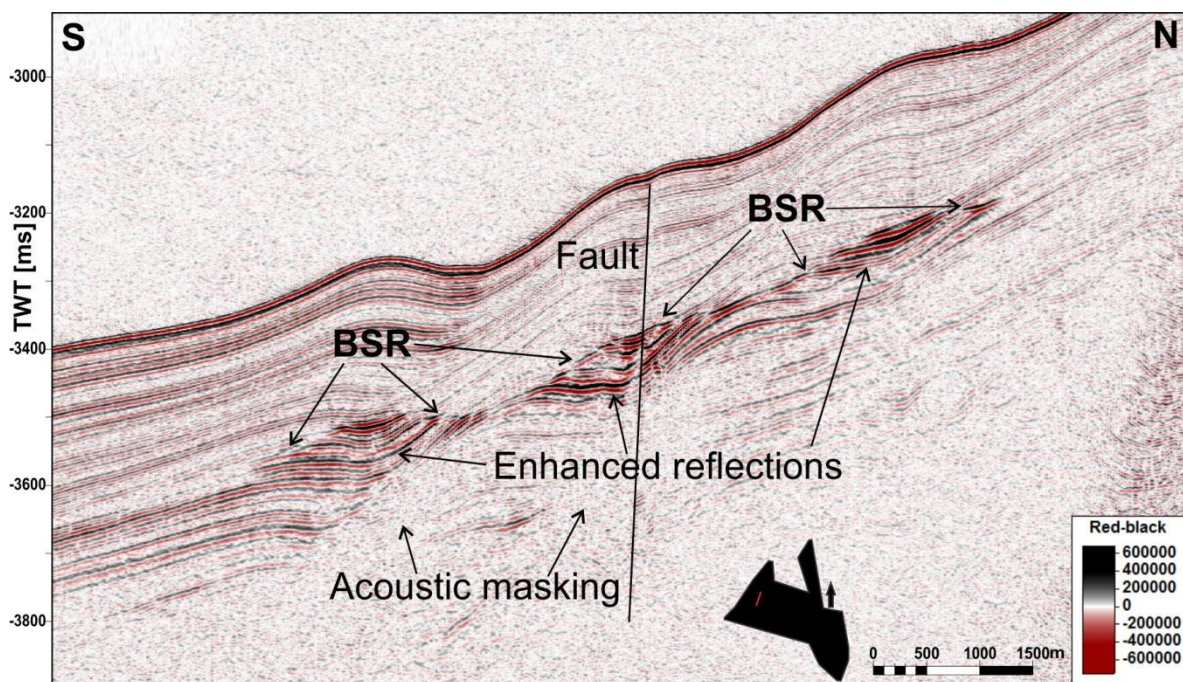
Figure 4-14: Seismic section from the southern flank of the Vestnesa Ridge. A BSR is terminating enhanced reflections that form lens-shaped segments. Beneath the enhanced reflections, a zone of acoustic masking is observed. A south-dipping fault is reaching from the seafloor, piercing through the BSR and the enhanced reflections and can be recognized in the zone of acoustic masking.

In closer distance to the ridge crest, the BSR is mimicking the seafloor along the termination of enhanced reflections and it is difficult to identify as a continuous reflection (figure 4-15). In areas where the seismic sedimentary strata are not parallel to the seafloor, the BSR crosscuts these. The BSR show strongest amplitudes at the crest and a general decrease in strength is observed towards the south. Enhanced reflections showing strong amplitudes are observed beneath the BSR (figure 4-15, inserted). Beneath the enhanced reflections, an acoustic turbidity zone is observed, which is most likely caused by seismic energy loss due to the presence of free gas. A north-dipping

fault is observed penetrating both the BSR and the high amplitude zone reaching to the uppermost part of the sediments just below the seafloor.
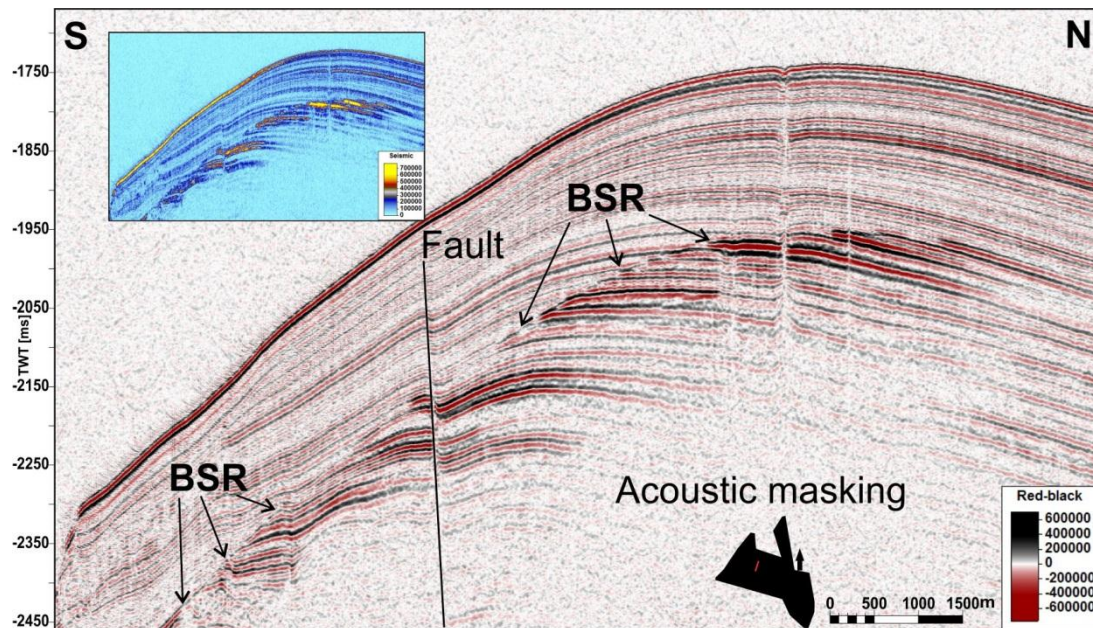
Figure 4-15: Seismic profile across the Vestnesa Ridge showing the BSR identified as the termination of enhanced reflections. A north-dipping fault is penetrating the sedimentary strata. Inserted image show a reflection strength plot where the strong amplitudes are clearly seen.

4.2 BSR at the Molloy Transform Fault

Four 2D seismic lines are covering the deep sea area including the MTF which stretches out in NW-SE direction, where the profiles going along the continental slope cross the MTF (figure 3-1 and 4-1). In the deep ocean basin the reflection pattern is less complicated than the rest of the continental slope (figure 4-16). The gradient is approximately 0,5° in this area, which might be a contributing factor for the orderly arranged reflection pattern.

The BSR is identified in close distance, and at the MTF in water depths between ~1900 m and 2900 m at 200-260 ms (TWT) bsf (figures 4-16 to 4-19). The BSR is identified as the upper termination of enhanced reflections (figure 4-16), or as a continuous reflection (figure 4-17) showing reversed polarity relative to the seafloor reflection. The BSR is in either way dominated by high amplitude values and high reflection strength. The seismic character of the stratigraphic interval above the BSR show reflections of much lower amplitude values than below. Polarity reversal across the BSR is observed at some places where the BSR terminates enhanced reflections (figure 4-19).

 In the NW part of the MTF, on the northernmost seismic line covering the MTF, the BSR is identified in well stratified sediments (figure 4-16). From the MTF the BSR is terminated by enhanced reflections that can be followed for ~16 km in eastward direction towards two normal-faults forming a graben structure (figure 4-16). The offset is ~50 ms (TWT) for the eastern fault and ~20 ms (TWT)

for the western fault. Figure 4-16 (inserted) shows a reflection strength display in close up of the faults where strong reflections are observed in vicinity of the fault planes. The BSR fades out west of the MTF where the reflection configuration pattern is much more chaotic than east of the MTF.
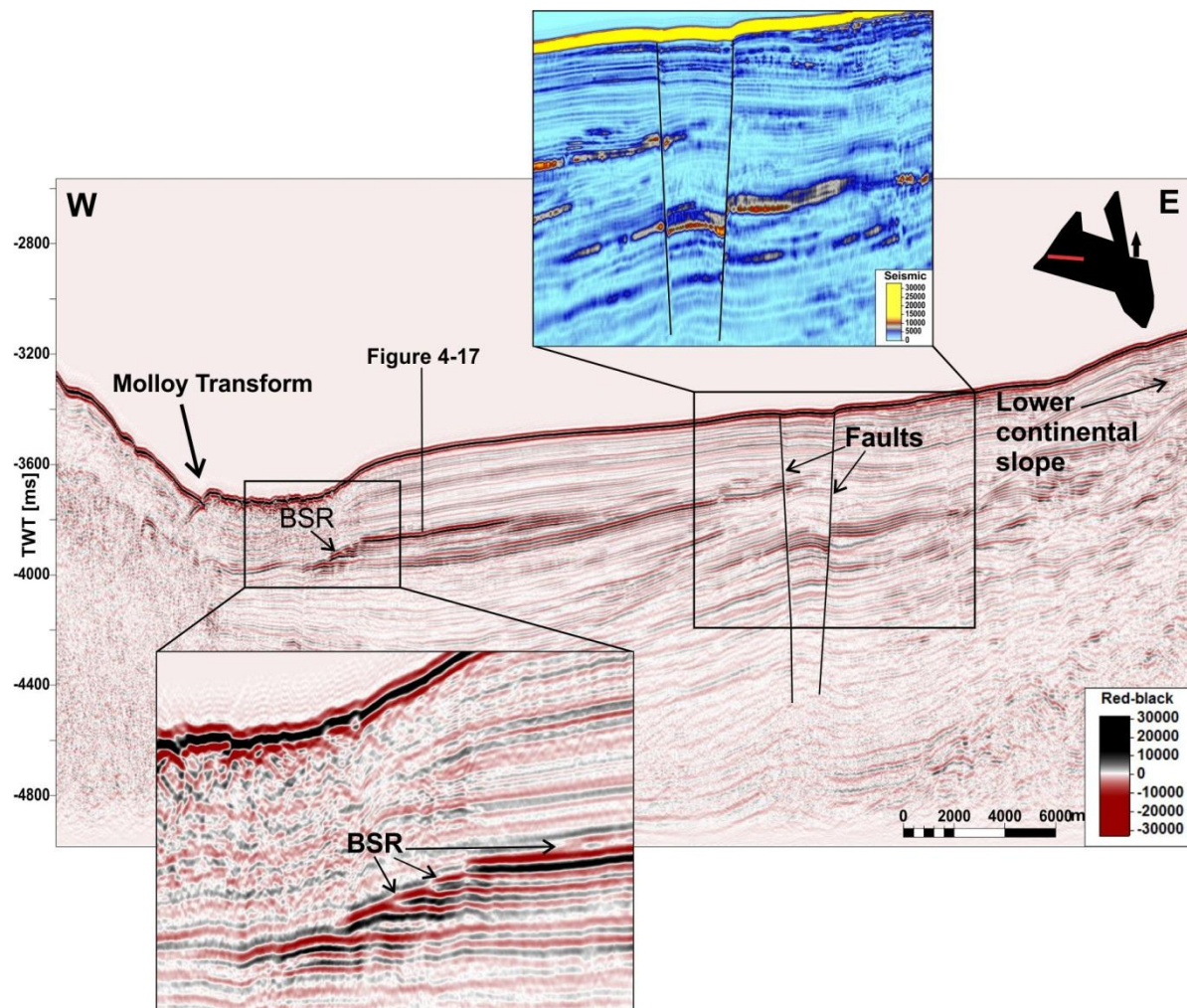
Figure 4-16: Seismic profile from the abyssal plain including the MTF. A BSR is observed terminating enhanced reflections close to the MTF (inserted). Two normal-faults are observed in the eastern part of the basin, terminating high amplitude reflections (inserted).

On a seismic profile going in N-S direction, the BSR is observed as a continuous reflection that terminates underlying strong reflections (figure 4-17, see figure 4-16 for crossing point). At the MTF, the general reflection pattern is chaotic showing little continuity. The BSR can be followed from close distance of the MTF in northward direction for approximately 5 km. An interesting observation from this area is that the sub-bottom depth of the BSR is increasing from 200 ms (TWT) bsf close to the MTF in south to ~240 ms (TWT) bsf towards north over the ~5 km long BSR segment. This observed shoaling of the BSR toward the MTF points to elevated heat flow. Above the inferred BSR a ~30 ms (TWT) interval of amplitude blanking is observed, possibly caused by the reduction of the impedance contrast of the gas hydrate bearing strata similar to observations on the Blake Ridge (Hornbach et al., 2003). An approximately 4 km long zone above the blanking zone and up to the

seafloor is characterized by a disrupted reflection pattern with discontinuous reflections. The
reflections show an increasingly degree of stratification toward north, with continuous parallel
reflections demonstrating an undisturbed, well-stratified sedimentary sequence where the BSR is
difficult to distinguish.
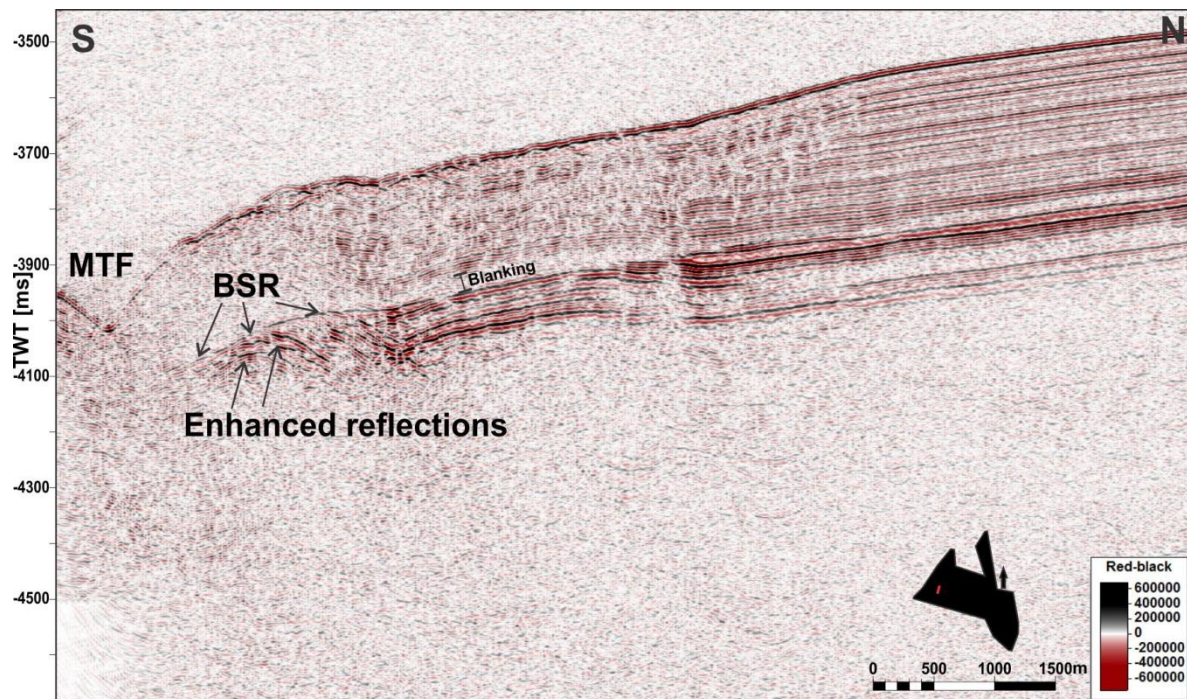
Figure 4-17: Seismic profile from the abyssal plain and the MTF. A BSR is observed as a continuous reflection close to the MTF with underlying enhanced reflections. The sub-bottom depth of the BSR is observed to decrease towards the south. Above the BSR a ~30 ms (TWT) interval of amplitude blanking is observed.

Following the MTF in SE direction the BSR can be observed as a continuous reflection just at the MTF
(figure 4-18). The area west of the MTF is dominated by several faults that can be observed to a
depth of ~400 ms (TWT) bsf with largest offset of about 30 ms (figure 4-18). The area east of the
MTF show well stratified reflectors with no signs of faulting or fluid flow features. The well stratified,
parallel configuration pattern includes a sequence of ~500 ms (TWT) bsf. Below this interval, a
chaotic reflection pattern with internal continuous reflectors with high amplitudes is observed.
Brauti (2005) implied that this pattern could be related to debris-flow deposits or slumping where
the continuous reflectors can represent possible internal glide planes.
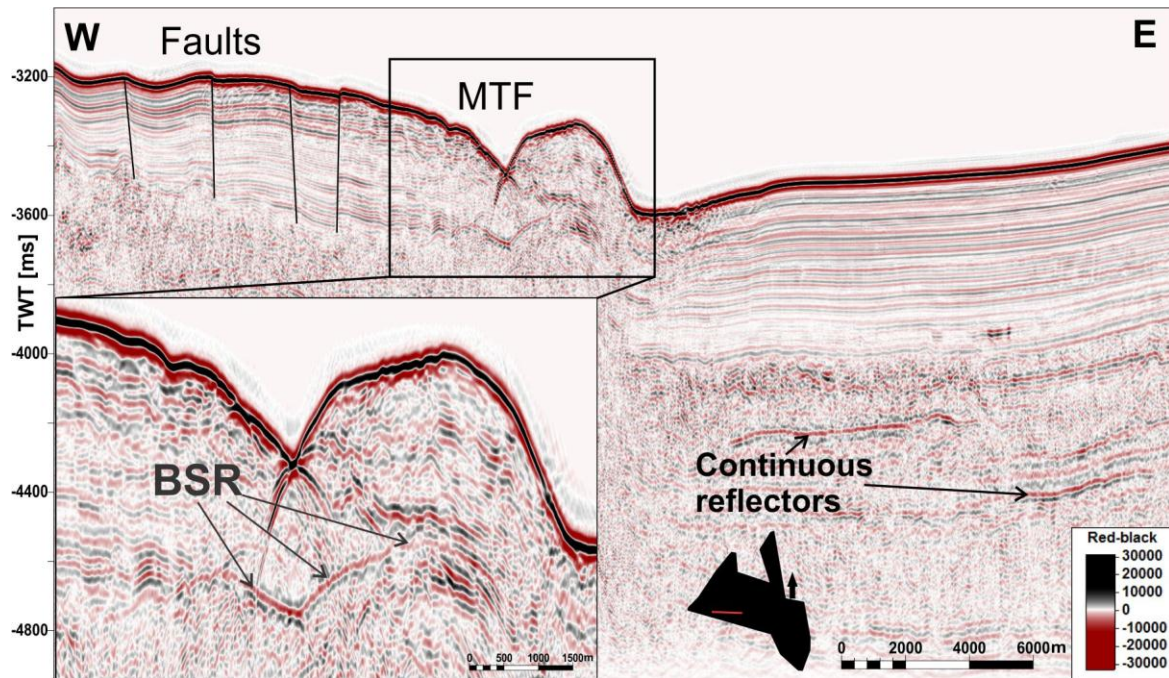
Figure 4-18: Seismic profile from the MTF showing a BSR as a continuous reflection (inserted). In the area west of the MTF several faults are observed terminating the seafloor. The area east of the MTF show well stratified layers down to ~500 ms (TWT) bsf. Below this sequence a chaotic reflection pattern with internal continuous reflections are observed.

On the southernmost seismic line covering the MTF, the BSR is clearly a single reflection with reversed polarity relative to the seafloor (figure 4-19). The sediment cover at the MTF is in this area nearly transparent. Upslope in eastward direction, the BSR is readily identified as the termination of enhanced reflections that strongly crosscuts sedimentary strata. The variation in the reflection amplitude of the BSR in this area is great, as well as the extent of enhanced reflections underneath the BSR.
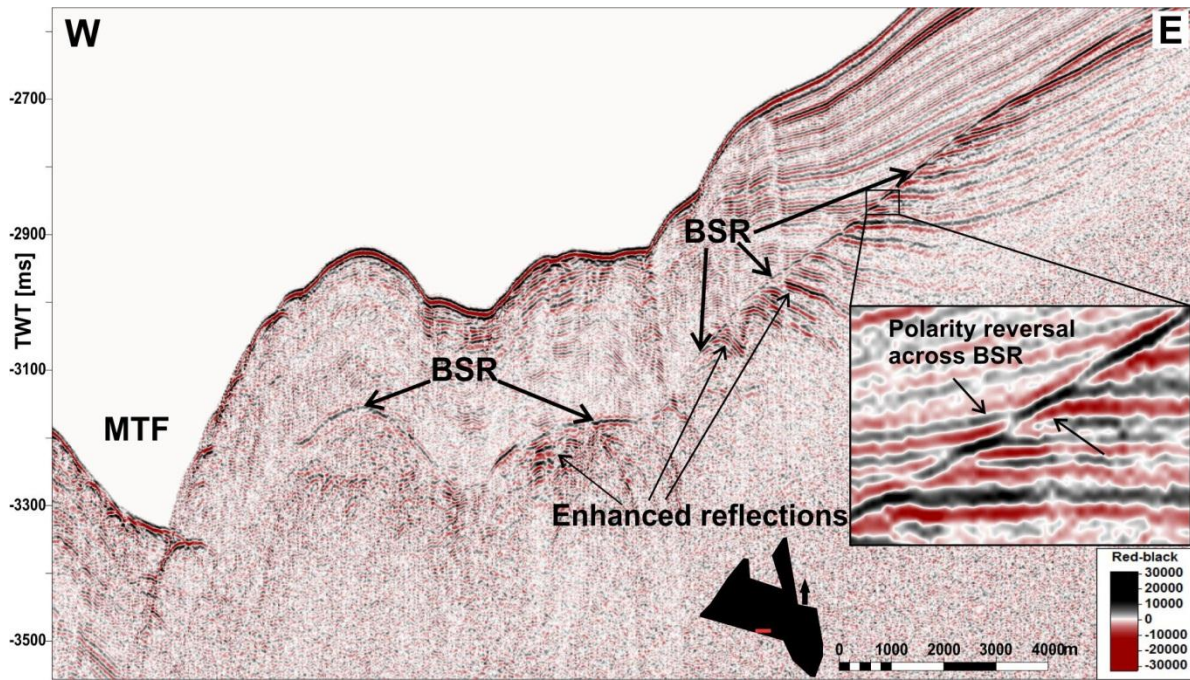
Figure 4-19: Seismic profile from the MTF area showing a BSR as a continuous reflection to the west and as the termination of enhanced reflections in the east. Here, polarity reversal across the BSR is observed (inserted).

4.3 BSR on the continental slope

The continental slope can be divided into upper and lower continental slope and abyssal plain (figure 4-20). On the three seismic profiles going along the continental slope, the BSR can be identified both as a continuous reflection and as the termination of enhanced reflections at 220-250 ms (TWT) bsf, showing lateral amplitude variations (figure 4-21 and 4-22). The BSR is observed from the Molloy Transform Fault in the west towards a topographic high that marks the limit between the upper and lower continental slope in east (figure 4-21). The BSR is observed in water depths varying from ~2500 m to ~700 m.
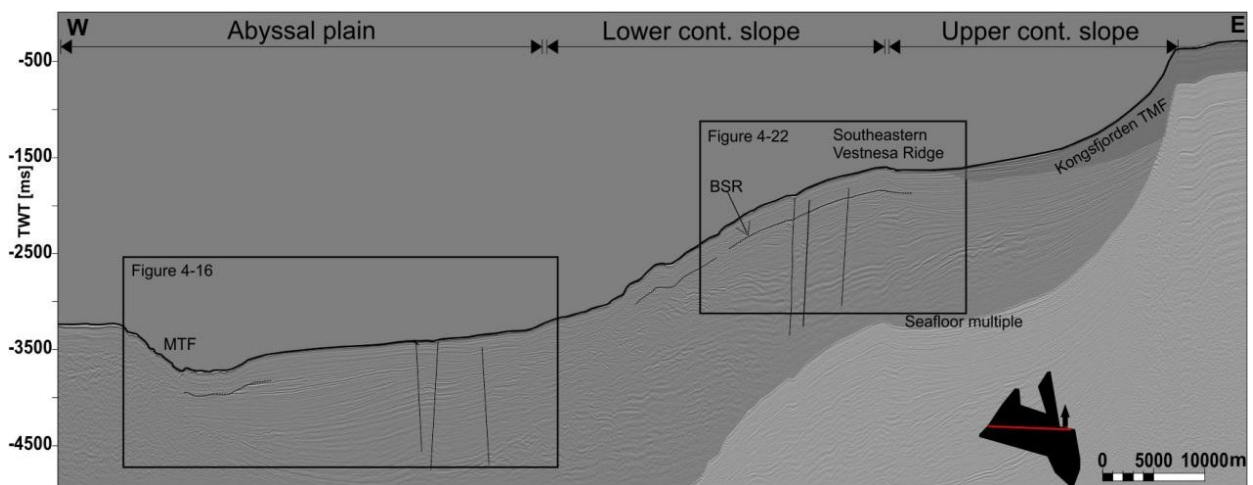
Figure 4-20: Profile of the continental slope illustrating the subdivision of the abyssal plain and lower and upper slope.

The BSR is most prominent on the lower continental slope and generally weakens upslope and is not observed at the upper part of the slope. Here the slope is steep with a gradient up to approximately 4° towards the shelf edge. The upper sedimentary sequence of the upper slope area show less stratification and is characterized by parallel to sub-parallel reflections that increases in thickness towards the shelf edge. The upper slope is influenced by glacier-derived sediments originating from the Kongsfjord trough-mouth fan (Vorren and Laberg, 1997) (figure 4-20). These sediments are interpreted to represent glacigenic debris flow deposits (GDF). The sequence pinches out ~25 km from the shelf edge.

On the lower continental slope the BSR is identified in an area dominated by wavy reflection configuration and a discontinuous and chaotic reflection pattern (figure 4-21). The BSR marks a vertical transition between these underlying wavy patterns and overlying parallel strata. The wavy reflection pattern is interpreted to represent contourites, as such are known to emerge with internal forms like migrating sediment waves on seismic sections (Mitchum et al., 1977; Eiken and Hinz, 1993).

Faults and vertical pipe structures present in the area are cutting the BSR at several places (figure 4-21 and 4-22). The faults are commonly reaching the seafloor and are interpreted to represent normal-faults developed as a consequence of extension. The most prominent faults can be followed from the seafloor and down to the first seafloor multiple indicating recent activity. The faults largely coincide with faults described by Crane et al. (2001). Crane et al. (2001) described faults trending parallel to both the ridge and transform, cutting the Vestnesa Ridge from south to north along its boundary with the Spitsbergen continental margin. They were suggested to be a northwards extension of the eastern rift valley walls of the Knipovich Ridge to the south. The faults were reported to be located in a 5,5 km corridor and because of their structural connection with the mid-ocean ridge, it was suggested as an evidence of ongoing or recent northerly rift propagation (Crane et al., 2001).

Within the sequence of wavy reflections, zones of high amplitudes (e.g. bright spots) are recognized in an up to 1300 ms (TWT) interval beneath the BSR (figure 4-21). Some of the high amplitudes are terminated by the BSR, while others appear at deeper stratigraphic levels in vicinity of faults and pipe-structures. In the same interval, zones of lower amplitudes are also observed, appearing as acoustic masking probably related to gas in the overlying sediments.
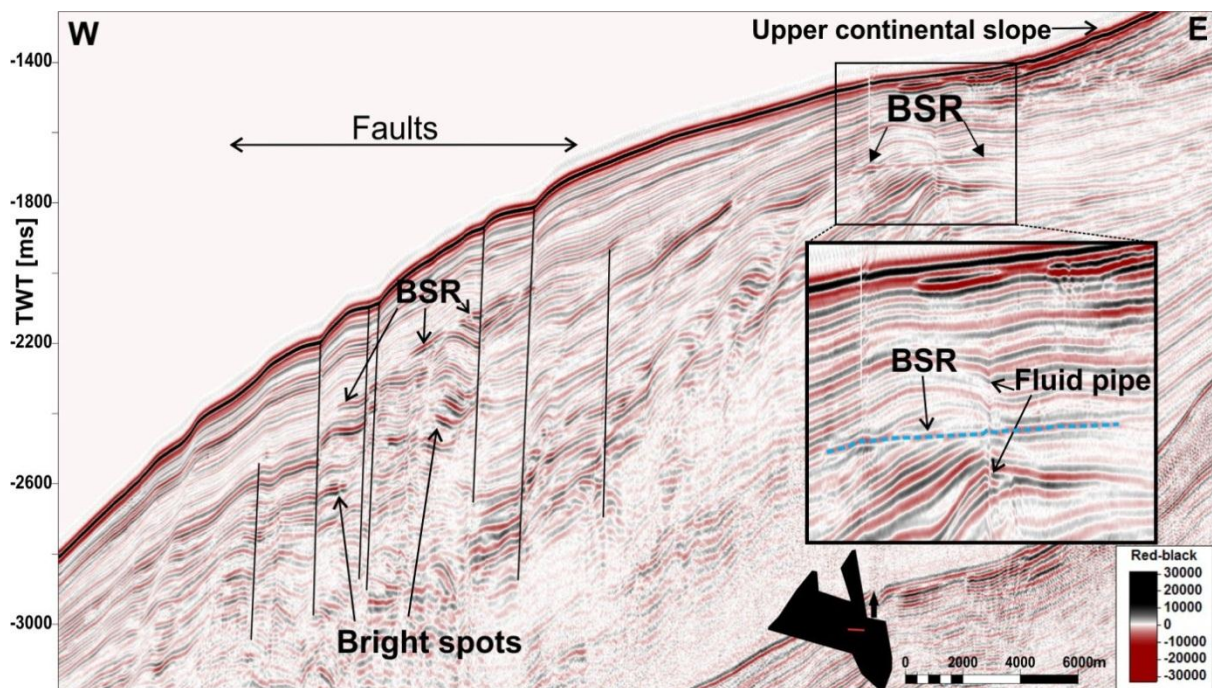
Figure 4-21: Seismic profile from the lower continental slope showing a BSR in a zone of wavy reflection pattern. Faults and pipe structures are observed within the same sequence, cutting the BSR at several places. High amplitude anomalies (i.e. bright spots) are observed in vicinity of the faults. The inserted image shows the strong cross-cutting nature of the BSR.

A topographic high making up the southeastern Vestnesa Ridge on the transition between lower and upper continental slope, clearly shows a BSR at ~200 ms (TWT) bsf (figure 4-22). The BSR can be followed for ~3 km in landward direction and ~14 km in seaward direction from the crest. The high is inferred to be a result of the build-up of contourites (Eiken and Hinz, 1993). The BSR compose an anticline below the ridge crest due to the topography of the ridge and the cross-bedded stratigraphy of contourite deposits (Hustoft et al., 2009). The BSR is nearly uninterrupted in the ridge area. Beneath the BSR a high reflectivity zone can be observed, showing maximum thickness just below the crest.

Following the continental slope in western direction, the reflection show an increasingly degree of stratification as the slope angle decreases (figure 4-16 and 4-20). The BSR fades out in this area, and is difficult to identify due to the parallel layering.
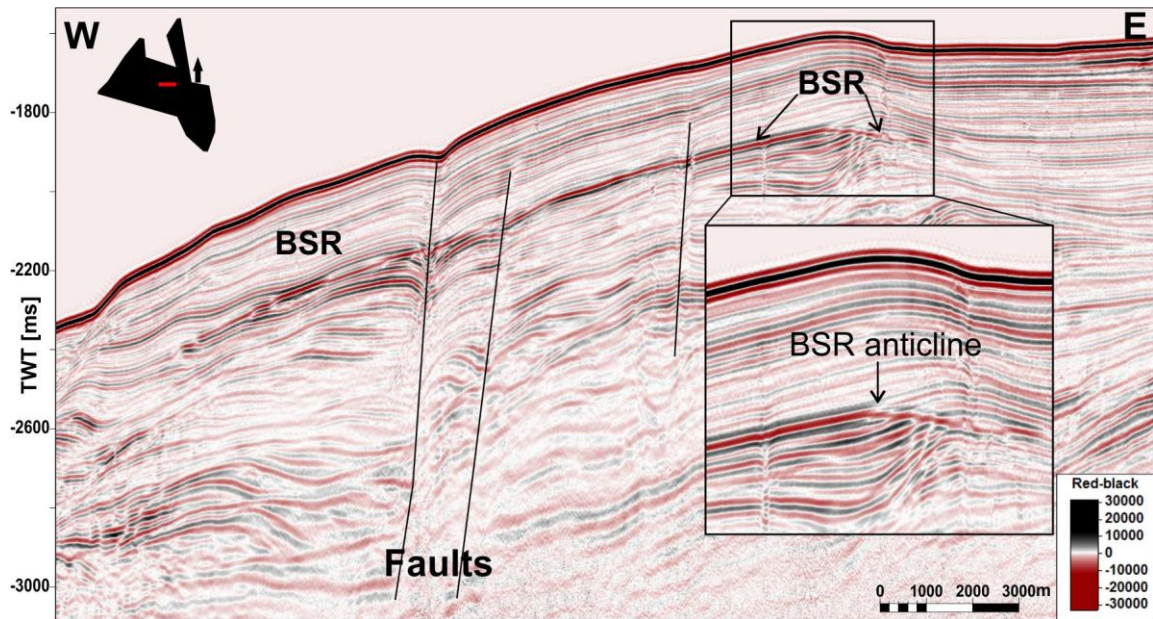
Figure 4-22: Seismic profile from the lower continental slope showing a continuous BSR. Faults are observed to interrupt the BSR. The inserted image shows a BSR anticline with enhanced reflections beneath it.

5. Discussion

The result chapter presented the appearance of a gas-hydrate related BSR in three different areas including the Vestnesa Ridge crest and flanks, the MTF and the continental slope. The presence of the BSR in these very different geological settings will be discussed in terms of geological processes that control the occurrence of gas hydrates and the formation of a BSR. Given the widespread occurrence of fluid-flow indicators, I discuss the fluid migration system and fluid accumulation mechanism also related to the presence of gas hydrates. A modeling of gas-hydrate stability is carried out in order to enlighten the source of gas and the dynamic state of the free-gas/gas-hydrate system.

5.1 Seismic indicators of gas hydrate presence

The most obvious indication of the presence of gas hydrates on the western Svalbard margin is the observation of a BSR. Seafloor mimicking, polarity reversal and crosscutting of stratigraphic boundaries are all characteristics of the BSR relating it to the presence of gas hydrates. There are also other indicators from seismic data that can assist the gas hydrate interpretation, such as frequency content, amplitude blanking and enhanced reflections.

The instantaneous frequency attribute allowed the inferring of the presence of gas hydrates within the sediments (figure 4-6 and 4-9 c). It is widely accepted to associate areas with low frequencies with higher degree of attenuation and vice versa. This assumption gives a proportional relationship between frequency and attenuation (Petersen et al., 2008). Similar observations in instantaneous frequency changes across the BGHSZ have also been described from other locations (Berndt et al., 2004). Taylor et al. (2000) reported a drop of instantaneous frequency underneath the BSR on the Blake Outer Ridge and addressed it to free gas absorbing the high-frequency component of the seismic energy, which is consistent with the observation in this thesis, and corroborates the observations of the BSR being hydrate related as well as verifying the presence of free gas underneath it.

A 2D seismic line close to the MTF shows an interval of ~30 ms (TWT) with reduced reflection amplitude, observed above the BSR (figure 4-17). This phenomenon is called amplitude blanking and has previously been described as a useful indicator of gas hydrate accumulations (Shipley et al., 1979). Holbrook et al. (1996) described amplitude blanking as a consequence of either lithologic homogeneity of the sediments or by hydrate cementation. Amplitude blanking is however dependent on hydrate saturation as layers containing sufficiently high concentrations of hydrate can enhance reflectance because of their higher velocity compared with surrounding strata (Holbrook et al., 2002). Due to the presence of a BSR underneath the blanking zone, it is reasonable to assume that it is caused by the cementation effect of gas hydrates. Amplitude blanking may also be a good gas hydrate indicator in cases where a BSR is absent, weak or suspicious.

At several places in the study area, the BSR is observed as the upper termination of enhanced reflections that stretch laterally and underneath the BSR (figures 4-9 a and b, 4-14, 4-16 and 4-19). Previous studies have addressed the occurrence of enhanced reflections in gas hydrate settings (Chand and Minshull, 2003; Popescu et al., 2007). Below the inferred BSR, free gas is believed to exist along strata increasing the acoustic impedance contrast, which will give rise to a pattern of enhanced reflections on seismic data. The enhanced reflections will terminate when they reach the BGHSZ, where hydrates have the possibility to trap the gas. Because of the relation between the

enhanced reflections and the presence of free gas, the varying reflection amplitudes are a result of contrasting gas saturations possibly due to different porosities in adjacent layers (Bünz and Mienert, 2004).

5.2 Distribution and appearance of the BSR in the study area

A gas-hydrate related BSR was extensively observed in the study area (figure 5-1). There are also regions with no BSR observation. The different regions show great variation concerning water depth, geothermal gradients, sedimentary environment and structural pattern. The different settings that the BSR occur in, leads to a subdivision into three regions, being the Vestnesa Ridge, the continental slope and the MTF (figure 5-1). It is clear that the distribution of the BSR varies within the study area, where some conditions seem to exclude the presence of a BSR, whereas other conditions seem to favor the formation of gas hydrates and the presence of a BSR. Here, the different areas will be discussed in order to enlighten the conditions that favor gas hydrate formation and the presence of a BSR on the seismic data.
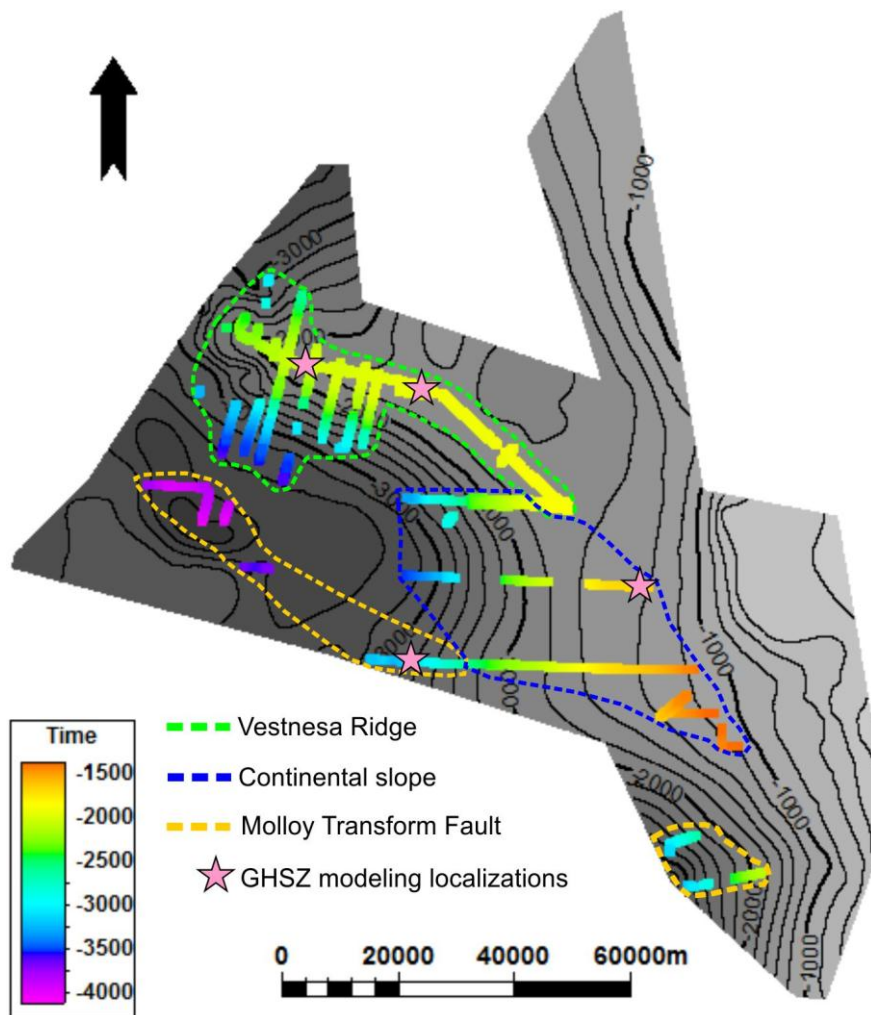
Figure 5-1: The BSR interpretation from the study area leads to a subdivision of three areas indicated on the map. The pink stars indicate localizations for GHSZ modeling (please refer to chapter 5.4).

5.2.1 Area extent

Based on the seismic interpretation, the area, in which the BSR occurs, can be used to interpolate an approximate extent of gas hydrate occurrence in the area. The interpolation shows that the three different regions comprise an area of approximately 2700 km^2 (figure 5-1). This is a rough estimation as the BSR is not observed over the entire study area and some areas without data coverage are included in the calculation assuming the BSR is present also here. It includes also places where the spacing between 2D lines is large. The seismic observations indicate that the area is an active fluid migration zone, and assuming that the origin of the BSR is caused by the free gas zone below hydrate-bearing sediments, it can also be assumed that gas hydrates might be present without the presence of a BSR. It is therefore possible that the extension of gas hydrates is larger than inferred from observations made from seismic interpretation.

The estimation of 2700 km^2 is much larger than the 1600 km^2 estimate suggested by Vanneste et al. (2005[b]), but assumed to be reasonable compared to the estimate of ~3000 km^2 proposed by Bünz et al. (2008). From the estimate by Bünz et al. (2008), Hustoft et al. (2009) suggested that the total amount of in situ methane stored as hydrate and gas could be as much as ~0,7±0,2 billion metric tons (Gt). This estimate is considered relatively conservative since the thickness of the hydrate and gas zone may locally be greatly enhanced in the presence of faults and beneath the Vestnesa Ridge crest as well as the fact that the BSR may be more widespread (Hustoft et al., 2009).

5.2.2 The upper continental slope

The upper continental slope is characterized by glacigenic debris-flow deposits where a BSR is not observed (figure 4-20 and 4-21). In addition, there are no observations of amplitude anomalies from which free gas in the sediments could be inferred from. The lack of BSR observations from the upper continental slope is probably a result of the GDF deposits occurring here. Due to the thickness of these sediments, it is expected that the BGHSZ falls within this section which can be confirmed by calculating the theoretical predicted BGHSZ. A similar observation has been described on the mid-Norwegian margin where Bünz et al. (2003) concluded that due to the impermeability of GDF deposits, upward migration of fluids that could form gas hydrates is efficiently inhibited. Also, there are no signs of faults or fluid flow structures that could act as migration pathways for gas into the GHSZ. The eastern termination of the inferred gas hydrate occurrence fits well with the western termination of the GDF deposits (figure 4-21). It is therefore suggested that the eastern extent of gas hydrates is bound by the GDF deposits as similarly observed at the mid-Norwegian margin.

5.2.3 The lower continental slope

A prominent BSR stands out in the area of the lower continental slope, and is observed as a nearly continuous reflection for ~20 km (figure 4-21, 4-22 and 5-1). The BSR seems to represent a vertical transition between wavy reflections below and overlying parallel strata. Eiken and Hinz (1993) suggest that such vertical changes in seismic pattern may result from changes in current intensities through times. The chaotic and discontinuous seismic pattern observed beneath the BSR (figure 4-21 and 4-22) indicates the influence of along-slope and/or downslope processes. Several normal-faults observed in the area (figure 4-21) may also affect the seismic reflection patter as well as the presence of gas in the sediments.

The wavy reflection pattern on the lower continental slope is thought to represent contourites (figure 4-21 and 4-22). Eiken and Hinz (1993) interprets the wavy reflection pattern as an indication of contourites of Late Miocene to Pliocene being controlling factors for most of the depositions in the upper sequences on the continental slope on the western Svalbard margin, and that migrating sediment waves of this scale are normally formed by deep thermohaline currents. The relatively thick sequence of wavy reflections indicates that this current regime has been persistent over long time with high sedimentation rates. The build-up of these sediments is most likely responsible for the topographic high marking the transition between the lower- and upper continental slope (figure 4-22). As a BSR anticline is observed beneath the topographic high, it is inferred that the topography is a favorable condition for the formation of gas hydrates. As muddy contourites are unlikely to serve as good reservoir rocks (Stow and Lovell, 1979), it has previously been assumed that the apparent presence of gas indicates a significant sand fraction (Eiken and Hinz, 1993). It is therefore assumed that also the lithological properties of the sediments are favorable when it comes to accumulation of gas and the formation of gas hydrates. In western direction the BSR fades out where the reflections show parallel layering relative to the seafloor and the gradient of the slope decreases (figure 4-20). This is suggested to represent the western boundary for the BSR distribution on the lower continental slope.

5.2.4 Abyssal plain

Between the lower continental slope and the MTF, the BSR observations are sparse (figure 4-16, 4-18, 4-20 and 5-1). This area covers the eastern part of the abyssal plain and the transition to the lower continental slope. With exception of a limited number of observed faults (figure 4-16 and 4-20), this area does not show any fluid flow structures such as acoustic chimneys and pipes, nor any seafloor fluid flow expressions such as pockmarks. The lack of fluid migration pathways could indicate that fluids are less widespread here. The decreased supply of gas-rich fluids prevents formation of gas hydrates and the appearance of a BSR on seismic data. It is reasonable to assume

that the sedimentary environment in this area is a contributing factor concerning the lack of fluid flow structures and gas hydrate formation. The upper sequence (i.e. the upper 500 ms TWT) of the abyssal plain (figure 4-18) is characterized by well stratified sediments indicating a different depositional regime compared to the slope. Eiken and Hinz (1993) have previously interpreted the sediments here to mainly consist of turbidites originating from the continental slope. However, the gradient of the seafloor is low, and the sub-seafloor sedimentary layering is almost perfectly parallel to the seafloor. The identification of a BSR is hampered in such an environment, but also there might be relatively little topographic control that could focus fluid migration to an extent, where hydrates could be formed within the GHSZ.

5.2.5 Molloy Transform Fault

The BSR is for the most absent in the deep waters of the abyssal plain. Approaching the MTF, however, the BSR is observed again, fulfilling the criteria relating it to gas hydrates (figure 4-16 to 4-19, figure 5-1). The sediments in the deep water area of the MTF comprise a relatively thin sequence of a few hundred meters and are assumed to be turbidites or glaciomarine and hemipelagic originating from the continental slope that is partly reworked by contour-currents (Eiken and Hinz, 1993; Vorren et al., 1998). The underlying young and hot crust may play a part in the generation of sufficient amount of gas in order for gas hydrates to be formed here and the presence of a BSR on seismic data. This is to be discussed further in chapter 5.4. The observation of fluid flow is limited in the area of the MTF, but faults are however observed west of the MTF (figure 4-18). Here, the BSR is absent, suggesting the MTF as a western boundary for the BSR distribution in the study area. Also, amplitude anomalies are not observed in vicinity of the faults that could relate them to fluid flow. The faults are located in close distance to the MTF and the Knipovich Ridge and they are tectonically active (Crane et al., 2001).

5.2.6 Vestnesa Ridge flanks

The flanks of the Vestnesa Ridge show well stratified sediments and no signs of seafloor pockmarks (figure 4-14 and 4-15). A BSR is however readily identified on the southern flank indicating that gas hydrates are present here (figure 4-14 and 4-15, figure 5-1). According to a theoretical study by Nimblett and Ruppel (2003), gas hydrates have the ability to significantly reduce the permeability of sediments, which in turn affects the fluid flux, eventually creating a barrier to further migration of gas. The reduced permeability can therefore act as an effective seal where free gas is trapped beneath the hydrate-bearing sediments. Bünz et al. (2008) suggest that the gas hydrates of the Vestnesa Ridge flanks exhibit such sealing properties on the background that gas hydrates are present in the entire ridge, whereas fluid flow structures are confined to the crest. Vertical fluid flux

is therefore inhibited on the flanks, where the gas is forced to migrate laterally underneath the BSR (i.e. the BGHSZ) eventually accumulating at the crest as the fluids cannot migrate further laterally.

At the southern flank of the ridge, topographic highs interpreted as contour drifts are observed (figure 4-14). Directly beneath the drifts, gas seems to accumulate, as lens-shaped areas of high amplitudes are located beneath the BSR. It seems likely that the gas accumulations in this area are affected by the topography of the seafloor, suggesting a local topography-driven fluid-flow. Beneath the enhanced reflection a large zone of acoustic masking is observed (figure 4-14 and 4-15). Considered the overlying enhanced reflections, it is possible that a large amount of gas is present in the sediments. In connection to one of the drifts, a fault is observed piercing the sedimentary strata from below the BSR and all the way up to the seafloor (figure 4-14). The fault may have the possibility to act as a conduit for fluid migration, but because no amplitude anomalies are observed in vicinity of the fault, it is assumed that fluid migration is limited here. A barely visible depression is observed where the fault terminates the seafloor (figure 4-14). The depression is not thought to represent a pockmark, but rather a fault escarpment.

5.3 Gas accumulation and migration

The western Svalbard margin and the Vestnesa Ridge compose a sedimentary basin overlying a young (<20 Ma) oceanic crust. An up to 5 km thick post-rift sedimentary succession occurs at the eastern Vestnesa Basin decreasing to a few hundreds of meters of sediments at the Knipovich Ridge and MTF (Ritzmann et al., 2004; Breivik et al., 1999). The young, relatively hot oceanic crust makes this a very unique setting that clearly affects the fluid-flow system. Hustoft et al. (2009) discovered seepage of methane from the seabed on the Vestnesa Ridge indicating the active discharge of fluids from subsurface sediments. The exact origin of the fluids has yet to be investigated. However, Hustoft et al. (2009) speculate that the thermal structure and the evolution of the oceanic crust drives biogenic and thermogenic methane generation, and hence the migration of fluids in Vestnesa Ridge sediments, at the MTF and on the continental slope.

The Vestnesa Ridge crest is believed to function as a pressure valve for the continuing gas accumulation leading to pressure build-ups (Bünz et al., 2008). With time the pressure will increase to a critical level requiring pressure-release. Fluid may be released through the numerous chimneys, pipes and faults observed at the crest (figure 4-8, 4-9 and 4-12). Both old chimneys/pipes and formation of new structures may act as fluid conduits. Hustoft et al. (2009) suggested that hydrothermal circulation through young oceanic crust may play a significant role for the gas-hydrate system on the western Svalbard margin. A possible consequence of such hydrothermal-controlled system is dislocated and disturbed BGHSZ where warm fluids are focused upwards. This can be

observed at several places along the crest, where the BSR is frequently disrupted or absent in vicinity of fluid flow structures (figure 4-8 and 4-9). Close to the vertical fluid flow structures, the BSR commonly loses its seafloor-simulating character (figure 4-8 and 4-9). Klerkx et al. (2006) described a similar observation in Lake Baikal, which is consistent with the observations presented in this thesis. It was suggested that the irregular morphology of the BSR is predominantly temperature-controlled and directly related to the existence of a local anomaly of increased heat flow. Because of the temperature-sensitivity of gas hydrates, the disruption of the BSR is thought to involve local destabilization of hydrates within the fluid flow structures. As a consequence, the BSR is either absent or present at a shallower depth.

The heat-flow values on the western Svalbard margin are on average two to three times higher compared to the mid-Norwegian margin. This implies a strong temperature-controlled system compared to the mid-Norwegian margin where the gas hydrate occurrence depends strongly on the geological settings (Bünz et al., 2003). An observation from the study area that strengthens this argument is the obvious shoaling of the BSR close to the MTF (figure 4-17). Normally, higher hydrostatic load on the pore fluids will cause a deepening of the BSR on seismic sections (Madrussani et al., 2010). However, the sub-bottom depth of the BSR is observed at ~200 ms (TWT) close to the MTF, gradually increasing to ~230 ms (TWT) over a distance of ~5 km in northward direction away from the MTF (figure 4-17). The observations are in agreement with observations made by Posewang and Mienert (1999) and Vanneste et al. (2005[b]) along the western Svalbard margin, who addresses the BSR shoaling to the proximity of the Knipovich Ridge inducing higher heat-flow, thereby a sub-seafloor temperature increase downslope.

Within several of the chimney structures observed at the ridge crest, the BSR appear as a pulled-up feature (figure 4-10). From the thickness map between the seafloor and the BSR surface, areas of decreased thickness are clearly observed, coinciding with seafloor pockmarks and acoustic chimneys (figure 4-7). This has previously been observed at the Vestnesa Ridge crest by Petersen et al. (2010) who suggested that the pull-up may be attributed to high seismic velocity within the chimney due to a higher concentration of gas hydrates. Mechanical deformation of the sediments was also presented as a possible explanation. It is also reasonable to assume that the pull-up of the BSR is caused by a local change of the phase boundary as a result of thermal effects caused by the increased heat-flow from the fluids within the chimney as discussed above. A combination of these effects is also possible, as suggested by Petersen et al. (2010). The zone of velocity pull-up is directly overlying a zone of velocity push-down situated in the inferred free gas zone (figure 4-10). Such

feature may indicate a seismic velocity decrease due to the presence of free gas in the sediments (Badley, 1985).

Another phenomenon observed within some of the chimney structures at the Vestnesa Ridge crest, are high amplitude anomalies identified in the upper 100 ms (TWT) (figure 4-10). The RMS amplitude time slice from 1866 ms (TWT) show that the highest amplitude is confined to the inner part of the chimney (figure 4-11). Similar observations have been described as a possible consequence of the presence of hydrates and/or authigenic carbonates within the chimneys (Petersen et al. 2010). Further, Petersen et al. (2010) points out that precipitation of carbonates is restricted to the upper few meters of the sediments (i.e. the sulfate reducing zone), which means that potential carbonates must have been buried beneath sediments after their formation in order to occur at greater depths. Another explanation for the high amplitude might be presence of a small gas-pocket within the chimney. If this is the case, it must be assumed that free gas can exist in the GHSZ, limited by the presence of permeable pathways. A possible mechanism for preserving the gas within the GHSZ has been proposed by Suess et al. (1999) who suggested that the gas is surrounded by hydrated, impermeable sediment, which prevents water getting into contact with the free gas. The high amplitude observed (figure 4-10 and 4-11) occur even deeper than the ones described by Petersen et al. (2010). It is therefore more likely that the high amplitude is due to the presence of hydrates or free gas rather than carbonates.

The seismic data suggest the appearance of several faults located at different places in the study area. Faults are present at the ridge crest and flanks (figure 4-12, 4-14 and 4-15), the lower continental slope (figure 4-21 and 4-22), and the abyssal plain where some are located in close distance to the MTF (figure 4-16 and 4-18).

At the ridge crest, several of the fluid flow features such as chimneys and pipes are observed in close distance to faults or they are coinciding with faults (figure 4-12). Here, the faults are thought to represent important fluid migration pathways, allowing the gas to enter the GHSZ. Especially at greater depths where the sediments are more compacted, the faults may be important when it comes to upwards focusing of fluids. The variance time-slice sections (figure 4-13) show that chimneys 2, 3 and 4 are closely related to faults or fractures. The fault/fractures terminate at different stratigraphic levels (figure 4-12) and are oriented in different directions (figure 4-13). The structures are rooted well below the BGHSZ and can be recognized down to 2250 ms (TWT). This may indicate that gas is focused from a deeper level.

There are several observations of high amplitude anomalies (i.e. bright-spots) in vicinity of fault structures or along fault-planes (figure 4-16 and 4-21), which may be an indication that faults are pathways of focused fluid flow (Ligtenberg, 2005). The faults making up the graben structure on the abyssal plain show high reflection strength and bright-spots that are terminated by the faults (figure 4-16). This might indicate that the faults act as a migration pathway that focus the fluids upwards and into permeable and porous layers at shallower depths. If the faults are effective migration pathways for fluids into the GHSZ, a BSR would be expected here. A BSR is, however, not observed in this area. Hustoft (2005) performed a velocity analysis in this area and found relatively high interval velocities close to the seafloor compared to Hamilton's curve for acoustic velocities in normally compacted marine sediments. This might indicate that gas hydrates could be present here assuming that the migrating gas along the fault planes causes higher concentrations of gas hydrates. If gas migration along the faults is an episodic event it is possible that the gas accumulation below the BGHSZ is insufficient in the manner of creating a large enough acoustic impedance contrast for the BSR to be identified on seismic data. The parallel layering of the sediments relative to the seafloor can also be a factor that prevents the BSR from standing out in this area.

Enhanced reflections observed beneath the BSR have already been discussed, and are thought to represent layers with appropriate porosity and permeability to concentrate gas below the BGHSZ. Bünz et al. (2008) estimated the zone of enhanced reflections beneath the BSR to have a thickness of approximately 150 m. Together with the relatively thick zone of enhanced reflections, a large zone of acoustic masking exist beneath the enhanced reflections (figure 4-4, 4-14 and 4-15). This may indicate that a part of the gas is produced well beneath the BGHSZ and the area of enhanced reflections. This observation is corroborated by chimney structures that can be observed at deeper levels down to ~2100 ms (TWT) (figure 4-11) and connect with faults (figure 4-12 and 4-13).

5.4 GHSZ modeling

The BGHSZ is defined based on the observation of the inferred gas-hydrate related BSR. Many authors have used the BSR to estimate geothermal gradients beneath the seafloor, thus obtaining information on the heat flow and the thermal structure of continental margins (Yamano et al., 1982; Grevemeyer and Villinger, 2001; Vanneste et al., 2005[b]). Grevemeyer and Villinger (2001) document the importance of independent heat flow measurements to calibrate the modeling of gas-hydrate stability. Here, the objective of the GHSZ modeling is to further shed light on the dynamics of gas hydrate formation and the ensuing formation of a BSR, thereby investigating how well the observed BSR depth fits with the theoretical predicted depth of the GHSZ. The geothermal gradients were derived from heat-flow stations (Sundvor et al., 2000; Crane et al., 1982, 1988, 1991), and thus are very well constrained in the modeling. Hence, modeling locations were chosen based on the location of heat flow measurements (figure 5-2).

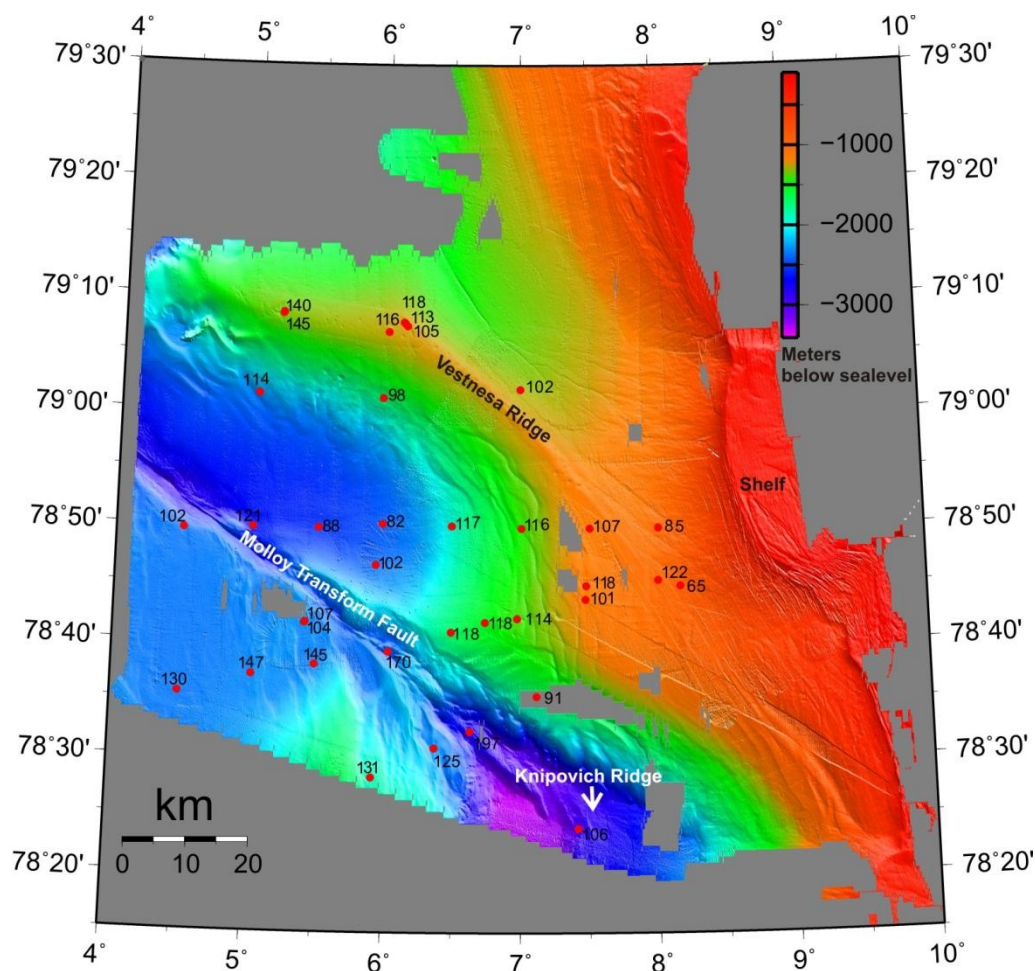**Figure 5-2: Bathymetry map of the area with the location of heat flow stations (Sundvor et al., 2000; Crane et al., 1982, 1988, 1991) marked with red dots. Corresponding values show the geothermal gradient derived from the stations.**

Consequently, the major unknown in the modeling is the composition of the gas. The modeling was carried out at four different locations including the MTF, the lower continental slope, and the

Vestnesa Ridge crest in distance from, and at pockmark locations, where heat-flow stations are nearby (figure 5-1). Modeling the hydrate stability zone also requires information about the bottom water temperature and the pore water salinity.

As indicated, the stability of gas hydrates is strongly controlled by the prevailing pressure- and temperature conditions in the sediments, where temperature has proven to be the most influential force (Ruppel, 2000; Max et al., 2006). The observed BSR depth might slightly deviate from the predicted BGHSZ due to properties of the sediment, capillary effects and geochemical potential, but these small deviations are of no significance for this study (Ruppel, 1997; Max et al., 2006).

The western Svalbard margin lies in close distance to the mid-oceanic ridge system and the gas-hydrate system here is therefore assumed to be significantly affected by large variation in heat flow from the mid-ocean ridge to the continental shelf. This is documented by the shoaling of the BSR towards the mid-ocean ridge and MTF indicating an increase in the geothermal gradient. Geothermal gradients on the western Svalbard margin have been suggested to vary between 65-118 °C/km (Crane et al., 1982) and 90-140 °C/km (Sundvor et al., 2000) based on in situ temperature measurements. Gradients have also previously been estimated using the BSR as an in situ temperature proxy, where the geothermal gradient was estimated to increase gradually from ~70°C/km at the upper slope to ~115°C/km at the MTF depression in water depths between 850 m and >2200 m (Vanneste et al., 2005[b]).

Also, local variations due to focused fluid flow through faults and/or acoustic chimneys/pipes are expected. Rising fluids usually are warmer than surrounding sediments leading to an increase in the geothermal gradient that will cause an uplift of the GHSZ, thereby reducing the GHSZ thickness (Ruppel, 2000; Feseker et al., 2008). On seismic data, this can be observed as local depth variations of the BSR indicating changes in heat flow (figure 4-7).

The sub-bottom depth of the GHSZ is also dependent of the bottom water temperature which varies from -0,9°C close to the MTF to >1,5°C towards the upper slope (Vanneste et al., 2005[b]). A higher bottom water temperature will in general move the GHSZ to a shallower level, and is therefore an important factor in GHSZ modeling. Seasonal variations in the bottom water temperature may occur, but concerning the relatively deep waters of the study area, a stable temperature is assumed. A bottom water temperature of -0,9°C was used during the modeling for all locations.

The salinity of the pore water is affecting the thickness of the GHSZ as salt is an inhibitor in gas hydrate formation, in such it lowers the hydrate formation temperature (Sloan, 1990). A higher pressure for gas-hydrate formation is therefore required if higher pore water salinity exist. Usually,

the pore water salinity is assumed to be similar to the seawater (35 SU; SU = 1000 ppm) (Chand et al., 2008), and is therefore used here.

Another complicating factor concerning GHSZ modeling is the composition and source of gas from which hydrate form (Chand et al., 2008). The gas composition will greatly affect the GHSZ thickness, where a higher fraction of heavier hydrocarbons result in a thicker GHSZ. It is suggested that methane is the dominant gas in the hydrate system along the western Svalbard margin (Vanneste et al., 2005[a]). Carbon isotope studies from the Barents Sea and the Spitsbergen region have, however, revealed the presence of higher order hydrocarbons in bottom waters, which preferably occur in vicinity of active seepage sites (Knies et al., 2004). Further, Knies et al. (2004) suggest that active petroleum source rocks along the western Spitsbergen continental margin and migrating gaseous hydrocarbons at re-activated fault systems might explain these findings.

The modeling was carried out using the CSMHYD software from Sloan (1998[b]) for assumed gas mixtures in the presence of NaCl. Five different gas compositions were used:

1. 100 % methane
2. 99 % methane + 1 % ethane
3. 98 % methane + 2 % ethane
4. 95 % methane + 5 % ethane
5. 90 % methane + 10 % ethane

The depth of the BSR was determined from the seismic data, whereby two-way traveltimes were converted to depth using velocity models proposed by Westbrook et al. (2008), Hustoft et al (2009) and Petersen et al. (2010). The error on the depth estimate of the BSR is related to the error of the velocity analysis and is in the range of up to ± 2,5 m. The two-way traveltime to the seafloor was converted to depth using a velocity of 1730 m/s. Subsequently, observed BSR depth and predicted BGHSZ were evaluated with respect to gas composition and geothermal gradients. At present, there is no ground-truth data available from the study area, leading to great uncertainties when it comes to gas composition. Also, the geothermal gradient contains an uncertainty and can vary quite significantly over short distances as figure 4-7 indicates. Table 3 provides an overview of the locations chosen for the modeling, their geothermal gradients and BSR depths.

Location	Lower continental slope	MTF	Vestnesa Ridge crest in distance from pockmarks	Vestnesa Ridge crest at pockmark
Geothermal gradient [°C/km]	85	118	105	140
Water depth [m]	1080	2200	1245	1360
BSR depth [mbsf]	202	189	182	155

Table 3: Information about the locations chosen for the modeling.
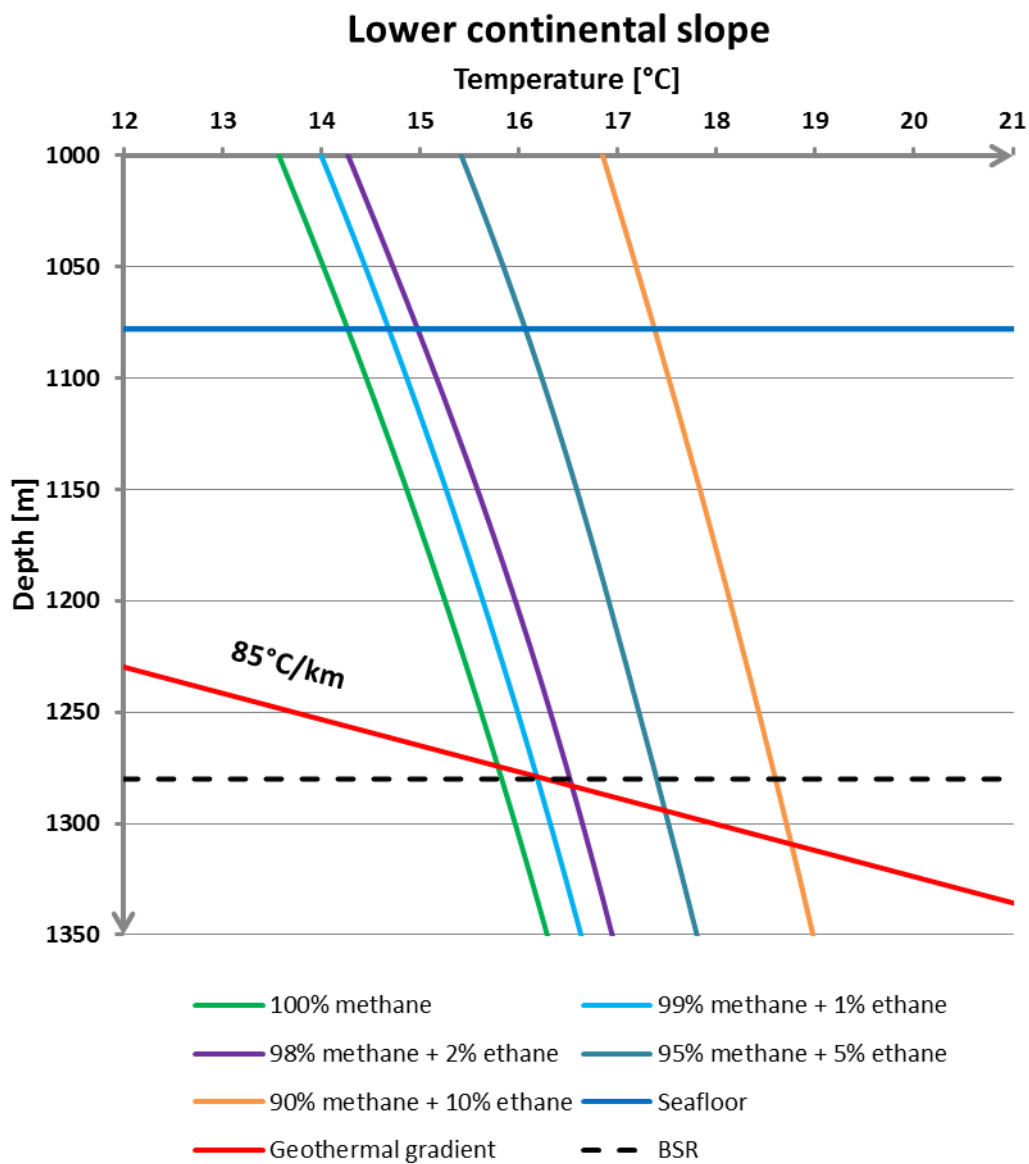
Figure 5-3: GHSZ modeling from the lower continental slope.

At the lower continental slope, the BSR was observed at 202 m bsf in water depth of 1080 m (figure 4-21). The geothermal gradient of 85 °C/km was derived from a heat flow station nearby and fits with a gas composition of 99 % methane + 1 % ethane (figure 5-3). This gas composition is reasonable assuming that methane is the dominant gas in the region (Vanneste et al., 2005[a]) and might stem from biogenic degradation of organic matter. The chosen location, at the eastern part of the lower continental slope (figure 4-21 and 5-1), show less fluid flow structures than the western part of the slope. An increase in the geothermal gradient is expected in western direction due to the closer distance to the MTF and the Knipovich Ridge and possibly due to warm uprising fluids along faults and chimneys/pipes. This is confirmed by the heat flow stations showing gradients up to 117 °C/km on this part of the slope. The second closest heat flow station and the corresponding geothermal gradient of 107 °C/km would give unlikely high fractions of higher order hydrocarbons at the observed BSR depth. Thus, it is believed that seismic observations are in good agreement with the modeling. It further indicates that the free-gas/gas-hydrate system on the continental slope is largely in a steady state, which is in agreement with results from numerical modeling of hydrate formation and gas depletion at the BSR interface (Haacke et al., 2008).

Molloy Transform Fault
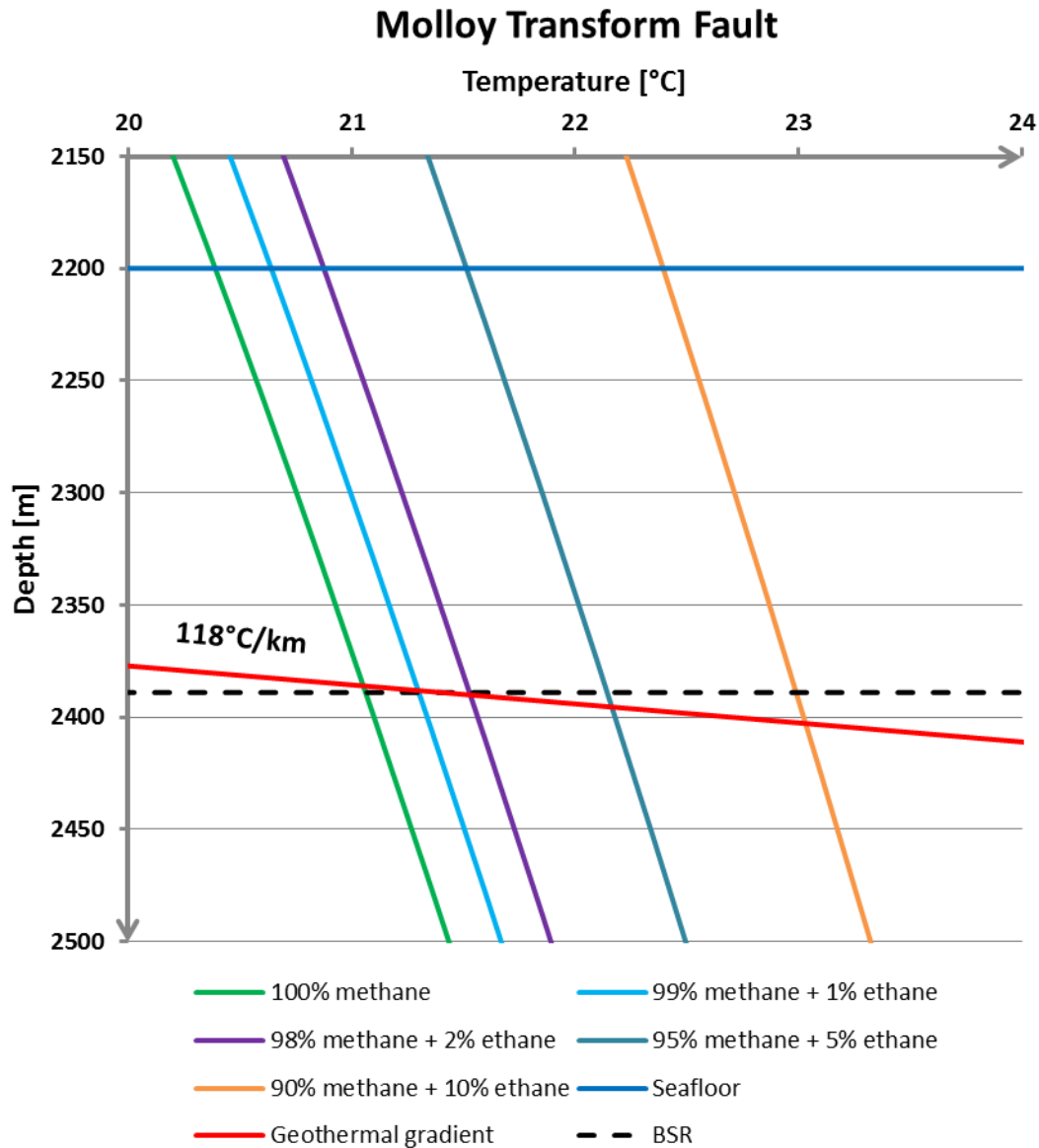
Figure 5-4: GHSZ modeling from the Molloy Transform fault.

The MTF is situated at ~2200 m, over 1000 m deeper than the lower continental slope. The observed BSR depth of 189 m is, however, shallower than at the slope (figure 4-19). This suggests that the area is strongly affected by the increased heat flow induced by the proximity of the mid-ocean ridge system. A geothermal gradient of 118 °C/km from a nearby heat flow station can predict the observed BSR depth using a gas composition that lies between 99 % methane + 1 % ethane and 98 % methane + 2 % ethane (figure 5-4). This is a relatively good agreement with the assumed gas composition at the lower continental slope, suggesting mainly biogenic origin of the gas. The sedimentary cover so close to the MTF is only a few hundred meters. However, a shallow maturation window due to the underlying hot oceanic crust and a therefore accelerated rate of biogenic and possibly thermogenic gas production might produce a substantial amount of gas to form gas hydrates and the ensuing BSR. Also at this location, seismic observations are in relatively good

agreement with predictions, although one might presume that the close distance to the MTF might cause a significant disturbance to the gas hydrate system.
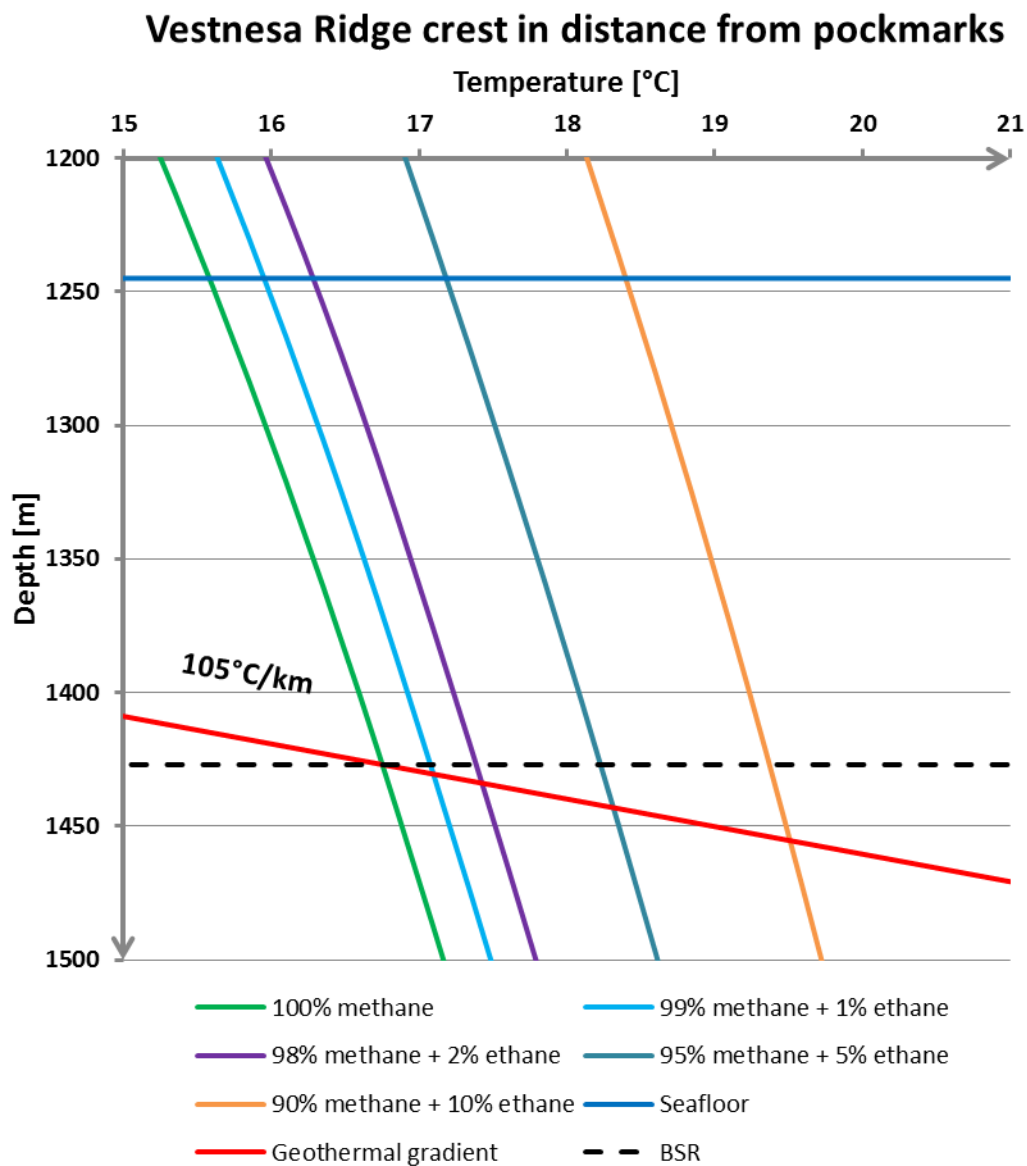
Figure 5-5: GHSZ modeling from the Vestnesa Ridge crest away from pockmark location.

Vestnesa Ridge crest at pockmark
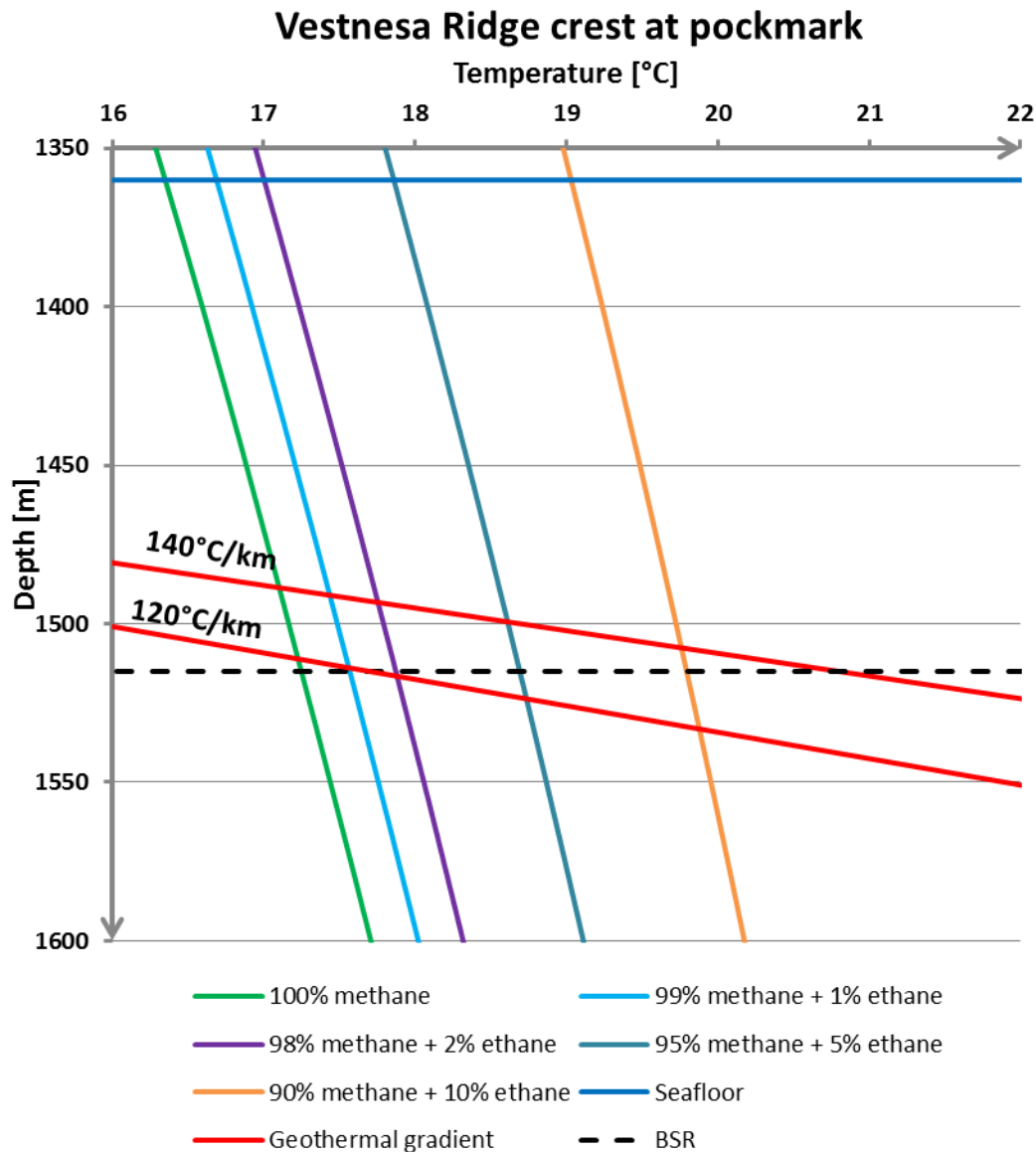
Figure 5-6: GHSZ modeling at pockmark location.

The modeling of the GHSZ on the Vestnesa Ridge was performed at two locations: away from pockmark and fluid flow structures and at a pockmark location (figure 5-1, 5-5 and 5-6). The BSR was observed at depth of 182 and 155 mbsf, respectively. This is consistent with the time-thickness map (figure 4-7) that revealed BSR shoaling at pockmark locations. The irregularity of the observed BSR depth suggests that increased heat flow in vicinity of fluid flow structures is responsible for the shoaling of the BSR. Variations in heat flow leads to variations in the geothermal gradient. As the Vestnesa Ridge crest show numerous fluid flow structures it is also expected that the geothermal gradient varies significantly over relatively short distances as observed from heat flow stations (figure 5-2).

At a distance of 1500 m from pockmarks and fluid flow structures, the BSR was observed at 182 mbsf. With a geothermal gradient of 105 °C/km, the BSR depth can be predicted using a gas composition of 95 % methane + 5 % ethane (figure 5-5). At a pockmark location the BSR was observed at 155 mbsf. A geothermal gradient of 140 °C/km derived from a heat flow station would assume a gas composition with larger fractions of higher order hydrocarbons to match the observed BSR depth.

 Both locations at the crest show anomalous gas compositions compared to the other two locations, in that a larger fraction of higher order hydrocarbons are indicated to be present. In particular the pockmark location indicates a surprisingly larger fraction of higher order hydrocarbons. Even within the uncertainties of the BSR depth estimate, the fraction of higher order hydrocarbons would be high resembling that of deep-rooted fossil source if the geothermal gradient is correct. Correspondingly, a lowering of the geothermal gradient to 120 °C/km must be obtained to achieve similar gas compositions as observed at the lower continental slope and the MTF.

It is likely that the distribution of gas hydrates on the Vestnesa Ridge is more influenced by the thermal regime than the continental slope concerning the local shoaling of the BSR in vicinity of fluid flow structures (figure 4-7) and the indication of the presence of higher order hydrocarbons (figure 5-5 and 5-6). Thermal alteration of organic matter occurs relatively deep in the sediments, generating methane and higher order hydrocarbons by catagenesis, preferably within a temperature range of 50-200°C. Because thermogenic gas generation generally occurs at temperatures much deeper than found within the GHSZ, concentration of thermogenic gases within the GHSZ indicates the existence of hydrocarbon migration pathways (Schulz and Zabel, 2006). At the pockmark location, the temperature would reach ~140 °C at 1 km sediment depth, and in distance from pockmark the temperature would reach ~210 °C at 2 km sediment depth, assuming the geothermal gradients derived from heat flow stations. High geothermal gradients would cause the optimal temperature window for thermogenic gas production to exist at a shallower depth. Due to the temperatures, being well within the thermogenic gas generation window, the vicinity of fluid flow structures observed to be rooted well beneath the BGHSZ (figure 4-12 and 4-13), and the sediment thickness of the ridge ranging from 1-5 km, it is likely that a mixture of thermogenic and biogenic gas sources are incorporated in the fluid flow system at the Vestnesa Ridge. The fact that fluid flow structures are far more abundant at the Vestnesa Ridge crest suggest that this area is more active and dynamic than elsewhere in the study area, and hence, also less in a steady state compared to the continental slope and MTF areas. Fluid expulsion at the crest has been attributed to the topography of the ridge, causing fluids to accumulate beneath the crest. It is, however, also likely

that the localization of the ridge on relatively young, hot crust has an impact on the gas hydrate distribution on the Vestnesa Ridge.

As previously mentioned, there is at present no ground-truth data from the Vestnesa Ridge area in terms of gas analysis. The closest ground-truthing is from ODP Leg 151 (sites 908, 909 and 912) (figure 2-1). Here, high methane concentrations were recorded as well as minor, but significant, amounts of ethane and propane (Stein et al., 1995). The modeling cannot be accepted as an exact determination of gas composition as uncertainties are connected to all the parameters involved. The origin of the gases and the gas compositions suggested here might therefore be slightly unreliable. However, the modeling does suggest a clear trend that points to an increase of larger fractions of higher order hydrocarbons at the Vestnesa Ridge crest.

6. Conclusion

2D and 3D seismic data allowed the mapping of a BSR on the western Svalbard margin including the Vestnesa Ridge. The identification of a BSR provides indirect evidence for the occurrence of gas hydrates in the area. The BSR is seismically characterized as a very variable reflection depending on the geological setting it occurs in. The BSR is cross-cutting the sedimentary strata, mimicking the seafloor over short distances and can be identified as a proper, phase-reversed reflection in its own right whereas in other areas it shows as the envelope of the upward termination of enhanced reflections. Enhanced reflection amplitudes beneath the BSR indicate the presence of significant amounts of free gas. Other evidence for the presence of gas hydrates in sediments offshore western Svalbard stems from the observation of amplitude blanking and instantaneous frequency analysis showing a clear change in frequency content across the BSR interface.

A BSR indicating the base of the gas hydrate stability zone was observed 180-260 ms (TWT) bsf on the seismic data used in this thesis. The BSR stretches out over an area of approximately 2700 km^2, including the entire Vestnesa Ridge, the Molloy Transform and the lower continental slope. The BSR is shoaling from the continental slope towards the mid-ocean ridge systems suggesting a strong temperature-controlled subsurface depth as the underlying young oceanic crust cools off eastward.

The BSR on the lower continental slope is bounded in eastward direction by the upper continental slope consisting of GDF deposits which are assumed to inhibit the formation of gas hydrates and the presence of BSRs on seismic data.

In the deep waters the gas hydrate occurrence is bound by the MTF to the west and south-west, and by the Knipovich Ridge to the south.

The flanks of the Vestnesa Ridge are believed to strongly inhibit vertical fluid flow due to the sealing properties of the hydrates that are believed to exist here. Due to these sealing properties, fluids are forced to migrate laterally towards the ridge crest.

Fluid-flow features like chimneys, pipes or pockmarks are confined to the crest of the Vestnesa Ridge, and together with the lack of fluid-flow features on the flanks of the ridge, it suggests a strong topographically controlled migration of fluids.

In vicinity of fluid-flow features, the BSR is either absent, significantly disturbed or present at a shallower depth. Fluid-flow features are often connected to faults that are rooted well below the BGHSZ indicating a supply of hydrocarbon gas from deep-seated sediments.

The high heat flow together with the tectonic activity of this region, a thick sedimentary cover, a shallow maturation window and an accelerated rate of biogenic and thermogenic gas production might cause substantial disturbance to the free-gas system leading to high variability in gas supply, gas migration and gas hydrate build-up.

Modeling of gas hydrate stability indicates that the free-gas/gas hydrate system on the lower continental slope and at the MTF is largely in a steady state, suggesting mainly biogenic origin of the gas. Compared to these areas, the free-gas/gas hydrate system at the Vestnesa Ridge crest is in a less steady state, suggesting a more active and dynamic system in vicinity of fluid flow structures. A mixture of biogenic and thermogenic gas sources are thought to be incorporated in the fluid-flow system of the Vestnesa Ridge.

7. References

Aagaard, K., Foldvik, A., and Hillman, S., 1987, The west-Spitsbergen Current – Deposition and water mass transformation: Journal of Geophysical Research, v. 92, p. 3778-3784.

Andreassen, K., Hogstad, K., and Berteussen, K.A., 1990, Gas hydrates in the southern Barents Sea, indicated by a shallow seismic anomaly: First Break, v. 8, p. 235-245.

Andreassen, K., Hart, P.E., and MacKay, M., 1997, Amplitude versus offset modeling of the bottom   simulating reflection associated with submarine gas hydrates: Marin Geology, v. 137, p. 25-40.

Archer, D., Buffett, B., and Brovkin, V., 2009, Ocean methane hydrates as a slow tipping point in the global carbon cycle: Proceedings of the National Academy of Sciences of the United States of America, v. 106, p. 20596-20601.

Ashi, J., and Taira, A., 1993, Thermal structure of the Nankai accretionary prism as inferred from the distribution of gas hydrate BSRs, Geological Society of America, Special Paper, v. 273, p. 137-149.

Badley, M.E., 1985, Practical seismic interpretation: International Human Resources Development Corporation, Boston, 265 p.

Badr, O., Probert, S.D., and O'Callaghan, P.W., 1991, Origins of atmospheric methane: Applied Energy, v. 40, p. 189-231.

Beauchamp, B., 2004, Natural gas hydrates: myths facts and issues: Comptes Rendus Geoscience, v. 336, p. 751-765.

Berndt., C., Bünz, S., Clayton, T., Mienert, J., and Saunders, M., 2004, Seismic character of bottom simulating reflectors: examples from the mid-Norwegian margin: Marine and Petroleum Geology, v. 21, p. 723-733.

Birkenmajer, K., 1975, Caledonides of Svalbard and plate tectonics: Geological Society of Denmark Bulletin, v. 24, p. 1-19.

Birkenmajer, K., 1981, The geology of Svalbard, the western part of the Barents Sea, and the continental margin of Scandinavia, in: Nairn, S.E.M., Churkin, M-Jr., and Stehli, F.G., eds., The Arctic Ocean, The Ocean Basins and Margins, Part 5, Plenum, New York, p. 265-329

Boetius, A., Ravenschlag, K., Schubert, C.J., Rickert, D., Widdel, F., Gieseke, A., Amann, R., Jørgensen, B.B., Witte, U., and Pfannkuche, O,. 2000, A marine microbial consortium apparently mediating anaerobic oxidation of methane: Nature, v. 407, p. 623-626.

Boswell, R., 2007, Resource potential of methane hydrate coming into focus: Journal of Petroleum Science and Engineering, v. 56, p. 9-13.

Boswell, R., 2009, Is gas hydrate energy within reach?: Science, v. 325, p. 957-958.

Bouriak, S., Vanneste, M., and Saoutkine, A., 2000, Inferred gas hydrates and clay diapirs near the Storegga Slide on the southern edge of the Vøring Plateau, offshore Norway: Marine Geology, v. 163, p. 125-148.

Brauti, K., 2005, Gasshydrater og temperaturutvikling fra den vestlige Svalbardmarginen og den midt-norske marginen, Masteroppgave i Geologi ved Universitetet i Tromsø, 146 p.

Breivik, A.J., Verhof, J., and Faleide, J.I., 1999, Effects of thermal contrasts on gravity modeling at passive margins: results from the western Barents Sea: Journal of Geophysical Research, v. 104, p. 15293-15311.

Brown, A.R., 1999, Interpretation of three-dimensional seismic data: American Association of Petroleum Geologists Memoir, v. 42, 512 p.

Buffet, B.A., and Zatsepina, O.Y., 2000, Formation of gas hydrate from dissolved gas in natural porous media: Marine Geology, v. 164, p. 69-77.

Bünz, S., Mienert, J., and Berndt, C., 2003, Geological controls on the Storegga gas-hydrate system of the mid-Norwegian continental margin: Earth and Planetary Science Letters, v. 209, p. 291-307.

Bünz, S., and Mienert, J., 2004, Acoustic imaging of gas hydrate and free gas at the Storegga Slide: Journal of Geophysical Research, v. 109, 15 p.

Bünz, S., Petersen, J., Hustoft, S., and Mienert, J., 2008, Environmentally – sensitive gas hydrates on the W-Svalbard margin at the gateway to the Arctic ocean: Proceedings of the 6th International Conference on Gas Hydrates, Vancouver, British Colombia, Canada, July 6-10, 6 p.

Bünz, S., and Mienert, J., 2009, Gas hydrate occurrence at the northernmost segment of the Mid-Atlantic Ridge, AGU Fall meeting, San Fransisco, California.

Butt, F.A., Elverhøi, A., Solheim, A., and Forsberg, C.F., 2000, Deciphering Late Cenozoic developement of the western Svalbard Margin from ODP Site 986 results: Marine Geology, v. 169, p. 373-390.

Chand, S., and Minshull, T.A., 2003, Seismic constraints on the effects of gas hydrate on sediment physical properties and fluid flow: a review: Geofluids, v. 3, p. 275-289.

Chand, S., Mienert, J., Andreassen, K., Knies, J., Plassen, L., and Fotland, B., 2008, Gas hydrate stability zone modeling in areas of salt tectonics and pockmarks of the Barents Sea suggests an active hydrocarbon venting system: Marine and Petroleum Geology, v. 25, p. 625-636.

Claypool, G., and Kaplan, I., 1974, The origin and distribution of methane in marine sediments in: Kaplan, I., ed., Natural Gases in Marine Sediments, Plenum, New York, p. 99-139.

Collett, T.S., and Dallimore, S.R., 2002, Detailed analysis of gas hydrate induced drilling and production hazards: Proceedings of the 4th International Conference on Gas Hydrates, Yokohama, Japan, April 19-23, p. 47-52.

Collett, T.S., 2002, Energy resource potential of natural gas hydrates: American Association of Petroleum Geologists Bulletin, v. 86, p. 1971-1992.

Crane, K., Eldholm, O., Myhre, A.M., and Sundvor, E., 1982, Thermal implications for the evolution of the Spitsbergen transform fault: Tectonophysics, v. 89, p. 1-32.

Crane, K., Sundvor, E., Foucher, J.-P., Hobart, M., Myhre, A.M., and LeDouaran, S., 1988, Thermal evolution of the western Svalbard Margin: Marine Geophysical Researces, v. 9, p. 165-194.

Crane, K., Sundvor, E., Buck, R., and Martinez, F., 1991, Rifting in the northern Norwegian-Greenland Sea: Thermal tests of asymmetric spreading: Journal of Geophysical Research, v. 96, p. 14529-14550.

Crane, K., Doss, H., Vogt, P., Sundvor, E., Cherkashov, G., Poroshina, I., and Joseph, D., 2001, The role of the Spitsbergen shear zone in determining morphology, segmentation and evolution of the Knipovich Ridge: Marine Geophysical Researches, v. 22, p. 153-205.

Dillon, W.P., and Max, M.D., 2000, Oceanic gas hydrates, in: Max, M., ed., Natural Gas Hydrate in Oceanic and Polar Environments: Kluwer Academic Publishers, Dordrecht, The Netherlands, p. 61-76.

Ecker, C., Dvorkin, J., and Nur, A., 2000, Estimating the amount of gas hydrate and free gas from marine seismic data: Geophysics, v. 65, p. 565-573.

Eiken, O., and Hinz, K., 1993, Contourites in the Fram Strait: Sedimentary Geology, v. 82, p. 15-32.

Faleide, J.I., Solheim, A., Fiedler, B.O., Hjelstuen, B.O., Andersen, E.S., and Vanneste, K., 1996, Late Cenozoic evolution of the western Barents Sea-Svalbard continental margin: Global and Planetary Evolution, v. 12, p. 53-74.

Feseker, T., Foucher, J.-P., and Harmegnies, F., 2008, Fluid flow or mud eruptions? Sediment temperature distributions on Håkon Mosby mud volcano, SW Barents Sea slope: Marine Geology, v. 247, p. 194-207.

Floodgate, G.D., and Judd, A.G., 1992, The origins of shallow gas: Continental Shelf Research, v. 12, p. 1145-1156.

Folger, P., 2010, Gas hydrates: resource and hazard: Congressional Research Service, The Library of Congress, May 25, 2010, Washinton DC, 9 p.

Ginsburg, G.D., Guseynov, R.A., Dadashev, A.A., Ivanova, G.A., Kazantsev, S.A., Soloviev, V.A., Telepnev, E.V., Askeri-Nasirov, R.Y., Yesikov, A.D., Maltseva, V.I., Mashirov, Y.G., and Shabayeva, I.Y., 1992, Gas hydrates of the southern Caspian: International Geology Review, v. 34, p. 765-782.

Ginsburg, G.D., and Soloviev, V.A., 1997, Methane migration within the submarine gas hydrate stability zone under deep water conditions: Marine Geology, v. 137, p. 49-57.

Grevemeyer, I., and Villinger, H., 2001, Gas hydrate stability and the assessment of heat flow through continental margins: Geophysical Journal International, v. 145, p. 647-660.

Grozic, J.L.H., 2009, Interplay between gas hydrates and submarine slope failure: Advances in Natural and Technological Hazards Research, v. 28, p. 11-30.

Guerin, G., and Goldberg, D., 2002, Sonic waveform attenuation in gas hydrate-bearing sediments from the Mallik 2L-38 research well, Mackenzie Delta, Canada: Journal of Geophysical Research, v. 107, 11 p.

Haacke, R.R., Westbrook, G.K., and Hyndman, R.D., 2007, Gas hydrate, fluid flow and free gas: Formation of the bottom-simulating reflector: Earth and Planetary Science Letters, v. 261, p. 407-420.

Haacke, R.R., Westbrook, G.K., and Riley, M.S., 2008, Controls on the formation and stability of gas hydrate-related bottom-simulating reflectors (BSRs): A case study from the west Svalbard continental slope: Journal of Geophysical Research, v. 113, 17 p.

Hamilton, E.L., 1980, Geoacoustic modeling of the sea floor: Journal of the Acoustical Society of America, v. 68, p. 1313-1340.

Hebbeln, D., Henrich, R., and Baumann, K-H., 1998, Paleoceanography of the last interglacial/glacial cycle in the Polar North Atlantic: Quaternary Science Reviews, v. 17, p. 125-153.

Hein, J.R and Scholl, D.W., 1978, Diagenesis of late Cenozoic diatomaceous deposits and formation of the bottom simulating reflector in the southern Bering Sea: Sedimentology, v. 25, p. 2021-2024.

Hansen, B., and Østerhus, S., 2000, North Atlantic – Nordic Seas exchanges: Progress in Oceanography, v. 45, p. 109-208.

Holbrook, S.W., Hoskins, H., Wood, W.T., Stephen, R.A., and Lizzaralde, D., 1996, Methane hydrate and free gas on the Blake Ridge from vertical seismic profiling: Science, v. 273, p. 1840-1843.

Holbrook, S.W., 2001, Seismic studies of the Blake Ridge: implications for hydrate distribution, methane expulsion and free gas studies, in: Paull, C.K., Dillon, W.P., eds., Natural Gas Hydrates: Occurrence, Distribution and Detection, Geophysical Monographs, American Geophysical Union, v. 124, p. 235-256.

Holbrook, S.W., Gorman, A.R., Hornbach, M., Hackwith, K.L., Nealon, J., Lizarralde., and Pecher, I.A., 2002, Seismic detection of marine methane hydrate: The Leading Edge, v. 21, p. 686-689.

Hornbach, M.J., Holbrook, W.S., Gorman, R., Hackwith, K.L., Lizarralde, D., and Pecher, I., 2003, Direct seismic detection of methane hydrate on the Blake Ridge: Geophysics, v. 68, p. 92-100.

Hovland, M., and Judd, A.G., 1988, Seabed pockmarks and seepages, impact on geology, biology and the marine environment: Graham & Trotman Ltd., 293 p.

Howe, J.A., Shimmield, T.M., and Harland, R., 2008, Late Quaternary contourites and glaciomarine sedimentation in the Fram Strait: Sedimentology, v. 55, p. 179-200.

Hustoft, S., 2005, Seismisk identifisering av fluidlekkasjer I gasshydratsettinger på den midt-norske og den vestlige Svalbard marginen, Masteroppgave i Geologi ved Universitetet i Tromsø, 140 p.

Hustoft, S., Mienert, J., Bünz, S., and Nouzé, H., 2007, High-resolution 3D-seismic data indicate focused fluid migration pathways above polygonal fault systems of the mid-Norwegian margin: Marine Geology, v. 245, p. 89-106.

Hustoft, S., Bünz, S., Mienert, J., and Chand, S., 2009, Gas hydrate reservoir and active methane-venting province in sediments on <20 Ma young oceanic crust in the Fram Strait, offshore NW-Svalbard: Earth an Planetary Science Letters, v. 284, p. 12-24.

Hyndman, R.D., and Davis, E.E., 1992, A mechanism for the formation of methane hydrate and seafloor bottom simulating reflectors by vertical fluid expulsion: Journal of Geophysical Research, v. 97, p. 7025-7041.

Hyndman, R.D., Spence, G.D., Chapman, R., Riedel, M., and Edwards, R.N., 2001, Geophysical studies of marine gas hydrate in northern Cascadia, in: Paull, C.K., Dillon, W.P., eds., Natural Gas Hydrates: Occurrence, Distribution and Detection, Geophysical Monographs. American Geophysical Union, v. 124, p. 273-296.

Jakobsson, M., Cherkis, N., Woodward, J., Coakley, B.J., and Macnab, R., 2000, A new grid of Arctic bathymetry: a significant resource for scientists and mapmakers: EOS Transactions, American Geophysical Union, v. 81, p. 89, 93, 96.

Judd, A.G., and Hovland, M., 2007, Seabed Fluid Flow – The impact on Geology, Biology and the Marine Environment: Cambridge University Press, Cambridge, 475 p.

Kennett, J.P,. Cannariato, K.G., Hendy, I.L., and Behl, R.J., 2003, Methane Hydrates in Quaternary Climate Change: The Clathrate Gun Hypothesis: American Geophysical Union, Washington, DC, U.S, 216 p.

Klerkx, J.M., De Batist, J., Poort, R., Hus, P., Van Rensbergen, O., and Granin, N.G., 2006, Tectonically controlled methane escape in Lake Baikal, Advances in the geological storage of carbon dioxide. NATO Science Series IV: Earth and Environmental Sciences, v. 65, p. 203-219.

Klitgaard Kristensen, D., Sejrup, H.P., and Haflidason, H., 2001, The last 18 kyr fluctuations in Norwegian Sea surface conditions and implications for the magnitude of climatic change; evidence from the North Sea: Paleoceanography, v. 16, p. 455-467.

Knies, J., Damm, E., Gutt, J., Mann, U., and Pinturie, L., 2004, Near surface hydrocarbon anomalies in shelf sediments off Spitsbergen: evidences for past seepages: Geochemistry Geophysics Geosystems, v. 5, 14 p.

Koh, C., 2002, Towards a fundamental understanding of natural gas hydrates: Chemical Society Reviews, v. 31, p. 157-167.

Koh, C., and Sloan, E.D., 2007, Natural gas hydrates: Recent advances and challenges in energy and environmental applications: AIChE Journal, v. 53, p. 1636-1643.

Krey, V., Canadell, J.G., Nakicenovic, N., Abe, Y., Andruleit, H., Archer, D., Grubler, A., Hamilton, N.T.M., Johnson, A., Kostov, V., Lamarque, JF., Langhorne, N., Nisbet, E.G., O'Neill, B., Riahi, K., Riedel, M., Wang, W., and Yakushev, V., 2009, Gas hydrates: entrance to a methane age or climate threat?: Environmental Research Letters, v. 4, 6 p.

Kvenvolden, K.A., and Barnard, L.A., 1983, Hydrates of natural gas in continental margins, in: Watkins, J.S., and Drake, C.L., eds., Studies in Continental Margin Geology, Bulletin of American Association of Petroleum Geologists, v. 34, p. 631-640.

Kvenvolden, K.A., and Lorenson, T., 2001, The global occurrence of natural gas hydrate, in: Paull, C., and Dillon, W., eds., Natural Gas Hydrates: occurrence, Distribution and Dynamics, AGU Monograph Series. American Geophysical Union, v. 124, p. 3-18.

Kvenvolden, K.A., 1988, Methane hydrate – A major reservoir of carbon in the shallow geosphere?: Chemical Geology, v. 71, p. 41-51.

Kvenvolden, K.A., 1993[a], Gas hydrates – Geological perspective and global change: Reviews of Geophysics, v. 31, p. 173-187.

Kvenvolden, K.A., 1993[b], Worldwide distribution of subaquatic gas hydrates: Geo-Marine Letters, v. 13, p. 32-40.

Kvenvolden, K.A., 1995, A review of methane in natural gas hydrate: Organic Geochemistry, v. 23, p. 997-1008.

Kvenvolden, K.A., 1998, A primer on the geological occurrence of gas hydrate, in J.-P. Henriet, and J. Mienert , eds., Gas Hydrates: Relevance to World Margin Stability and Climatic Changes, v. 137, Geological Society of London, Special Publication, p. 9-30.

Kvenvolden, K.A., 2000, Gas Hydrate and Humans: Annals of the New York Academy of Sciences, v. 912, p. 17-22.

Kvenvolden, K.A., 2006, Natural Gas Hydrate Occurrence and Issues: Annals of the New York Academy of Sciences, v. 715, p. 232-246.

Lerche, I., 2000, Estimates of worldwide gas hydrate resource: Energy Exploration and Exploitation, v. 18, p. 329-337.

Ligtenberg, J.H., 2005, Detection of fluid migration pathways in seismic data: implications for fault seal analysis: Basin Research, v. 17, p. 141-153.

Lovell, J.P.B., and Stow, D.A.V., 1981, Identification of ancient sandy contourites: Geology, v. 9, p. 347-349.

Lucazeau, F., Brigaud, F., and Bouroullec, J.L., 2004, High-resolution heat flow density in the lower Congo basin: Geochemistry, Geophysics, Geosystems (G^3), v. 5, p. 1-24.

Lundin, E., and Doré, A.G., 2002, Mid-Cenozoic post-breakup deformation in the 'passive' margins bordering the Norwegian-Greenland Sea: Marine and Petroleum Geology, v.19, p. 79-93.

Løseth, H., Wensaas, L., Arntsen, B., Hanken, N., Basire, C,. and Graue, K., 2011, 1000 m long gas blow-out pipes: Marine and Petroleum Geology, v. 28, p. 1047-1060.

MacDonald, G.J., 1990, Role of methane clathrates in past and future climates: Climatic Change, v. 16, p. 247-281.

MacKay, M.E., Jarrard, R.D., Westbrook, G.K., and Hyndman, R.D., 1994, Origin of bottom-simulating reflectors: geophysical evidence from the Cascadia accretionary prism: Geology, v. 22, p. 459-462.

Madrussani, G., Rossi, G., and Camerlenghi, A., 2010, Gas hydrates, free gas distribution and fault pattern on the west Svalbard continental margin: Geophysical Journal International, v. 180, p. 666-694.

Makogon, Y.F., Holditch, S.A., and Makogon, T.Y., 2007, Natural gas-hydrates: A potential energy source for the 21st century: Journal of Petroleum Science and Engineering, v. 56, p. 14-31.

Makogon, Y.F., 2010, Natural gas hydrates – A promising source of energy: Journal of Natural Gas Science and Engineering, v. 2, p. 49-59.

Maslin, M., Owen, M., Betts, R., Day, S., Jones, T.D., and Ridgwell, A., 2010, Gas hydrates: past and future geohazard?: Philosophical Transactions of the Royal Society, v. 368, p. 2369-2393.

Max, M.D., Johnson, A.H., and Dillon, W.P., 2006, Economic Geology of Gas Hydrates, Springer, Dordrecht, The Netherlands, 341p.

McIver, R.D., 1982, Role of naturally occurring gas hydrates in sediment transport: American Association of Petroleum Geologists Bulletin, v. 66, p. 789-792.

Mienert, J., Vanneste, M., Bünz, S., Andreassen, K., Haflidason, H., and Sejrup, H.P., 2005, Ocean warming and gas hydrate stability on the mid-Norwegian margin at the Storegga Slide: Marine and Petroleum Geology, v. 22, p. 233-244.

Miles, P.R., 1995, Potential distribution of methane hydrate beneath the European continental margins: Geophysical Research Letters, v. 22, p. 3179-3182.

Milkov, A.V., 2004, Global estimates of hydrate-bound gas in marine sediments: how much is really out there?: Earth-Science Reviews, v. 66, p. 183-197.

Minshull, T.A., and White, R., 1989, Sediment compaction and fluid migration in the Makran accretionary prism: Journal of Geophysical Research, v. 94, p. 7387-7402.

Minshull, T.A., Singh, S.C., and Westbrook, G.K., 1994, Seismic velocity structure at a gas hydrate reflector, offshore Western Columbia, from full waveform inversion: Journal of Geophysical Research, v. 99, p. 4715-4734.

Mitchum, J., Vail, P.R., and Sangree, J.B., 1977, Seismic stratigraphy and global changes of sea level, Part 6. Stratigraphic interpretation of seismic reflection patterns in depositional sequences. In: C.E. Payton., ed., Seismic Stratigraphy – Applications to Hydrocarbon Exploration, American Association of Petroleum Geology, v. 26., p. 117-133.

Mottl, M.J., and Wheat, C.G., 1994, Hydrothermal circulation through mid-ocean ridge flanks: Fluxes of heat and magnesium: Geochimica et Cosmochimica Acta, v. 58, p. 2225-2237.

Myhre, A.M., and Eldholm, O., 1988, The Western Svalbard margin (74° - 80°N): Marine and Petroleum Geology, v. 5, p. 134-156.

Myhre, A.M., Thiede, J., Firth, J.V., et al., 1995, Proceedings of the Ocean Drilling Program, Initial Reports, 151, Ocean Drilling Program, College Station, TX.

Nimblett, J., and Ruppel, C., 2003, Permeability evolution during the formation of gas hydrates in marine sediments: Journal of Geophysical Research, v. 108, p. 2420.

Nisbet, E., 1990, Did The end of the ice age: Canadian Journal of Earth Science, v. 27, p. 148-157.

Norville, G.A., and Dawe, R.A., 2007, [13]Carbon and hydrogen isotopic variations of natural gases in the southeast Columbus Basin offshore southeastern Trinidad, West Indies – clues to origin and maturity: Applied Geochemistry, v. 22, p. 2086-2094.

Nixon, M.F., and Grozic, J.L.H., 2006, A simple model for submarine slope stability analysis with gas hydrates: Norwegian Journal of Geology, v. 86, p. 309-316.

OECD, 2011, Organisation for Economic Co-operation and Development, glossary of statistical terms, http://stats.oecd.org/glossary.

Okino, K., Curewitz, D., Asada, M., Tamaki, K., Vogt, P., and Crane, K., 2002, Prelininary analysis of the Knipovich Ridge segmentation: influence of focused magmatism and ridge obliquity on an ultraslow spreading system: Earth and Planetary Science Letters, v. 202, p. 275-288.

Overpeck, J., Hughen, K., Hardy, D., Bradley, R., Case, R., Douglas, M., Finney, B., Gajewski, K., Jacoby, G., Jennings, A., Lamoureux, S., Lasca, A., MacDonald, G., Moore, J., Retelle, M., Smith, S., Wolf, A., and Zielinski, G., 1997, Arctic environmental changes of the last four centuries: Science, v. 278, p. 1251-1256.

Pecher, I.A., Kukowski, N., Ranero, C.R., and VonHuene, R., 2001, Gas hydrates along the Peru and middle America trench systems, in: Paull, C., Dillon, W.P., eds., Natural Gas Hydrates: Occurrence, Distribution and Detection, Geophysical Monographs, American Geophysical Union, v. 124, p. 257-271.

Petersen, C.J., Bünz, S., Hustoft, S., and Mienert, J., 2008, 3D seismic imaging of marine gas hydrates in arctic sediments of the Vestnesa Ridge off the W-Svalbard margin: Proceedings of the 6th International Conference on Gas Hydrates, Vancouver, British Colombia, Canada, July 6-10, 8 p.

Pierce, B.S., and Collett, T.S., 2004, Energy Resource Potential of Natural Gas Hydrates: 5th Conference & Exposition on Petroleum Geophysics, Hyderabad 2004, India, p. 899-903.

Popescu, I., Lericolais, G., Panin, N., De Batist, M., and Gillet, H., 2007, Seismic expression of gas and gas hydrates across the western Black Sea: Geo-Marine Letters, v. 27, p. 173-183.

Posewang, J., and Mienert, J., 1999, High-resolution seismic studies of gas hydrates west of Svalbard: Geo-Marine Letters, v. 19, p. 150-156.

Premuzic, E.T., Benkovitz, C.M., Gaffney, J.S., and Walsh, J.J., 1982, The nature and distribution of organic matter in the surface sediments of world oceans and seas: Organic Geochemistry, v. 4, p. 63-77.

Rice, D.D., and Claypool, G.E., 1981, Generation, accumulation, and resource potential of biogenic gas: American Association of Petroleum Geologists Bulletin, v. 65, p. 5-25.

Riedel, M., Willoughby, E,C., and Chopra, S., eds., 2010, Geophysical Characterization of Gas Hydrate, Society of Exploration Geophysicists, Oklahoma, U.S, 392 p.

Ritzmann, O., Jokat, W., Czuba, W., Guterch, A., Mjelde, R., and Nishimura, Y., 2004, A deep seismic transect from Hovgård Ridge to northwestern Svalbard across the continental-ocean transition: A sheared margin study: Geophysical Journal International, v. 157, p. 683-702.

Ruppel, C., 1997, Anomalously cold temperatures observed at the base of the gas hydrate stability zone, U.S. Atlantic passive margin: Geology, v. 25, p. 699-702.

Ruppel, C., 2000, Thermal state of the gas hydrate reservoir, in: Max, M.D., ed., Natural Gas Hydrates in Oceanic and Permafrost Environments, Kluwer Academic Publishers, p. 29-42.

Sain, K., Minshull, T.A., Singh, S.C., and Hobbs, R.W., 2000, Evidence for a thick free gas layer beneath the bottom simulating reflector in the Makran accretionary prism: Marine Geology, v. 164, p. 3-12.

Sassen, R., Roberts, H.H., Carney, R., Milkov, A.V., DeFreitas, D.A., Lanoil, B., and Zhang, C., 2004, Free hydrocarbon gas, gas hydrate, and authigenic minerals in chemosynthetic communities of the northern Gulf of Mexico continental slope: relation to microbial processes: Chemical Geology, v. 205, p. 195-217.

Satyavani, N., Sain, K., Lall, M., and Kumar, B.J.P., 2008, Seismic attribute study for gas hydrates in the Andaman Offshore India: Marine Geophysical Researc, v. 29, p. 167-175.

Schlumberger, 2001, Schlumberger Oilfield Glossary, http://www.glossary.oilfield.slb.com.

Schlüter, H.H., and Hinz, K., 1978, The continental margin of West Spitsbergen: Polarforschung, v. 48, p. 151-169.

Shankar, U., Thakur, N.K., and Reddi, S.I., 2004, Estimation of geothermal gradients and heat flow from Bottom Simulating Reflector along the Kerala-Konkan basin of Western Continental Margin of India: Current Science, v. 87, p. 250-253.

Shipley, T.H., Houston, M.K., Buffler, R.T., Shaub, F.J., McMillan, K.J., Ladd, J.W., and Worzel, J.L., 1979, Seismic reflection evidence for the widespread occurrence of possible gas hydrate horizons on continental slopes and rises: American Association of Petroleum Geologists Bulletin, v. 63, p. 2201-2213.

Schulz, H.D., and Zabel, M., 2006. Marine Geochemistry, Berlin, Springer, 574 p.

Sloan, E.D., 1990, Natural gas hydrate phase equilibria and kinetics; understanding the state-of-the-art: Revue de l'Institut Francais du Petrole, v. 45, p. 245-266.

Sloan, E.D., 1998[a], Physical/chemical properties of gas hydrates and application to world margin stability and climatic change, in J.-P. Henriet, and J. Mienert, eds., Gas Hydrates: Relevance to World Margin Stability and Climatic Changes, v. 137, Geological Society of London, Special Publication, p. 31-50.

Sloan, E.D., 1998[b], Clathrate hydrates of natural gases: New York & Basel, Marcel Dekker Inc, 705 p.

Sloan, E.D., 2003, Fundamental principles and applications of natural gas hydrates: Nature, v. 426, p. 353-362.

Sloan, E.D., and Koh, C., 2008, Clathrate Hydrates of Natural Gases, Third Edition, No. 119 in Chemical Industries. CRC Press, Taylor & Francis group, 721 p.

Solheim, A., Faleide, J.I., Andersen, E.S., Elverhøi, A., Forsberg, C.F., Vanneste, K., Uenzelmann-Neben, G., and Channell, J.E.T., 1998, Late Cenozoic seismic stratigraphy and glacial geological developement of the East Greenland and Svalbard-Barents Sea continental margins: Quaternary Science Reviews, v. 17, p. 155-184.

Stein, R., Brass, G., Graham, D., Pimmel, A., and Shipboard Scientific Party., 1995, Hydrocarbon measurements at Arctic Gateways sites (ODP LEG 151), in: Myhre, A.M., Thiede, J., Firth, J.V., et al., eds., Proceedings of the Ocean Drilling Program, Initial Reports, v. 151, p. 385-395.

Stow, D.A.V., and Lovell, J.P.B., 1979, Contourites: Their recognition in modern and ancient sediments: Earth-Science Reviews, v. 14, p. 251-291.

Suess, E., Torres, M.E., Bohrmann, G., Collier, R.W., Greinert, J., Linke, P., Rehder, G., Trehu, A., Wallmann, K., Winckler, G., and Zuleger, E., 1999, Gas hydrate destabilization: enhanced dewatering, benthic material turnover and large methane plumes at the Cascadia convergent margin: Earth and Planetary Science Letters, v. 170, p. 1-15.

Sundvor, E., Eldholm, O., Gladczenko, T.P., and Planke, S., 2000, Norwegian-Greenland Sea thermal field, in A. Nøttvedt, ed., Dynamics of the Norwegian margin, v. 167, Geological Society Special Publication, v. 176, p. 397-410.

Talwani, M., and Eldholm, O., 1977, Evolution of the Norwegian-Greenland Sea: Geological Society of America Bulletin, v. 88, p. 969-999.

Taylor, M.H., Dillon, W.P., and Pecher, I.A., 2000, Trapping and migration of methane associated with the gas hydrate stability zone at the Blake Ridge diapir: new insights from seismic data: Marine Geology, v. 164, p. 79-89.

Thiede, J., Pfirman, S., Schenke, H-W., and Reil, W., 1990, Bathymetry of Molloy Deep: Fram Strait between Svalbard and Greenland: Marine Geophysical Researches, v. 12, p. 197-214.

Thiede, J., Winkler, A., Wolf-Welling, T., Eldholm, O., Myhre, A.M., Baumann, K-H., Henrich, R., and Stein, R., 1998, Late Cenozoic history of the Polar North Atlantic: results from ocean drilling: Quaternary Science Reviews, v. 17, p. 185-208.

Tilley, B., and Muehlenbachs, K., 2008, Biogenic gases in the western Canada sedimentary basin: AAPG Annual Convention, San Antonio, Texas, U.S, April 20-23, 28 p.

Townend, J., 1997, Estimates of conductive heat flow through bottom-simulating reflectors on the Hikurangi and southwest Fiordland continental margins, New Zealand: Marine Geology, v. 141, p. 209-220.

Tucholke, B.E., Bryan, G.M., and Ewing, J.I., 1977, Gas-hydrate horizons detected in seismic-profiler data from the western North Atlantic: American Association of Petroleum Geologists Bulletin, v. 61, p. 698-707.

U.S. Energy Information Administration, 2011, Glossary, http://www.eia.gov/tools/glossary/ .

Valentine, D.L., Balnton, D.C., Reeburgh, W.S., and Kastner, M., 2001, Water column methane oxidation adjacent to an area of active hydrate dissociation, Eel river basin: Geochimica et Cosmochimica Acta, v. 65, p. 2633-2640.

Vanneste, M., Guidard, S., and Mienert, J., 2005[a], Arctic Gas Hydrate Provinces along the Western Svalbard Continental Margin: Norwegian Petroleum Society Special Puplications, v. 12, p. 271-284.

Vanneste, M., Guidard, S., and Mienert, J., 2005[b], Bottom-simulating reflections and geothermal gradients across the Svalbard margin: Terra Nova, v. 17, p. 510-516.

Vogt, P.R., 1986, Geophysical and geochemical signatures and plate tectonics. In Hurdle, B.G., ed., The Nordic Seas: New York, Springer, p. 413-664.

Vogt, P.R., Crane, K., Sundvor, E., Max, M.D., and Pfirman, S.L., 1994, Methane-generated(?) pockmarks on young, thickly sedimented oceanic crust in the Arctic: Vestnesa Ridge, Fram Strait: Geology, v. 22, p. 255-258.

Vogt, P.R., Gardner, J., and Crane, K., 1999, The Norwegian-Barents-Svalbard (NBS) continental margin: Introducing a natural laboratory of mass wasting, hydrates, and ascent of sediment, pore water, and methane: Geo-Marine Letters, v. 19, p. 2-21.

Vorren, T.O., Lebesbye, E., Andreassen, K., and Larsen, K.-B, 1989, Glacigenic sediments on a passive continental margin as exemplified by the Barents Sea: Marine Geology, v. 85, p. 251-272.

Vorren, T.O., and Laberg, J.S., 1997. Trough Mouth Fans – paleoclimate and ice-sheet monitors: Quaternary Science Reviews, v. 16, p. 865-881.

Vorren, T.O., Laberg, J.S., Blaume, F., Dowdeswell, J.A., Kenyon, N.H., Mienert, J., Rumohr, J., and Werner, F., 1998, The Norwegian – Greenland Sea continental margins: morphology and Late Quaternary sedimentary processes and environment: Quaternary Science Reviews, v. 17, p. 273-302.

Westbrook, G.K., Chand, S., Rossi, G., Long, C., Bünz, S., Camerlenghi, A., Carcione, J.M., Dean, S., Foucher, J.-P., Flueh, E., Gei, D., Haacke, R.R., Madrussani, G., Mienert, J., Minshull, T.A., Nouzé, H., Peacock, S., Reston, T.J., Vanneste, M., and Zillmer, M., 2008, Estimation of gas hydrate concentration from multi-component seismic data at sites on the continental margins of NW Svalbard and the Storegga region of Norway: Marine and Petroleum Geology, v. 25, p. 744-758.

Winters, B., and Lorenson, T., 2002, Gas Hydrate Studied in the Northern Gulf of Mexico: Sound Waves Monthly Newsletter, United States Geological Survey, Washington DC, U.S, September, at http://soundwaves.usgs.gov/2002/09.

Woodside, J.M., Modin, D.I., and Ivanov, M.K., 2003, An enigmatic reflector on subbottom profiler record from the Black Sea – The top of the shallow gas hydrate deposits: Geo-Marine Letters, v. 23, p. 269-277.

Xu, W., and Ruppel, C., 1999, Predicting the occurrence, distribution and evolution of methane gas hydrates in porous marine sediments: Journal of Geophysical Research, v. 104, p. 5081-5096.

Yamano, M., Uyeda, S., Aoki, Y., and Shipley, T.H., 1982, Estimates of heat flow derived from gas hydrates: Geology, v. 10, p. 339-343.